PRINCIPLES, DESIGN, FABRICATION, AND CHARACTERIZATION OF SUBWAVELENGTH PERIODIC RESONANT METASURFACES

by

Hafez Hemmati

DISSERTATION

Submitted to the Graduate Faculty of
The University of Texas at Arlington
in Partial Fulfillment of the
Requirements for the Degree of
Doctor of Philosophy

Arlington, Texas

December 2020

Supervising Committee:

Prof. Robert Magnusson
Prof. Efstathios I. Meletis
Prof. Yaowu Hao
Prof. Michael Vasilyev
Prof. Kyungsuk Yum

Acknowledgements

First I would like to express my deepest appreciation and sincere gratitude to my advisor Professor Robert Magnusson who guided me to resonance not only with the scientific advances in the field, but also to resonance with the real life in a way to overcoming the obstacles and always staying motivated. His dedication to science and enthusiasm for his research is always a great inspiration to me, and I am sure to many others. I am highly indebted to his ideas, understanding, and support during times of my personal difficulties.

I would also like to thank Prof. Efstathios I. Meletis, Prof. Yaowu Hao, Prof. Michael Vasilyev, and Prof. Kyungsuk Yum for their kind consent to be in my dissertation committee and giving me valuable comments.

I am also very grateful to Prof. Nader Hozhabri for his support from the time I attended the UTA. In addition, I am very thankful to UTA NanoFab experts Mr. Huan (Mick) Nguyen, Mr. Richard K. Chambers, and Mr. Dennis Bueno whom trained and helped me on various tools in the cleanroom.

I am very thankful to Dr. Kyu Jin Lee for all his help, guidance, and co-work during my research.

I would like to thank all my previous and current colleagues at "Nanophotonics Device Group" Prof. Halldor Svavarsson, Dr. Yeong Hwan Ko, Dr. Manoj Niraula, Dr. Alex Fannin, Dr. Daniel Carney, Dr. Sun-Goo Lee, Dr.

Subrata Das, Dr. Pawarat (Fern) Bootpakdeetam, Nasrin Razmjooei, Joseph Buchanan-Vega, Fairooz Simlan, and Robert Wood.

I am also grateful to my friends at UTA, Dr. Shahab Ranjbar Bahadori, Dr. Maziar Mahdavi, Dr. Han Zhang, Dr. Amir Koolivand, Dr. Amirali Nojoomi, and Hossein Madanipour for supporting me through all the difficult times I have had during my Ph.D. work.

I also acknowledge my funding sources: The National Science Foundation (NSF) [Award No. ECCS-1606898, ECCS-1809143, and IIP-1826966], the UT System Texas Nanoelectronics Research Superiority Award funded by the State of Texas Emerging Technology Fund as well as by the Texas Instruments Distinguished University Chair in Nanoelectronics endowment.

October 20, 2020

Dedications

I dedicate this work

To my father Firouz and my mother Faridokht

for all the love and sacrifices you made for me

To my lovely sisters and nieces

for all your love and motivation

To my incredible wife Nazila

for all your love and constant support during hard times

To my lovely daughter Nora

for bringing joy and happiness to my life

To my friends all around the world

for your continues support

I feel very fortunate to have all of you in my life.

Hafez Hemmati

October 20, 2020

Abstract

PRINCIPLES, DESIGN, FABRICATION, AND CHARACTERIZATION OF SUBWAVELENGTH PERIODIC RESONANT METASURFACES

HAFEZ HEMMATI, Ph.D.

The University of Texas at Arlington, 2020

Supervising Professor: Robert Magnusson

Since the emergence of diffraction gratings containing periodic unit cells, innumerable advances in theoretical studies and practical applications have emerged. Recently, these classic structures have been categorized as subsets of "meta-surfaces" or "meta-materials" in which periodically aligned wavelength-scale features manipulate all key properties of the electromagnetic waves in a desired manner for a wide variety of applications. This includes manipulating of amplitude, phase, spectral distribution, polarization state, and local mode structure of light in the various available spectral expressions. Among the significant characteristic properties of metasurfaces is the coupling of incident light to laterally propagating leaky Bloch modes in the subwavelength regime when the periodicity of the unit cell is moderately smaller than the free-space wavelength. This property,

which manifests itself as a resonance at certain wavelengths, is called “guided mode resonance (GMR)” or “leaky mode resonance (LMR)”. These structures offer novel properties and functionalities in ultra-thin device dimensions which make them potential replacements for conventional and bulky optical devices. Extensive studies have been conducted to realize the periodic structures in different materials (metals, dielectric, and semiconductors or their hybrid compositions) employing various fabrication methods for different wavelength ranges in 1D or 2D configuration. Thus, on account of the wide variety of material compositions and lattice architectures, the design space is vast.

Various numerical techniques such as rigorous coupled-wave analysis (RCWA), finite element method (FEM), and finite-difference time-domain (FDTD) can be used to implement simulations and obtain the precise optical responses of the metasurfaces. In addition, inverse optimization methods, efficiently provide optimized physical parameters in order to obtain a particular desired spectral response. However, these computational methods which are based on solving heavy and complicated equations and do not always provide comprehensive insight into underlying physics of the numerically obtained optical spectra.

In this dissertation, we present a comprehensive physical description of resonant metasurfaces based on exact solutions of the Rytov formulation. We define a clear transition wavelength between the resonance subwavelength region and the deep-subwavelength region. This transition point, analytical in a special

case, is not available presently in the literature. In addition, we design, fabricate, and characterize various novel GMR-based optical devices such as metamaterial polarizers, nanoimprinted nanocomposite filters, multipart unit-cell metasurfaces, ultrahigh-Q resonant dual-grating metamembranes, and fiber-facet integrated optical filters and sensors.

Table of Contents

List of Illustrations

List of Abbreviations

AFM	Atomic Force Microscopy
ATR	Attenuated Total Reflectance
BIC	Bound States in the Continuum
BPM	Beam Propagation Method
DLS	Dynamic Light Scattering
EMT	Effective Medium Theory
ER	Extinction Ratio
FDTD	Finite Difference Time Domain
FTIR	Fourier Transform Infrared Spectroscopy
LIL	Laser Interference Lithography
MMF	Multi-Mode Fiber
NIL	Nanoimprint Lithography
OSA	Optical Spectrum Analyzer
PDMS	Polydimethylsiloxane
PM	Polarization Maintaining
PVP	Polyvinylpyrolidone
RCWA	Rigorous Coupled-Wave Analysis
RIE	Reactive Ion Etching
RIU	Refractive Index Unit

SEM	Scanning Electron Microscopy
SOQ	Silicon on Quartz
TE	Transverse Electric
TM	Transverse Magnetic
WGP	Wire Grid Polarizer
1D	One Dimensional
2D	Two Dimensional
3D	Three Dimensional

Chapter 1

Introduction and Background

Light, which is an electromagnetic wave, plays a significant role in recent technological advancements involved in our daily life such as cell phones, televisions, and wireless networking. Light waves can be used by astronomers to identify various objects in space, or it can be used by a chemist to determine the chemical composition of an unknown material.

From the early days, scientists have manipulated the wavefront shape and phase of electromagnetic waves. Conventional lenses mainly used in imaging converge or diverge a light beam based on refraction at the interface of two different materials. Conventional polarizers, which transmit the desired polarization of the light while blocking the unwanted polarization state based on natural crystals and multilayer thin films are commonplace. All of these optical components are bulky and expensive.

Therefore, light-matter interaction in compact format is very important for light-manipulation-based systems. In 1902, Wood reported abrupt changes in the intensity and black and bright bands of the spectra obtained from a metallic diffraction grating [1]. He also found out the occurrence of these singular anomalies is polarization dependent (i.e. the bands can be found only in P polarization of the incident light). These phenomena are known as Wood's anomaly, as they could not be explained by ordinary grating theory. In 1907, Rayleigh tried to explain these

anomalies. He explained the occurrence of the wavelength anomaly arising of the wavelength at which the higher order passing-off in a spectrum. Although his method could predict the wavelength and polarization dependent response, it failed to explain the abrupt intensity change observed in Wood's anomaly [2].

1.1 Diffraction grating

A schematic of a diffraction grating, with periodicity of Λ and refractive index modulation of n_H and n_L, under illumination of an obliquely incident electromagnetic plane wave is shown in **Figure 1-1**. In general, the periodic structure of the diffraction grating produces various diffraction orders propagating in the cover region with refractive index of n_C and substrate medium with index of n_S. The "grating equation" for the backward diffracted wave and the forward diffracted wave gives the relation between diffraction angle (θ_m) and the angle of incidence (θ_i) as [2]

$$n_C \sin\theta'_m = n_C \sin\theta_i + m\frac{\lambda}{\Lambda} \tag{1.1}$$

$$n_S \sin\theta''_m = n_C \sin\theta_i + m\frac{\lambda}{\Lambda} \tag{1.2}$$

where λ is the wavelength of incident light.

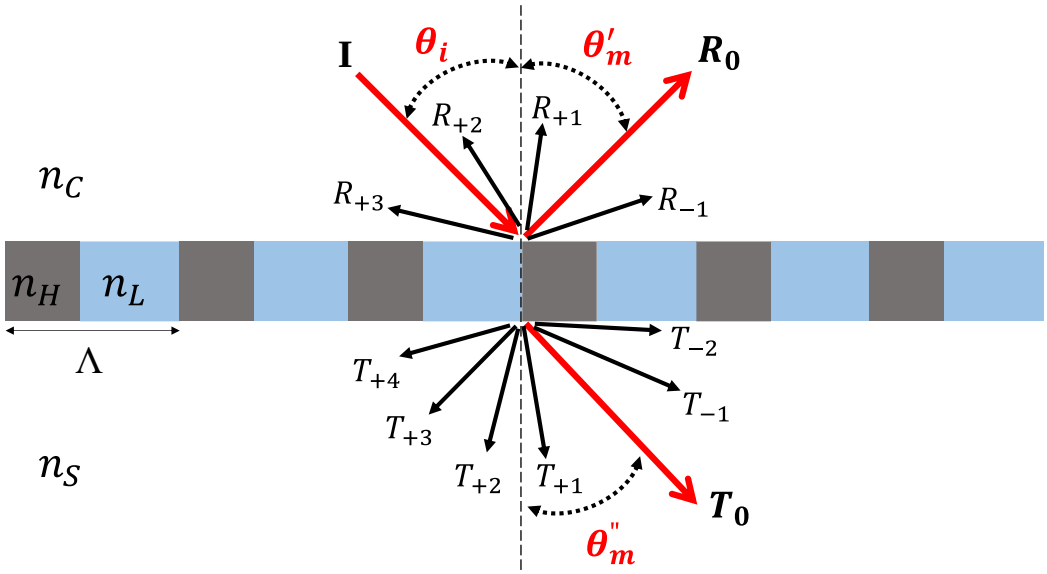

Figure 1-1 Schematic of diffraction orders due to periodic grating.

Choosing various wavelength to periodicity ratios, one can define two main diffraction regime for the grating: Non-subwavelength grating possessing more than one propagative diffracted orders and subwavelength grating which only zero-diffraction orders can be coupled to the cover or substrate while all the higher diffraction orders are evanescent. Transition from non-subwavelength to subwavelength regime, with periodicities smaller than wavelength, occurs at the Ryleigh wavelength (λ_R) [2]. These points are shown schematically in **Figure 1-2**.

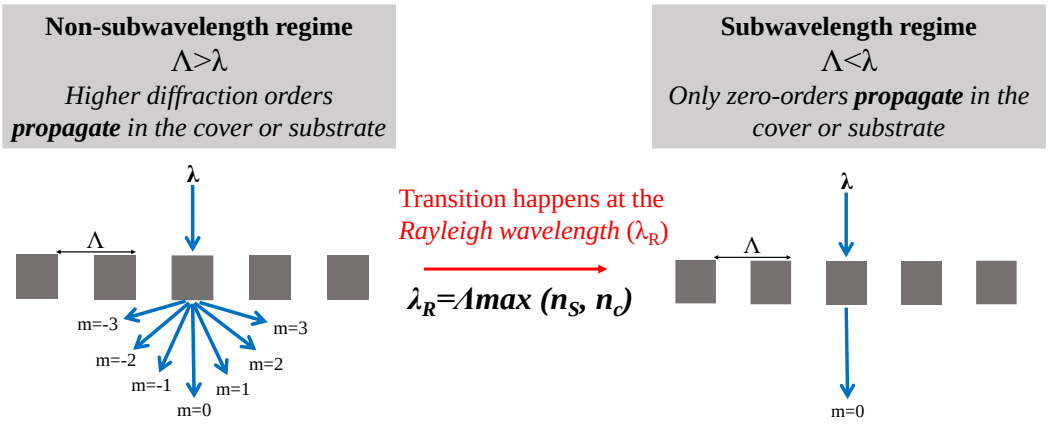

Figure 1-2 Two main diffraction regimes.

1.2 Guided-mode resonance mechanism

One interesting phenomenon which happens at subwavelength grating structure is guided-mode resonance [3-11]. The term "guided-mode resonance" was coined in 1990 by Wang et al. in an attempt to clearly communicate the fundamental physics governing these phenomena [11]. In earlier literature on the subject, authors often referred to these effects as being "anomalous," thereby implying that the phenomena were not well understood. **Figure 1-3** shows a representative guided mode resonance (GMR) or leaky-mode resonance (LMR) device consistsing of a subwavelength periodic grating and a waveguide layer over a substrate. Recently, periodic photonic lattices are often referred to as "metasurfaces" or "metamaterials" in which periodically aligned wavelength-scale features enable manipulation of an incoming electromagnetic waves in a desired manner. At resonance, the diffracted light by subwavelength grating, couples to a waveguide mode and propagates in the

lateral direction. While propagating, the mode leaks out due to the presence of the grating on the waveguide. The constructive (destructive) interference based on the phase difference between outgoing "leaky" wave and directly reflected wave from the grating surface forms a reflection (transmission) resonance in the optical spectrum of the device. Therefore, the guided mode resonance device can be seen as operating in light capture, storage, and release modes. The GMR terminology emphasizes the capture of photonic energy whereas LMR emphasizes its release.

By design, a plethora of differing spectral expressions is available with this device class thus providing a flexible applications platform. Wide parametric design spaces allow control of light amplitude, phase, polarization, near-field intensity, and light distribution on surfaces and within device volumes.

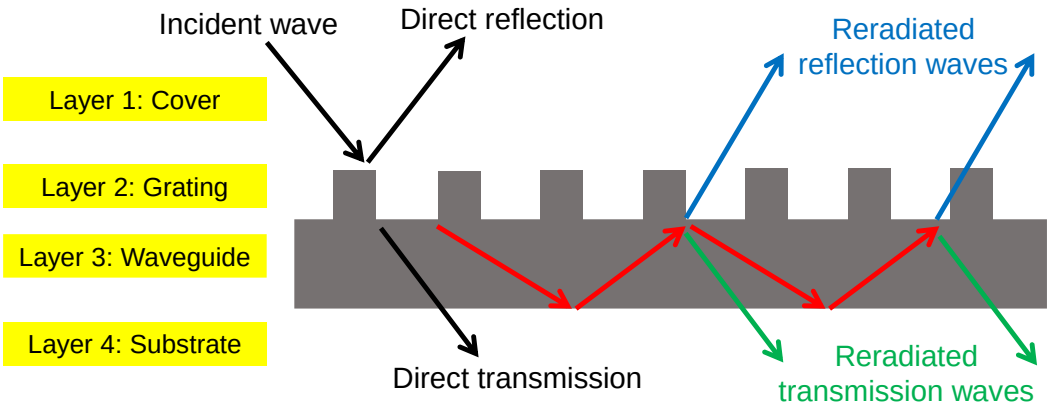

Figure 1-3 Schematic illustration of a GMR device.

1.3 Simulation tools

To obtain the exact optical response from GMR metasurfaces, such as reflection, transmission, diffraction, and internal field profile, two widely-used methods, rigorous coupled-wave analysis (RCWA) and finite-difference time domain (FDTD), are employed in our work. To simulate the optical response of our devices under plane wave incidence we use the RCWA method.

We use a home-written RCWA MATLAB code, developed in our lab at the University of Texas at Arlington, for design with 1D periodicity. However, for complicated structures and advanced simulation, we use commercially available RSoft DiffractMOD. For finite grating design and Gaussian input beams we use RSoft FullWAVE module for simulation.

To optimize the geometrical dimensions and device parameters, particle swarm optimization (PSO) technique is used. Our PSO code which contains the RCWA method is an iterative code to optimize design parameters in a way to obtain a desired output spectrum.

1.4 Device fabrication

1.4.1 Laser interference lithography (LIL)

There are many methods for fabricating GMR devices such as electron-beam (e-beam) lithography, mask-based photolithography, focused-ion beam (FIB) lithography, and laser interference lithography (LIL). Many fabricated devices have

been made with the e-beam lithography technique. This method of fabrication is time consuming, expensive, and impractical when applying patterning on large areas because of potential stitching issues and a restricted area of exposure. Among nanofabrication methods, LIL enables rapid realization of high- quality periodic structures on a large surface area. This method offers versatility for fabricating diffractive elements and metastructures because the periodicity and fill factor can be altered without the use of traditional masks. One advantage of LIL is that in comparison with electron-beam lithography, it does not require high vacuum chamber for patterning.

We employ a Lloyd's mirror interference lithography configuration which consists of a high-quality mirror mounted orthogonally to the sample holder stage. A schematic of this system is depicted in **Figure 1-4**. The attendant two-wave interference generates periodic fringes via constructive and destructive interference between the two parts of the collimated laser beam when they come together in phase onto the sample surface. A UV laser (TOPTICA Photonics Inc.) with 100 mW output power at 266 nm wavelength is used for patterning. Each exposure has a periodicity that is determined by $\Lambda=\lambda/2\sin\theta$ in which λ is our laser wavelength (266 nm) and θ is the bisector of the angle between the two interfering beams. This angle can be precisely controlled by rotating the stage. Therefore, changing θ allows one to change the periodicity of the grating. In LIL, typically, the exposure dose $E=It$ in mJ/cm^2 is controlled by exposure time t when I=constant.

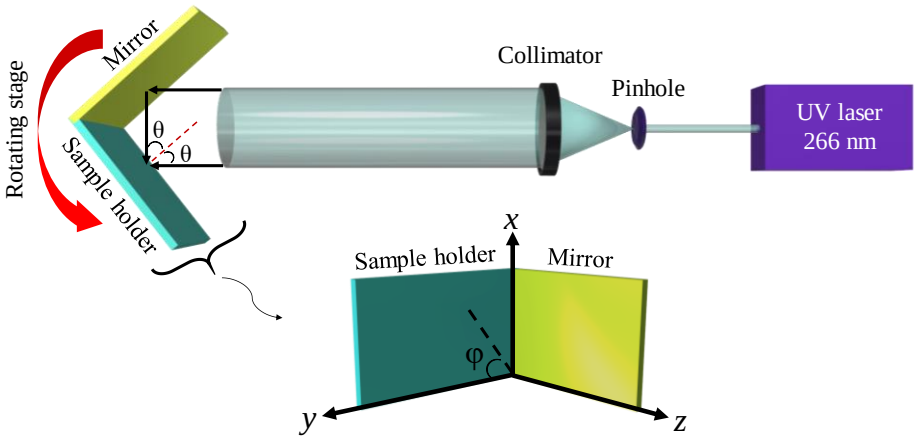

Figure 1-4 Schematic of an exemplary Lloyd's mirror laser interference lithography setup.

Employing two-beam interference lithography, 2D periodic structures can be realized by applying two sequential exposures and by rotating the substrate in its plane to $\varphi=90^{o}$ after the first exposure. There are also studies on fabrication methods of nanostructures based on multiple exposures with different sample rotation angles (φ) in between.

The general fabrication process of our devices is shown in **Figure 1-5**. Silicon and glass substrates are cleaned using acetone for 15 minutes then iso-propyl alcohol (IPA) for 10 minutes followed by deionized (DI) water for 2 minutes. The cleaned samples are dried with nitrogen gas. Then, thin-film deposition methods such as sputtering and e-beam evaporation are used to deposit Si_3N_4, Si, TiO_2, and Au thin films on cleaned substrates. Both positive and negative resists are used for gratings with different parameters. Photoresist coating is carried

out by a spin coater. To obtain grating fill-factor bigger than 50%, we use negative PR (UVN-30). On the other hand, to fabricate gratings with fill factor smaller than 50%, a positive photoresist (SEPR-701) is spin-coated at different spin speeds based on the final PR thickness desired. The spin-coated substrates are then soft baked for 90 seconds at 110°C followed by patterning using LIL method. We develop the exposed photoresist film in specific developers such as AZ 917 MIF to create a resist mask on the thin film. The mask patterns transfer to the film via a reactive-ion-etch (RIE) process using our Oxford PlasmaLab 80 RIE system. Different recipes are used to etch different materials. For instance, gas mixture of SF_6 (14 sccm) and CHF_3 (38 sccm) for 7 minutes with RIE power of 100 W gives an etch rate of about 30 nm/min for Si films. Subsequently, residual photoresist is removed by O_2 ashing process in the RIE chamber.

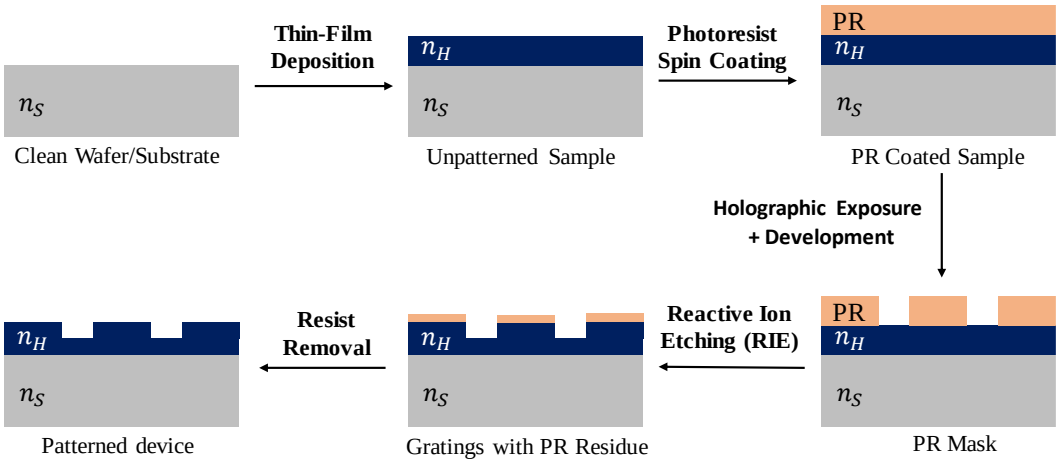

Figure 1-5 Standard fabrication process of our periodic metasurfaces.

1.4.1 Nanoimprint lithography (NIL)

Nanoimprint lithography (NIL) exploits flexible patterned stamps fabricated from suitable masters. Patterns on a given stamp can thus be transferred to resist or other imprint materials and, consequently, either heat or UV light can accomplish the curing process. A peel-off process can be implemented after curing of the imprinted material and the resulting structure, which has dimensions defined by the original master, acts as the final device. The strengths of this process compare well with other traditional lithography methods such as holographic interference patterning or e-beam writing and include cost-effective parallel nanofabrication that is fast, simple, repeatable, and mass-production qualified.

To fabricate a master template, a thin layer of photoresist is spin coated on a silicon wafer and patterned via the laser interference lithography method. Subsequently, development of the patterned photoresist and a reactive-ion etch (RIE) process enable transfer of patterns from the photoresist to a silicon wafer. A thin layer (~20 nm) of sputtered aluminum followed by an anti-adhesion chemical (dichloromethane) may be coated on the patterned silicon wafer to enhance the peel off process.

Polydimethylsiloxane (PDMS) is used to make the stamp that contains a negative pattern of the master template. Sylgard 184 silicone elastomer is mixed in a 10:1 ratio of base and curing agent. Then it is cast on a master template and degassed under vacuum until no visible bubbles are observed followed by curing at

75 °C for 4 hours. It is then peeled off from the master to complete the stamp (thickness~0.5 cm). In our study, the UV-curable adhesive acts as an imprint material, which is patterned with the PDMS stamp. The pattern is transferred via the curing and peel-off process with the PDMS.

1.5 Characterization methods

We use Park XE-70 atomic force microscopy (AFM) and JEOL JSM-7600F field emission scanning electron microscopy (SEM) measurements to verify the final device dimensions. **Figure 1-6** shows AFM images pertinent to 1D and 2D fabricated devices by the LIL method. The SEM images reveal-high quality grating lines in two different magnifications as shown in **Figure 1-7.** In addition, a Woolam VASE ellipsometer is used to measure the thickness and optical constant of the thin films.

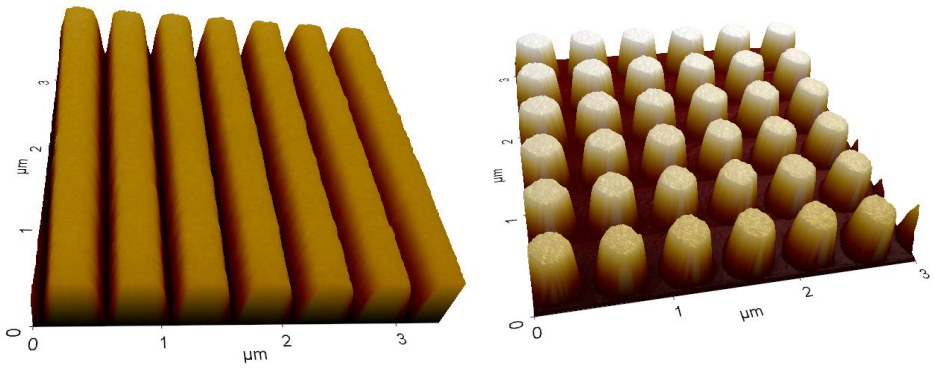

Figure 1-6 AFM images of the 1D and 2D gratings.

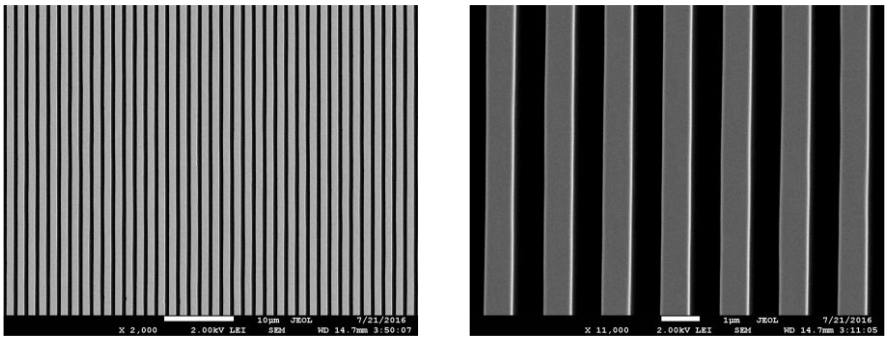

Figure 1-7 SEM images of the 1D grating at two different magnifications.

To measure the transmission spectra of the fabricated devices and investigate their actual performance, we employ a supercontinuum light source (Koheras SuperK Compact) to produce an incident beam and optical spectrum analyzer (OSA; Yokogawa AQ6375) to detect the transmitted light. Polarized transmission measurements of the fabricated samples (signal power) are made by inserting a Glan-Thompson polarizer (Thorlabs). Normalized transmission spectra for fabricated samples pertinent to both TE and TM incident waves are calculated by dividing the signal power by the input power measured via the detector. The rotation stage is used for angular spectral measurement of the device. The schematic of the experimental setup used to measure zero-order transmission (T_0) is shown in **Fig 1-8**.

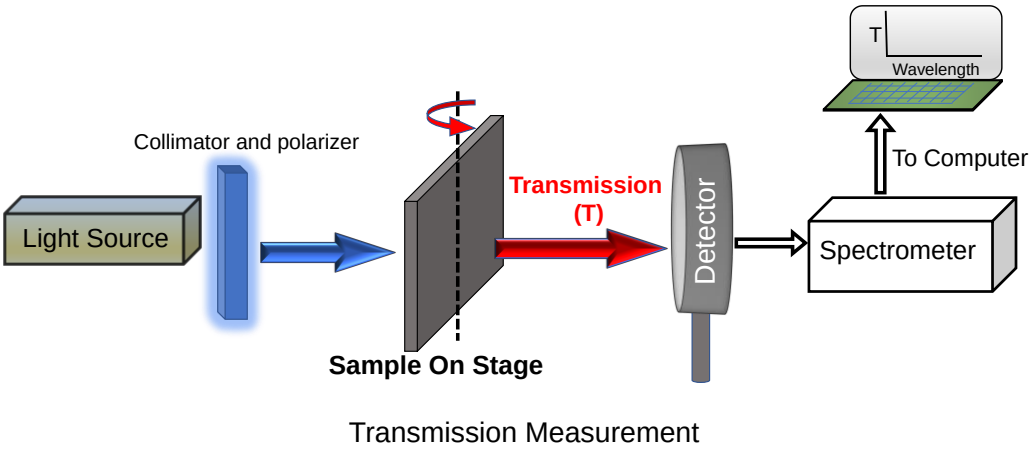

Figure 1-8 Schematic of a general transmission measurement setup.

1.6 Dissertation Overview

In this dissertation, theoretical and experimental studies on various new types of GMR-based metasurfaces are presented. Various design/simulation tools (RCWA, FDTD, PSO), micro/nano patterning methods (laser-interference lithography (LIL), nanoimprint lithography (NIL)), thin film deposition techniques (sputtering, e-beam evaporation, spin coating), etching methods (dry etch and wet etch), and optical/structural characterization techniques (ellipsometry, SEM, AFM, FTIR, DLS, OSA) are utilized in developing content for the subsequent chapters.

Chapter 2 establishes theoretical framework to systematically describe subwavelength resonance behavior and to predict the optical response of resonant photonic lattices using the full Rytov solutions. We show that Rytov's original effective-medium theory (EMT) is far more general and useful than previously thought and the full Rytov formulation implicitly contains refractive-index

solutions pertaining directly to evanescent waves that drive the laterally-propagating Bloch modes foundational to resonant lattice properties. This insight is useful in modeling guided-mode resonant devices including wideband reflectors, bandpass filters, and polarizers. As an additional result, we define a clear transition point between the resonance subwavelength region and the deep-subwavelength region with an analytic formula provided in a special case.

Chapter 3 presents design and fabrication of a new class of polarizers that are extremely compact and efficient. Based on an elemental low-loss single-resonant grating, we develop multilayer modules providing ultrahigh extinction ratio polarizers. The elemental polarizer contains a subwavelength periodic pattern of crystalline silicon on a quartz substrate. A stack of two dual-grating modules exhibits a measured extinction ratio (ER) of ∼100,000 in a sparse 2-mm-thick device across a bandwidth of ∼50 nm in the telecommunications spectral region. Theoretical computations indicate that extreme values of extinction are possible.

Chapter 4 provides an experimental demonstration of high-quality nanocomposites enabling convenient imprinting of nanopatterned optical devices. The nanocomposite developed contains homogeneously dispersed surface functionalized silicon (Si) nanoparticles in a UV-curable prepolymer host medium. Using an optical adhesive NOA73 as host eliminates surface treatment of the silicone mold due to minimal adhesion between the polymer and mold. Moreover, the chosen materials exhibit low shrinkage, enabling faithful replication of the

master templates. Tunable refractive index is realized by mixtures of the host polymer with a refractive index of ~1.56 and nanoparticles with a refractive index of ~3.45.

Chapter 5 provides a novel route towards facile fabrication of complex periodic metasurfaces based on sequential exposures by laser interference lithography. We propose a fabrication method which is fast, cost-effective, and can be applied to large surface areas. It is enabled by precise control over periodicity and exposure energy. With it we have successfully patterned and fabricated one-dimensional (1D) and two-dimensional (2D) multipart unit cell devices. Furthermore, it is shown that this method of fabrication can be implemented not only to pattern periodic symmetric/asymmetric designs but also to realize non-periodic metasurfaces.

Chapter 6 contains the properties of photonic devices fashioned with dual-grating metamaterials. We show that the resonance signatures are sensitively controlled by the relative parameters of the periodic regions. In particular, if they are physically identical and separated by a half-wavelength, there ensues a bound state in the continuum (BIC) with extremely narrow resonance linewidth. At grating-depth and thickness values satisfying Avrutsky's model, three different types of BICs are supported by a single metamembrane. Two BICs appear at normal incidence at the Γ point with one being a quasi-BIC on one band edge while a true symmetry-protected BIC resides on the other edge. Moreover, a quasi-BIC state

away from the Γ point in the same device is demonstrated. Whereas these results are based on a simple model with 1D periodicity, the primary properties will carry over to general 2D/3D photonic lattices.

Chapter 7 shows a considerable advance in this technology, as we experimentally demonstrate efficient fiber-facet mounted device prototypes. To retain a large aperture for convenient coupling, we design and fabricate silicon nitride-based resonators on the tip of a multimode fiber. We account for light propagation along the multimode fiber with exact numerical methods. This establishes the correct amplitude and phase distribution of the beam incident on the tip-mounted GMR element, thus enabling us to properly predict the resonance response. To fabricate the integrated GMR structures on the tips of fibers, we employ standard microfabrication processes, including holographic interference lithography and reactive-ion etching. The experimental results agree with simulation with an example device achieving high efficiency of ~77% in transmission. To investigate fiber sensor operation, an etched silicon nitride fiber tip filter is surrounded with solutions of various refractive indices, yielding an approximate sensitivity of 200 nm/RIU.

Chapter 2

Effective-medium formalism and exact solutions

Periodic photonic lattices, known as diffraction gratings for 100 years and diffractive optical elements for decades, have a venerable history [1-14]. With major discoveries in optical physics deriving from their deployment, periodic structures enable wide application fields including spectroscopy, laser technology, and sensors. Imbuing the lattice with waveguiding capability offers yet another set of functionalities grounded in resonance effects due to excitation of lateral leaky Bloch modes [3-6,15-19]. In the recent past, periodic photonic lattices are often referred to as "metasurfaces" or "metamaterials" in which periodically aligned wavelength-scale features enable manipulation of an incoming electromagnetic waves in a desired manner [20-24]. Resonant lattices offer novel properties and light-wave control in compact format potentially replacing and complementing conventional optical devices.

Extensive theoretical and experimental studies have been conducted to realize resonant and nonresonant periodic structures in materials systems pertinent to the various spectral regions. Whereas various wavelength (λ) to periodicity (Λ) ratios can be deployed, working in the subwavelength regime offers a particularly efficient optical response. Transition from the non-subwavelength to the subwavelength regime occurs at the Rayleigh wavelength (λ_R) [2]. For wavelength values longer than λ_R, all higher diffraction orders are eliminated and only the zero

orders propagate in the cover and substrate media. In the subwavelength regime, one can define two main regions. These are the deep-subwavelength region where the wavelength is much larger than the period, showing thin-film effects on account of a high degree of homogenization, and the resonant subwavelength region where the wavelength-scale periodicity triggers guided-mode, or leaky-mode, resonance effects. These regions are shown schematically in **Figure 2-1(a)**. While the Rayleigh wavelength is known by $\lambda_R = n_S \Lambda$, there exists no definition for this transition wavelength that we refer to as a cutoff wavelength (λ_c); here, we propose a definition for this value.

Since the seminal work by Rytov in 1956, the effective refractive indices of subwavelength gratings can be calculated for both transverse electric (TE) and transverse magnetic (TM) polarization states [25]. His effective-medium theory (EMT) applies to an infinite periodic halfspace. Treating continuity and periodicity of the electromagnetic fields at boundaries between constituent materials in a unit cell results in polarization-dependent transcendental equations. Employing a series expansion for the tangent term in the transcendental equations returns the well-known zero-order, second-order, or higher-order approximate solutions for effective refractive indices. Applying EMT based on the approximated Rytov formulation, one can replace a subwavelength grating by an equivalent homogeneous film with corresponding effective refractive indices for each polarization. This process is noted schematically in **Figures 2-1(b) and 2-1(c)**. The

thickness of the homogeneous film is identical to the grating thickness. In the deep subwavelength, or quasi-static, limit $\lambda/\Lambda \rightarrow \infty$, the zero-order effective refractive indices result in a reliable solution in terms of equivalent reflection, transmission, and phase calculations. Notably, in 1986, Gaylord et al. implemented zero-order EMT to approximate subwavelength gratings with a single homogeneous layer in order to design an antireflection coating at normal incidence [26]. In a related work, Ono et al. approximated a sinusoidal ultrahigh spatial frequency grating by several rectangular grating layers with different fill factors to design an antireflection structure [27]. They calculated the refractive index of each rectangular layer using the zero-order approximation. However, the zero-order approximation fails for wavelengths outside the deep subwavelength regime. Therefore, as the value of λ/Λ approaches the resonant subwavelength regime (i.e. $\lambda \sim \Lambda$) higher-order approximations must be used. Thus, Richter et al. used second-order EMT to design and study optical elements with a form birefringent structure [28]. Moreover, Raguin and Morris utilized second-order EMT to design antireflection surfaces in the infrared (IR) electromagnetic bands [29].

All previous EMT studies [26-34] based on Rytov's formulation [25], with either exact or approximated solutions, have reported only one effective refractive index for each wavelength as depicted in **Figure 2-1(d)**. In contrast, here, we report that solving the exact transcendental equation in the resonant subwavelength regime can result in several effective refractive indices for a single wavelength.

Mathematically, since tan(x) has an infinite sets of roots, this may not come as a surprise. What is surprising is that these roots are highly applicable to practical problems modeling photonic lattices with finite thickness, namely metasurfaces and metameterials, as we show in detail in the remainder of the study. These higher-order solutions have been completely ignored thus far to our knowledge. Even Rytov himself paid no attention to them and proceeded to derive simplified approximate expressions based on the zeroth root [25]. In his case, this is understandable as resonant photonic lattices were not known at that time.

Henceforth, we establish our theoretical framework to systematically describe subwavelength resonance behavior and predict the optical response of resonant photonic lattices using the full Rytov solutions. Expeditious results are obtained because of Rytov's semi-analytical formulation with direct, new physical insights available for resonant lattice properties. To prove the correctness of the proposed approach, we compare our semianalytical results with rigorously computed results and show excellent agreement between them. Our solutions, based on the exact symmetric Rytov problem, are previewed schematically in **Figure 2-1(e)**. Most importantly, we show here that the higher Rytov solutions n_m^{EMT} correspond exactly to reradiated fields generated by higher-order evanescent diffracted waves represented as S_m, m=±1, ±2, …, driving the resonance process [7,8,35].

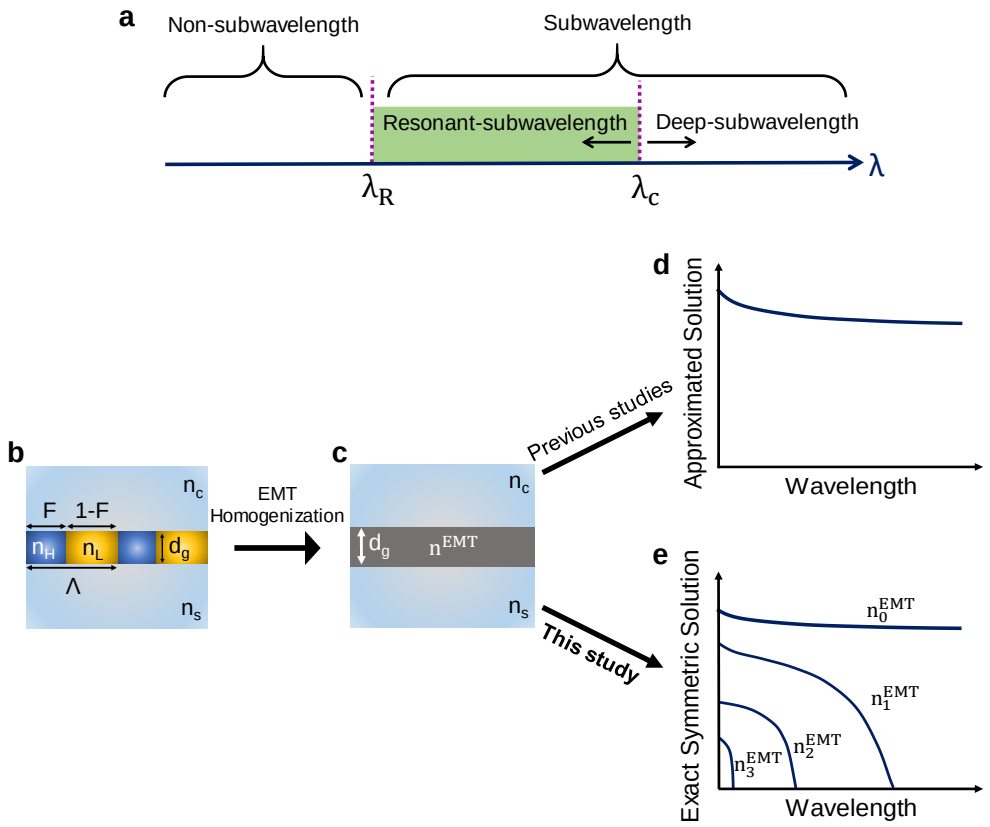

Figure 2-1 Diffraction regimes and exact Rytov EMT. Schematics illustrating (a) the diffraction regimes pertaining to Rytov's solutions, (b) the general rectangular grating model, (c) equivalent thin-film EMT model, (d) the zeroth-root Rytov solution basic to all past EMT models, (e) calculated effective refractive indices presented in this study based on the exact Rytov formalism.

2.1 Rytov refractive indices and their interpretation

We first review the Rytov formalism [25] for TE polarization, where the electric-field vector is parallel to the grating lines. The full formula for a rectangular grating structure with infinite thickness is derived by considering the continuity of

the electric and magnetic fields at boundaries between the ridges and grooves. There results a transcendental equation given by

$$\left(1+\kappa^2\right)\sin(\alpha_1 a)\sin(\alpha_2 \mathrm{b})+2\kappa\left(1-\cos(\alpha_1 a)\cos(\alpha_2 \mathrm{b})\right)=0 \qquad (2.1)$$

where $\alpha_1 = k_0\sqrt{n_H^2-(n_{TE}^{EMT})^2}$, $\alpha_2 = k_0\sqrt{n_L^2-(n_{TE}^{EMT})^2}$, $k_0 = 2\pi/\lambda_0$, $\kappa = \alpha_1/\alpha_2$, and n_{TE}^{EMT} represents the effective refractive index for the TE case. The parameters a and b are the widths of the grating constituents with refractive indices n_H and n_L, respectively. Based on this, one can define parameters F=a/Λ and 1-F=b/Λ as fill factors of each section in a unit cell as shown in **Figure 2-2(a)**. Since symmetric rectangular gratings are considered in Rytov's model, he extracted solutions from the full formula Eq. (2.1) that are pertinent to symmetric field distributions inside the grating. Accordingly, Eq. (2.1) is reduced to Eq. (2.2) which we reference here as the "exact" Rytov formulation for TE polarization.

$$\sqrt{\mathrm{n}_L^2-(\mathrm{n}_{TE}^{EMT})^2}\tan\left[\frac{\pi\Lambda}{\lambda}(1-F)\sqrt{\mathrm{n}_L^2-(\mathrm{n}_{TE}^{EMT})^2}\right]=-\sqrt{\mathrm{n}_H^2-(\mathrm{n}_{TE}^{EMT})^2}\tan\left[\frac{\pi\Lambda}{\lambda}F\sqrt{\mathrm{n}_H^2-(\mathrm{n}_{TE}^{EMT})^2}\right] \qquad (2.2)$$

Similarly, for TM polarization, where the magnetic-field vector is parallel to the grating lines, there results

$$\frac{\sqrt{\mathrm{n}_L^2-(\mathrm{n}_{TM}^{EMT})^2}}{\mathrm{n}_L^2}\tan\left[\frac{\pi\Lambda}{\lambda}(1-F)\sqrt{\mathrm{n}_L^2-(\mathrm{n}_{TM}^{EMT})^2}\right]=-\frac{\sqrt{\mathrm{n}_H^2-(\mathrm{n}_{TM}^{EMT})^2}}{\mathrm{n}_H^2}\tan\left[\frac{\pi\Lambda}{\lambda}F\sqrt{\mathrm{n}_H^2-(\mathrm{n}_{TM}^{EMT})^2}\right] \qquad (2.3)$$

Solving the exact Rytov equations, Eq. (2.2) and Eq. (2.3), for n_{TE}^{EMT} and n_{TM}^{EMT} delivers a set of effective refractive indices that depend on the wavelength

and the input design parameters. In principle, due to the periodicity of tan(x), there exists an infinite number of solutions; in practice, a few of the lowest-order solutions will be useful. Except for n_0^{EMT}, the effective refractive indices have specific cutoff wavelengths. Knowing the cutoff wavelengths is key to predicting the optical response as shown here. Working at wavelengths longer than the Rayleigh wavelength $\lambda_R=n_S\Lambda$, ensures zero-order propagation towards the cover and substrate with all higher-order diffracted waves being evanescent. These higher diffraction orders propagate in the periodic region depending on the structural design and corresponding cutoff values of λ_c^m.

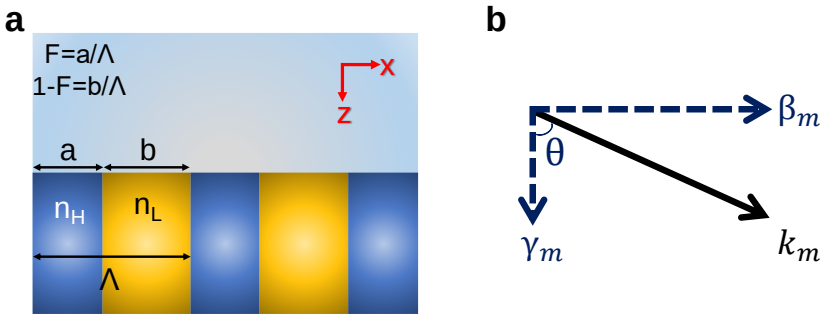

Figure 2-2 Half-space grating structure. (a) Schematic of the half space grating model in Rytov's formulation with an infinite number of periods along the X direction. (b) Wavevector of the m^{th} diffracted order accompanied by its vertical (Z direction) and horizontal (X direction) components.

In the periodic region, the fundamental coupled wave expansion of the y-component of the electric field can be written as [14,36]

$$E_y(x,z)=\sum_m S_m(z)\exp[-i(k-mK)x)] \tag{2.4}$$

where $S_m(z)$ are the amplitudes of the space-harmonic components in the Fourier series expansion of the total field in periodic direction, k is the wave vector of a diffracted wave, and $K=2\pi/\Lambda$ is the grating vector magnitude. Each diffracted order possesses a wavevector (k_m) in the direction of propagation which can be resolved into vertical and horizontal components as depicted in **Figure 2-2(b)**. Effective refractive indices obtained by solving the Rytov equations pertain to the vertical components of the diffracted orders belonging to k_m. We have

$$k_m^2 = \beta_m^2 + \gamma_m^2 \tag{2.5}$$

where $\beta_m = k_m \sin\theta$, $\gamma_m = k_m \cos\theta$, $k_m = k_0 n_m(\lambda_0)$, and $k_0 = 2\pi/\lambda_0$. Defining $N_m(\lambda_0) = \beta_m/k_0 = n_m(\lambda_0)\sin\theta$ and $n_m^{EMT}(\lambda_0) = \gamma_m/k_0 = n_m(\lambda_0)\cos\theta$, a relation is obtained between the component refractive indices of **Figure 2-2(b)** as

$$\left(n_m(\lambda_0)\right)^2 = \left(N_m(\lambda_0)\right)^2 + \left(n_m^{EMT}(\lambda_0)\right)^2 \tag{2.6}$$

Here, n_m is the refractive index experienced by a diffracted wave with wavevector k_m. In the geometry of a periodic waveguide, N_m represents the lateral effective index seen by the m^{th} Bloch mode whereas n_m^{EMT} refers to the vertical effective index seen by the resonant reradiated Bloch modes.

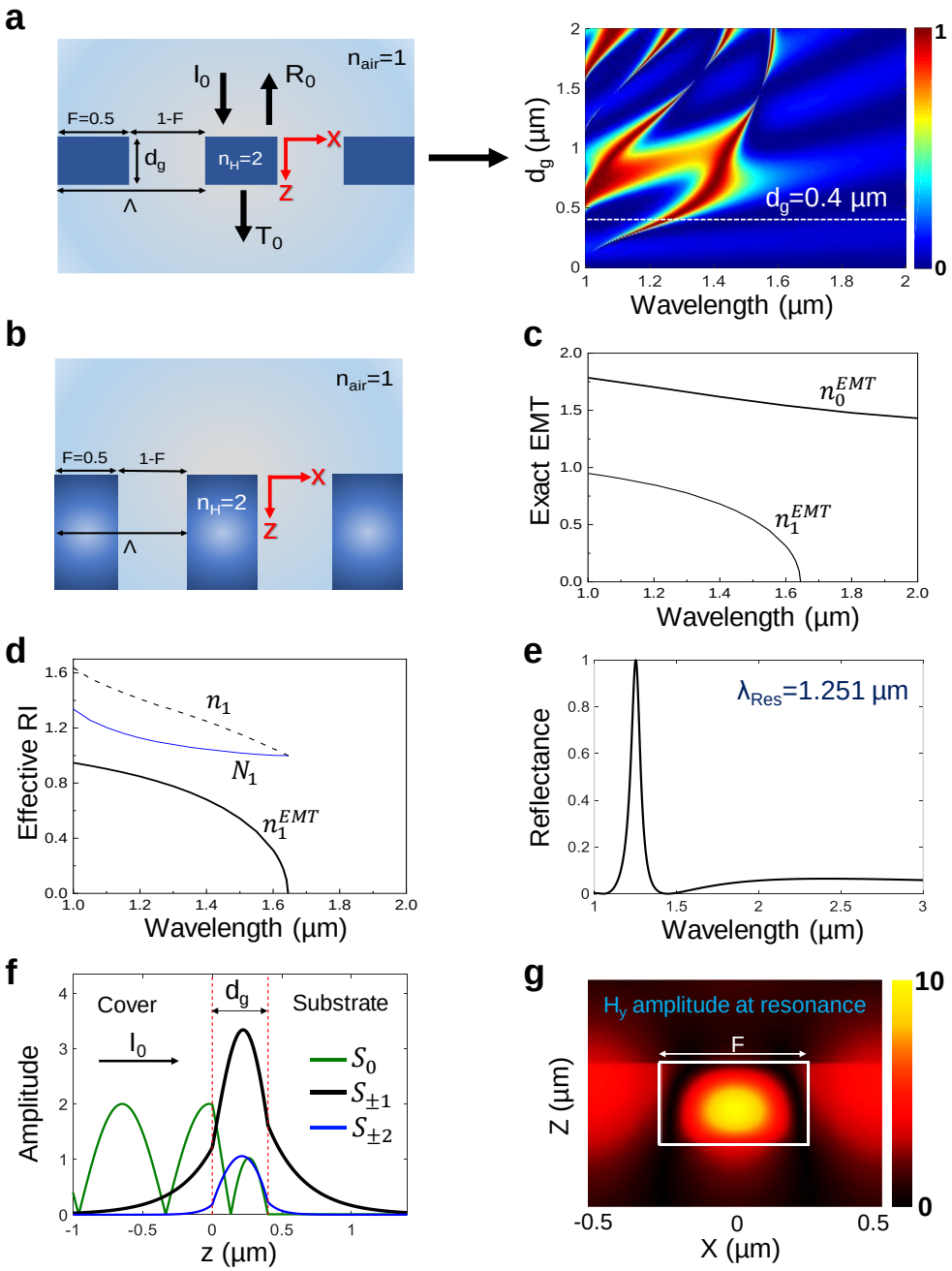

Figure 2-3 Rytov model and practical device geometries. (a) Schematic of a representative grating membrane and corresponding RCWA-based reflection map as a function of grating thickness (d_g) for TM-polarized incident light, (b) schematic of the half-space grating model, (c) calculated exact effective refractive indices, (d) wavelength dependent effective refractive indices of waveguide (n_1), horizontal

component (N_1), and vertical component (n_1^{EMT}) based on Eq. (2.6), (e) simulated reflectance spectrum of a grating with d_g =0.4 μm, (f) amplitude of the coupled diffracted orders at resonance wavelength of λ_{Res}=1.251 μm, and (g) distribution of total magnetic field in one period at the resonance wavelength of λ_{Res}=1.251 μm showing TM_0 mode shape. The grating structure has constant parameters of Λ= 1 μm, F=0.5, n_H=2, and n_L= n_c =n_s=1.

The objective of **Figure 2-3** is to connect the Rytov model with practical device geometry as applied in metamaterials presently. Accordingly, **Figure 2-3(a)** shows an example grating membrane structure enclosed by air and its reflection spectrum mapped in wavelength versus grating thickness (d_g). This spectrum is computed with rigorous coupled-wave analysis (RCWA) [14,36]. The corresponding half-space grating structure used in the Rytov model is presented in **Figure 2-3(b)**. The effective refractive indices n_m^{EMT} obtained by solving the exact Rytov Eq. (2.3) are shown in **Figure 2-3(c)**. The values of n_m^{EMT} denote vertical components of the refractive indices n_m that quasi-guided evanescent-wave diffraction orders see in the direction of propagation in the periodic medium. These evanescent diffraction orders excite lateral leaky Bloch modes that generate the guided-mode resonance. Comparing the rigorously-computed resonance map in **Figure 2-3(a)** to **Figure 2-3(c)** shows that no resonance occurs in the region where n_1^{EMT}=0. Moreover, using Eq. (2.6) with values of n_m^{EMT} obtained by the exact Rytov formula, one can find the corresponding pairs of n_m and N_m satisfying the eigenvalue equation of the equivalent homogeneous slab waveguide [6]. **Figure 2-3(d)** depicts these values as a function of wavelength for an equivalent waveguide having a thickness of d_g= 0.4

μm. It can be inferred from this figure that the cutoff wavelength occurs when the refractive index of the waveguide reaches $n_m=n_{air}=1$ at which point the waveguide vanishes. Thus, at the cutoff wavelength, the refractive index contrast becomes zero such that no waveguide mode can be supported. For the grating design of **Figure 2-3(a)** with d_g= 0.4 μm, the resonance manifests as a reflection peak at λ_{Res}= 1.251 μm as shown in **Figure 2-3(e)**. At the resonance wavelength, one can compute with RCWA the amplitudes of the coupled diffracted orders and simulate the magnetic-field distribution as shown in **Figures 2-3(f)** and **2-3(g)**, respectively. It is clearly illustrated that the dominant contribution to the internal modal field, whose cross-section is shown in **Figure 2-3(f)**, is due to the evanescent diffraction orders with amplitudes $S_{\pm 1}$ which is also completely consistent with the total magnetic-field distribution illustrated in **Figure 2-3(g)**. Interestingly, this point can be predicted and explained directly via **Figure 2-3(c)**; as the resonance wavelength falls below the cutoff wavelength of the first diffracted order (λ_c^1), we would expect the first diffracted orders $S_{\pm 1}(z)$ to be responsible for the resonance because it is this order that experiences n_1^{EMT}.

2.2 Rytov solutions for cutoff wavelengths

Knowing the values for the cutoff wavelengths is important to distinguish the deep-subwavelength and resonant-subwavelength regions. Moreover, the cutoff wavelengths define the spectral location where a new evanescent diffraction order, with attendant lateral Bloch-mode excitation, enters and begins to participate in the

resonance dynamics. The cutoff wavelengths λ_c^m occur when the vertical effective refractive index of diffraction order m vanishes (i.e., $n_m^{EMT} = 0$). The semianalytical Rytov formulas can be used to determine the first and higher cutoff wavelengths for any one-dimensional lattice. Therefore, plugging $n_{TE}^{EMT} = 0$ into the exact Rytov formulation, for example Eq. (2.2) for TE polarization, yields

$$n_L \tan\left[\frac{\pi\Lambda}{\lambda}(1-F)\,n_L\right] = -n_H \tan\left[\frac{\pi\Lambda}{\lambda}F\,n_H\right] \tag{2.7}$$

In general, there is no analytical solution for this equation. However, here we show that for specific design parameters one can straightforwardly and analytically calculate the cutoff wavelengths for each diffracted order. This works when the arguments of the tangent functions on each side of Eq. (2.7) become identical

$$(1-F)n_L = Fn_H \tag{2.8}$$

Once this condition is satisfied, Eq. (2.7) holds for values of the tangent arguments equal to $m\pi/2$ (m=1, 2, 3, …) which results in closed-form, simple analytical solutions

$$\lambda_c^m = \frac{2}{m}\Lambda F n_H \tag{2.9}$$

giving the cutoff wavelength for each diffraction order. All photonic lattices supporting guided-mode resonance admit at least the first evanescent diffraction order. Thus, with m=1, we get $\lambda_c^1 = 2\Lambda F n_H$. This is a remarkable canonical result.

From Eq. (2.8), appropriate fill factors satisfying these solutions are $F=n_L/(n_L+n_H)$. These values of F are therefore reasonable for experimental realization. In the subwavelength regime, to ensure that at least one resonance arises from the m^{th} diffraction order, the Rayleigh wavelength should be smaller than the cutoff wavelength (i.e., $\lambda_R < \lambda_c^m$). This yields a constraint $F > n_s/2n_H$ for m=1. Previously, Lalanne et al. obtained a numerical solution for λ_c^1 and pointed out its analogy with the Rayleigh wavelength [15]. One significant point in our solution is that the cutoff wavelengths are fixed and will not change with changes in the refractive index of the cover and substrate.

In this spirit, one can engineer the spectral response and the number of diffracted orders at work by appropriately choosing the values of λ_R and λ_c^m for grating design. For example, the grating design depicted in **Figure 2-4(a)** having parameters F=1/3, Λ=1 μm, n_H=2, and n_L=1 satisfies Eq. (2.8). Thus, the cutoff wavelengths for each evanescent diffracted order can be obtained analytically as expressed in Eq. (2.9) which returns values of λ_c^1=4/3~1.33 μm and λ_c^2=2/3~0.66 μm for the first two orders. The Rayleigh wavelength of this design is λ_R=1 μm which is smaller than the first order cutoff wavelength λ_c^1=4/3~1.33 μm.

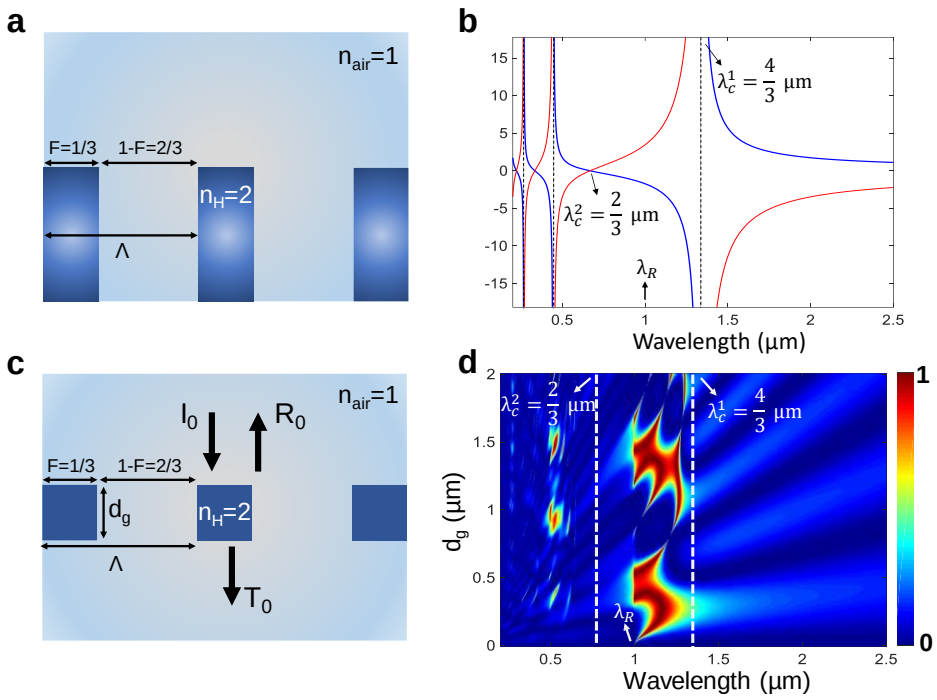

Figure 2-4 Grating design with parameters satisfying conditions for an analytic study. (a) Schematic of the half-space grating model, (b) graphical solution of Eq. (2.7) to find the cutoff wavelengths of the diffracted waves in the grating region, (c) schematic of a grating membrane with finite thickness, and (d) corresponding reflection map as a function of grating thickness (d_g).

To validate the accuracy of our method, it is seen in **Figure 2-4(b)** that graphical solutions of Eq. (2.7), give the exact same values as obtained analytically by Eq. (2.9). **Figure 2-4(c)** shows a schematic of a grating membrane surrounded by air (n_{air}=1) with finite thickness of d_g. For this design, the cutoff wavelengths shown by dashed lines in **Figure 2-4(d)**, which is a RCWA-simulated reflection map, are in full agreement with the analytical cutoff values.

2.3 Relevance of Rytov's formulation to resonance device design

In this section, we show that the Rytov effective refractive indices are directly applicable to design of periodic photonic devices, including metamaterials and metasurfaces. Their deployment fully supports prior explanations of resonance device physics in terms of lateral leaky Bloch modes and guided-mode resonance [7,8,35]. Their existence and spectral expressions are not consistent with resonance effects caused by local modes including Fabry-Perot resonance or Mie scattering [37, 38]. Here, we treat example devices whose spectra and functionality are directly explainable using the Rytov indices.

2.3.1 Wideband resonant reflector

One particularly useful device is the wideband resonant reflector in which nanopatterned design provides high reflectivity approaching 100% over a wide wavelength range [7,39]. Numerous studies have addressed these compact, often single-layer, reflectors both theoretically and experimentally for various optical wavebands [15,35,38-41]. Here, we apply the Rytov indices to substantiate the physical basis for the wideband reflection behavior. In this context, the half-space grating structure with parameters shown in **Figure 2-5(a)** is considered for the analysis. Corresponding roots of the exact Rytov equations for both TM and TE polarization states are found and the results are shown in **Figures 2-5(b)** and **2-5(c)**, respectively. Similar curves were obtained by Lalanne et al. [15] using an RCWA-

based numerical algorithm. For the TM case shown in Fig. 5(b), there are two significant points to be considered. The first one concerns the values of the cutoff wavelengths for each guided diffracted order and the second pertains to the shape of the index curves. For instance, it is illustrated in **Figure 2-5(b)** that in the wavelength range of 1.25 μm to 3 μm, beyond the cutoff wavelength of the second order, only n_0^{EMT} and n_1^{EMT} exist in the effective refractive index diagram. Consequently, these two orders with m=0 and m=1 are responsible for all important spectral properties. Furthermore, it is seen that the slopes of the curves are almost identical with both curves varying monotonically in a wide wavelength range depicted by the gray region in **Figure 2-5(b)**. This is a key point to achieve wideband reflector response as the wavelength dependent phase difference ($\Delta\varphi$) accumulated in the z direction between these two orders at work is defined by $\Delta\varphi=(2\pi/\lambda_0)(n_0^{EMT}(\lambda_0) - n_1^{EMT}(\lambda_0))\, d_g$ which is proportional to the effective refractive-index difference of the first two orders obtained by the exact Rytov expression. Therefore, our method enables prediction as to whether to expect a wideband reflector behavior from a one-dimensional grating structure, simply by calculating effective refractive index graphs without performing any rigorous numerical simulations. The closed-form Rytov formulas might thus substantiate efficient design methods. Applying this approach to **Figure 2-5(c)**, it is seen directly that no wideband reflection response will arise out of this design for TE polarization as the slopes of the two curves differ significantly. To confirm our

hypothesis, we performed RCWA-based simulations for the structure shown in **Figure 2-5(d)**. Simulated zero-order reflection maps of this grating design for TM and TE cases are shown in **Figures. 2-5(e)** and **2-5(f)**, respectively. These maps validate our predictions of wideband reflection response occurring in TM polarization but no wideband reflection response for the TE case. Wideband reflectors are related to the regions with dark red colors in a wide wavelength range. These appear in the TM map at some specific grating thicknesses d_g which provide an appropriate phase difference (completely in phase) for high reflection since $\Delta\varphi \propto d_g$. Explanation of wideband resonance reflection applying the spectral phase pertinent to similar, albeit numerically-simulated, effective indices was first provided by Lalanne et al. [15].

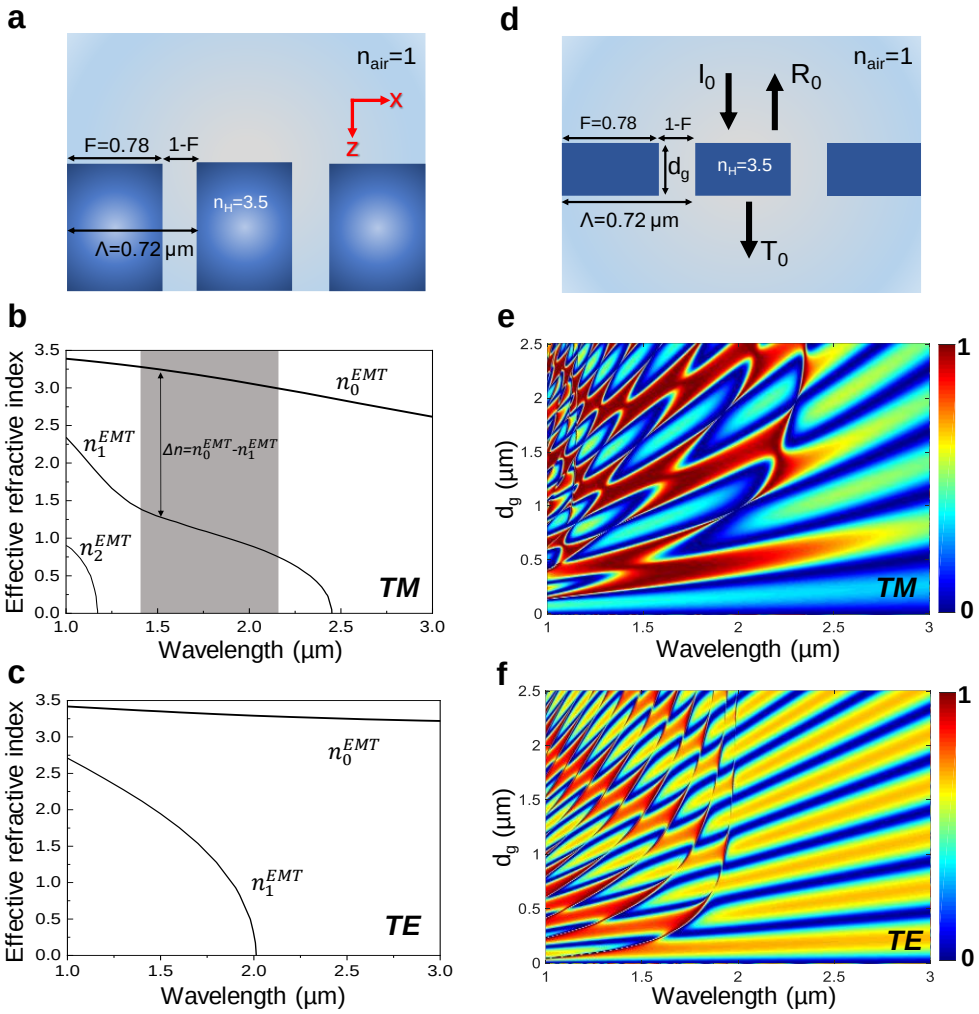

Figure 2-5 An example demonstrating the use of the Rytov indices for design of a wideband resonant reflector. (a) Schematic of the half-space model. Calculated effective refractive indices using the Rytov formalism for (b) TM-polarization, and (c) TE-polarization states. (d) A schematic of a corresponding grating membrane with parameters Λ= 0.72 μm, F=0.78, n_H=3.5, and n_L= n_{air}=1. Simulated reflection maps in wavelength versus grating thickness (d_g) pertinent to normally-incident (e) TM-polarized, and (f) TE-polarized light. In the maps, dark red color implies R_0 approaching 1.

2.3.2 Guided-mode resonant bandpass filter

Another important grating-based optical device is the sparse, single-layer bandpass filter (BPF) exhibiting low transmission sidebands and high-efficiency narrow-band transmission peak [42-45]. Low transmission sidebands and a transmission resonance peak correspond to a wideband high-reflection background and a reflection resonance dip, respectively. To study this device type, a half-space model and the corresponding calculated Rytov refractive indices are shown in Fig. 6(a). We choose the grating parameters to satisfy Eq. (2.8) to analytically obtain the cutoff wavelengths. As in the explanation of the wideband reflector, similarity in the slopes of the n^{EMT} curves enables an appropriate phase difference to obtain high reflectivity at a specific device thickness.

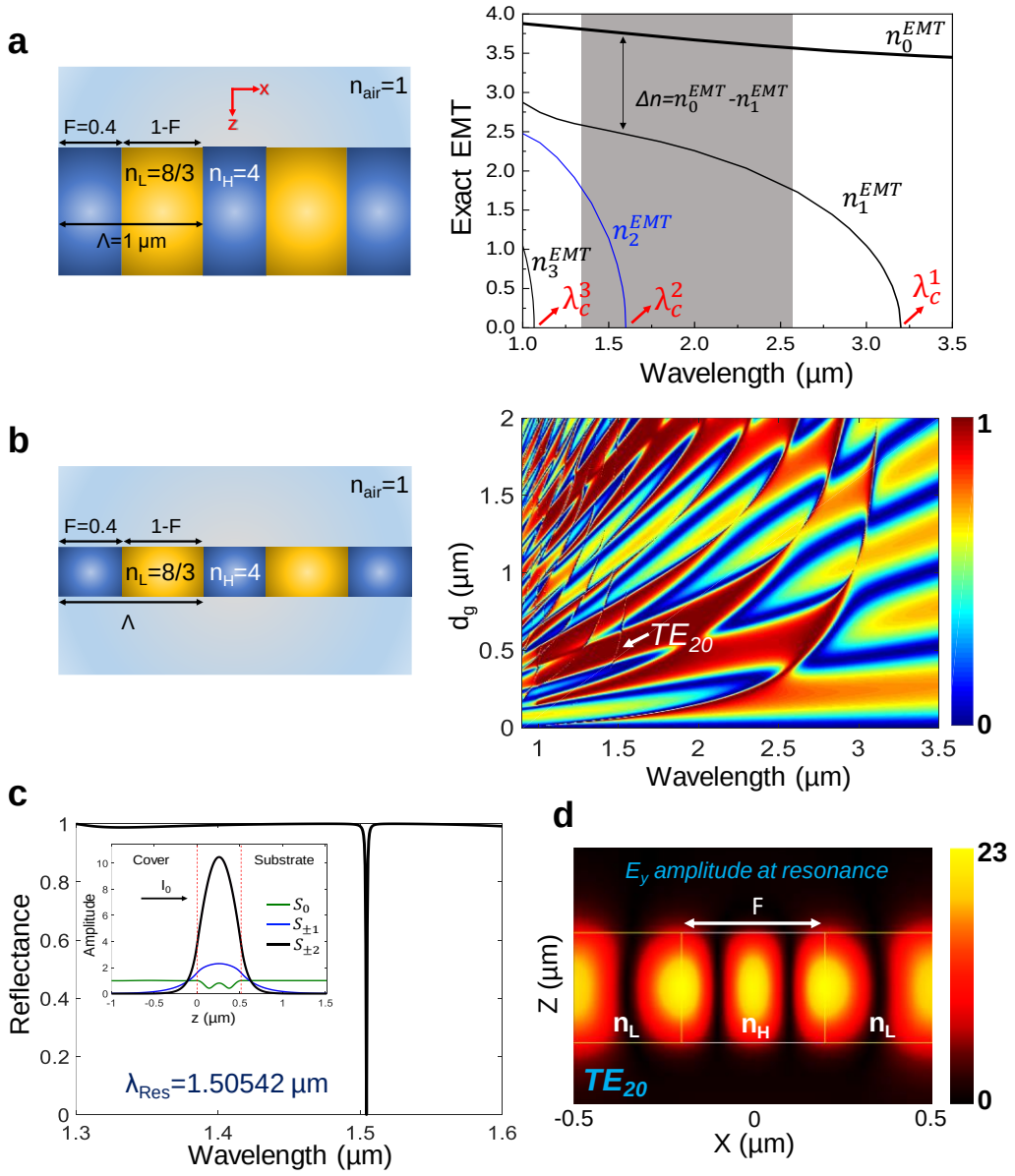

Figure 2-6 Rytov indices in bandpass filter analysis and design. The example filter works in TE polarization with parameters of Λ= 1 μm, F=0.4, n_H=4, and n_L=8/3, and n_{air}=1. (a) Schematic of the Rytov half-space model and calculated effective refractive indices. (b) Schematic of the attendant grating membrane with finite thickness and its simulated reflection map as a function of grating thickness (d_g). (c) Bandpass filter response of the device with grating thickness of d_g=0.51 μm. Inset in (c) shows the amplitudes of the coupling diffracted orders at the resonance

wavelength of λ_{Res}=1.50542 μm. (d) Electric field distribution at resonance exhibiting a TE_{20} profile.

Thus, we expect a wideband reflector response in the wavelength range where $\Delta n/\lambda_0$ is relatively constant. This condition prevails in the gray region of the EMT graph of **Figure 2-6(a)**. This figure is significantly different from **Figure 2-5(b)** in that the gray region in **Figure 2-5(b)** contains only n_0^{EMT} and n_1^{EMT} whereas the gray region in **Figure 2-6(a)** encompasses n_0^{EMT}, n_1^{EMT} and n_2^{EMT}. As n_0^{EMT} and n_1^{EMT} are responsible for a wideband reflection background, bringing the second order n_2^{EMT} to work will manifest as a reflection dip resonance feature in the optical spectrum because it exists within a region of total reflection. **Figure 2-6(b)** shows a schematic of the membrane version of the half-space grating design of **Figure 2-6(a)** and its reflection map as a function of grating thickness. The reflection map agrees well with the analytic solutions for the cutoff wavelengths and with the number of orders at work experiencing n_0^{EMT}, n_1^{EMT}, and n_2^{EMT}. The resonance feature predicted based on the existence of the n_2^{EMT} curve in the effective refractive index graph is marked as TE_{20} in the reflection map of **Figure 2-6(b)**. **Figure 2-6(c)** confirms a bandpass filter response having a wideband high reflection background. At the reflection dip wavelength, the inset in **Figure 2-6(c)** reveals that the second evanescent diffraction order m=2 is dominant showing that a non-zero n_2^{EMT} is key to realizing a bandpass filter. The electric field distribution at the resonance wavelength shown in **Figure 2-6(d)** furthermore indicates TE_{20}

response (fundamental mode excited by the second evanescent order) consistent with our model. In summary, the Rytov treatment of the resonant BPF is fully consistent with, and supports, prior descriptions of BPF physics [42,43,45].

2.3.2 Guided-mode resonance polarizer

The linear resonant polarizer is the final device example presented. In the past, it has been shown that ultra-compact polarizers with high extinction ratios are realizable with resonant gratings [7,46,47]. Treating here a known polarizer [47], the design schematic is shown in **Figure 2-7(a)** displaying a small fill factor (F=0.1) with n_H=3.5 embedded in a medium with refractive index of 1.5 in a way that n_L= n_C= n_S=1.5 under normal incidence. **Figure 2-7(b)** shows computed λ-d_g reflection maps for TE and TM polarization states. At the specific thickness of the grating denoted by the dashed line, TE polarization exhibits high reflection while TM reflectance is suppressed. Reflectance spectra for a grating with thickness d_g=0.54 μm as shown in **Figure 2-7(c)** reveal a good polarizing response in a wavelength range of 1.3-1.5 μm. To elucidate the polarization behavior in the Rytov picture, we calculate TE and TM Rytov indices as presented in **Figure 2-7(d)**. Again, the parallelism of the n_0^{EMT} and n_1^{EMT} curves in TE polarization enables a wideband reflector response. In contrast, for TM polarization in **Figure 2-7(d)** in the working range of the polarizer, only n_0^{EMT} exists. Consequently, we see that no guided-

mode resonance features will occur in the TM case consistent with the simulated reflection map in **Figure 2-7(b)**.

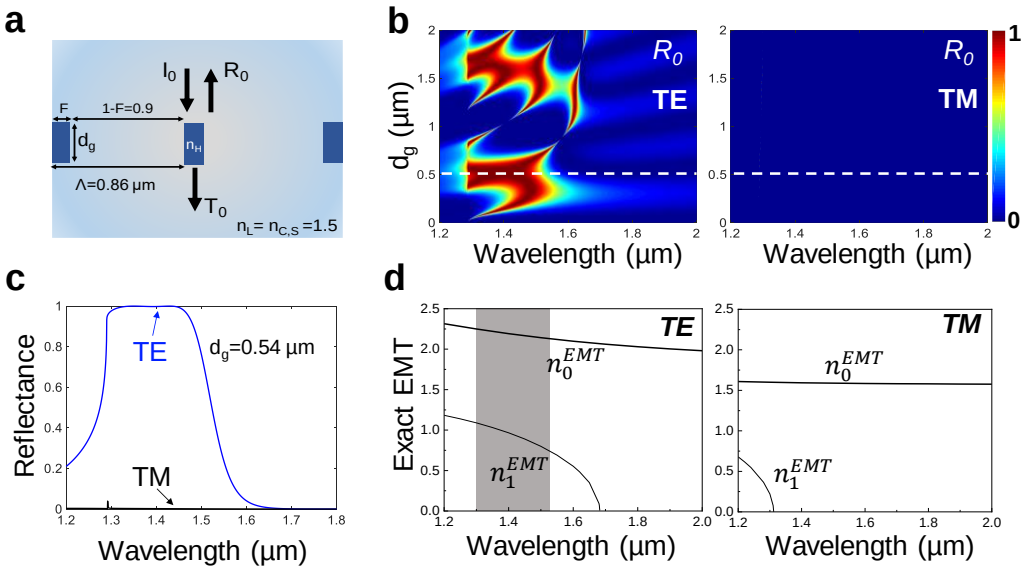

Figure 2-7 Rytov analysis of a sparse grating polarizer with parameters Λ= 0.86 μm, F=0.1, n_H=3.5, and n_L=1.5 extracted from Ref. [47]. (a) Schematic of the design with finite grating thickness of d_g, (b) RCWA-based λ-d_g reflection map for TE and TM polarization states, (c) reflectance spectra with d_g=0.54 μm, and (d) exact Rytov effective refractive index diagram for TE and TM cases.

2.4 Conclusion

In summary, we present Rytov refractive indices obtained by solving the exact Rytov formulation initially derived in 1956. In contradiction to past work where effective medium theory returns a single effective index for a given device, the full formalism provides multiple solutions based on the multiple roots inherent therein. We interpret these solutions as pertaining directly to evanescent waves that drive the laterally-propagating Bloch modes foundational to lattice resonance. The

resonant reradiated Bloch modes experience wavelength-dependent refractive indices that are solutions of Rytov's closed-form expressions. Moreover, the full set of Rytov indices is directly applicable to design of periodic photonic devices, including metamaterials and metasurfaces. Their manifestation fully supports the diffractive-optics explanation of resonance device physics in terms of lateral leaky Bloch modes and guided-mode resonance. The cutoff wavelengths of the evanescent diffraction orders define their spectral region of dominance and interaction. The spectral slope of the Rytov indices predicts spectral ranges across which the reradiated Bloch modes will be in phase or out of phase. Thus, for example, it is possible to predict whether to expect a wideband reflector behavior from a one-dimensional grating structure simply by calculating effective refractive index graphs without performing any rigorous numerical simulations. The closed-form Rytov formulas might thus substantiate efficient design methods. The fact that the cutoff wavelengths are directly embedded in the formulation enables definition of the dividing line between the resonance subwavelength region and the deep-subwavelength region based on the cutoff wavelength of the first evanescent diffraction order. This important transition point is always numerically available via the Rytov formulation. In a special case, we find that the transition wavelength is given by $\lambda_c^1 = 2Fn_H\Lambda$ which is directly comparable to the universal Rayleigh wavelength $\lambda_R = n_S\Lambda$ that defines transition from the non-subwavelength to the subwavelength regime. We successfully apply the Rytov formalism to reliably

describe the behavior of various optical devices, such as wideband reflectors, resonant bandpass filters, and guided-mode resonance polarizers. Rigorous numerical results support all of our explanations and predictions. Future studies might investigate and extend the methods of this study to more complex lattices such as those with multipart unit cells. Additionally, since the fundamental properties of the elemental 1D lattices studied here transfer in large measure to corresponding 2D lattices, extension of this work to 2D periodic metasurfaces is of interest. The utility and precision with which the simple Rytov formalism applies to resonant photonic lattices including metamaterials is an important discovery that will come as a surprise to most and will count as a major advance in the development of the field.

Therefore, the key advances we made in this study include:

1. Solving the exact Rytov formula returns one, multiple (can be infinite) effective refractive index values n_m^{EMT} $(m = \pm 1, \pm 2, \dots)$, depending on the working wavelength, in strong contradiction with previous studies returning one refractive index values per wavelength based on the approximated formalism.

2. The number of these values directly and accurately determines the number of diffracted orders at work, hence determines whether we are in deep suwavelength or resonance subwavelength region. Based on this, we define a clear transition wavelength between the resonance subwavelength region and deep subwavelength

region using the cutoff wavelength of the first diffracted order n_1^{EMT}. This transition point was not clearly defined previously in the literature.

3. For specific grating structures simple analytical formula exactly predict the cutoff for each order. For this structure, we find that the transition wavelength is given by $\lambda_c^1 = 2\Lambda F n_H$ (Λ: period, F: filling factor of the period constituent with refractive index of n_H) which is directly comparable to the Rayleigh wavelength $\lambda_R = n_S\Lambda$ (n_S: refractive index of the substrate) that defines transition from the non-subwavelength to the subwavelength regime. Furthermore, in the subwavelength regime, to ensure that at least one resonance arises from the m^{th} diffraction order, the Rayleigh wavelength should be smaller than the cutoff wavelength (i.e., $\lambda_R < \lambda_c^m$). This yields a constraint $F > n_s/2n_H$ for m=1.

4. The cutoff wavelengths define the spectral location where a new evanescent diffraction order, with attendant lateral Bloch-mode excitation, enters and begins to participate in the resonance dynamics.

5. Surprisingly, we demonstrate that this equation can apply to the practical resonant photonic lattices possessing finite thickness.

6. We stablish new, simple yet precise insights to comprehensively explain the underlying physics of the mathematically simulated results.

7. Not only the cutoff values but also the shape of the n_m^{EMT} curves will determine the optical response of the periodic metasurfacs.

8. We show that the first evanescent order cutoff wavelength (λ_c^1) and Rayleigh wavelength (λ_R) should follow specific condition to ensure that at least one resonance arises from the m^{th} diffraction order.

9. With our model, we can predict the spectral response of the one-dimensional periodic structures. Our predictions completely match with RCWA-based simulation results.

10. We successfully apply the Rytov formalism to reliably describe the behavior of various optical devices, such as wideband reflectors, resonant bandpass filters, and guided-mode resonance polarizers.

Chapter 3

Metamaterial polarizer providing principally unlimited extinction

Polarizers are used in a host of common products. In display technology, TV and computer monitors contain two polarizing layers, one on each side of the liquid-crystal display sheet that generates the image. Moreover, they are used in a wide variety of imaging applications, in telecommunication systems, and in laser technology. Linear polarizers pass one particular polarization state while blocking all other states. Conventionally, the polarization state is defined by the spatial direction of the electric-field component of the wave relative to the plane of incidence. The efficiency of a linear polarizer operating in transmission is ascribed to the extinction ratio which is defined by the transmittance of the desired polarization divided by the transmittance of the unwanted polarization state. Thus, the extinction ratio of the ideal linear polarizer approaches infinity.

Conventional polarizers based on natural crystals and multilayer thin films are commonplace. Dichroic polarizing crystals absorb light with electric field along a defined crystal axis permitting another state to survive. Sheet polarizers and metal nanocomposite-particle polarizers operate similarly [48,49]. Classic multilayer films are used in polarizing beam splitters at oblique incidence because homogeneous films, multilayer or not, cannot polarize light at normal incidence [50]. Wire-grid polarizers (WGPs) are made with parallel grids of wires that have nanoscale spatial features for visible light wavelengths as the period of the wires is

300 nm or less. The WGPs operate in transmission and work by absorbing and reflecting the polarization state with the electric-field vector along the wires while transmitting the component with electric-field vector orthogonal to the wires [51,52]. Advantages of devices not based on metals, such as those presented here, include low loss, high efficiency, easy handling, and ability to work as good polarizers in reflection, transmission, or both.

In the context of the present work, dielectric metasurfaces employing compact subwavelength structures or form-birefringent gratings have been used to fashion polarizers in the past. Tyan et al. experimentally realized an extinction ratio of ~830 at wavelength λ=1.523 μm based on a multilayer subwavelength binary grating design [53]. Delbeke et al. fabricated a grating-based polarizing beam splitter in monolithic GaAs with an experimental extinction ratio of ~72 at λ=10.6 μm [54]. Engaging the guided-mode resonance effect, Lee et al. fabricated a polarizer operating in the telecommunication band with a bandwidth of 40 nm and extinction ratio of ~97 [55]. Attempting to improve device performance, Lee et al. reported resonant polarizers made of nearly lossless materials including TiO_2, Si_3N_4, and Si [56]. Recently, wideband polarizers based on sparse low loss dielectric resonant photonic lattices were reported. Employing high aspect ratio nanogrids and matched refractive index of cover and substrate, a bandwidth of ~190 nm with extinction ratio less than 100 was found [47].

Moreover, there is immense current interest in the nanophotonic properties of dielectric metasurfaces with subwavelength spatial dimensions. Numerous publications address wavefront control and polarization analysis using metasurfaces to realize functionality comparable with bulky traditional elements [57-59]. Control of phase and polarization was sought using effective metasurfaces fashioned with elliptical nanoposts [60]. Full-Stokes imaging polarimetry was achieved via dielectric metasurfaces [61]. Finally, broadband linear polarization conversion using dielectric antennae was reported by Yang et al. [62].

Here, we report the design, fabrication, and characterization of metasurface polarizers based on the guided-mode resonance effect achieving excellent results. We design an elemental polarizer containing a single-layer grating on a substrate with air cover. This building block polarizer has a low aspect ratio and is thus expeditiously fabricated. Then, we demonstrate both theoretically and experimentally that stacking our individual metasurface polarizers results in a polarizer device with high extinction ratio, broadband operation, wide angular tolerance, and compact size. The physical mechanism operative in these devices is totally different from any other polarizing concept in current use. Our polarizer provides 100% transmission in TM or p-polarization and 100% reflection in TE or s-polarization. Thus we demonstrate nearly zero-insertion-loss polarizers that function simultaneously in transmission and reflection at normal incidence, an attribute not possessed by present polarizer technologies. Common polarizers

currently in use have some degree of insertion loss with transmission of useful polarized light ranging from ~50% to ~95%. Whereas each fundamental resonance polarizer layer possesses considerable polarizing capability, by vertically stacking the layers, we can attain arbitrarily high extinction ratios across substantially wide spectral bands while maintaining low insertion loss and compact size.

3.1 Elemental polarizer design

First, we develop basic individual polarizers possessing a single-layer grating to operate in the near-IR band on commercially available silicon-on-quartz (SOQ) wafers (Shin-Etsu Chemical Co., Ltd). The SOQ platform used in our experiment contains a 220-nm-thick crystalline silicon film (c-Si) on a quartz substrate. **Figure 3-1(a)** illustrates the schematic and design parameters of the elemental polarizer. The refractive index of Si and quartz are 3.45 and 1.45 as there is a minimal dispersion in these materials in the desired wavelength range of ~1400-1700 nm.

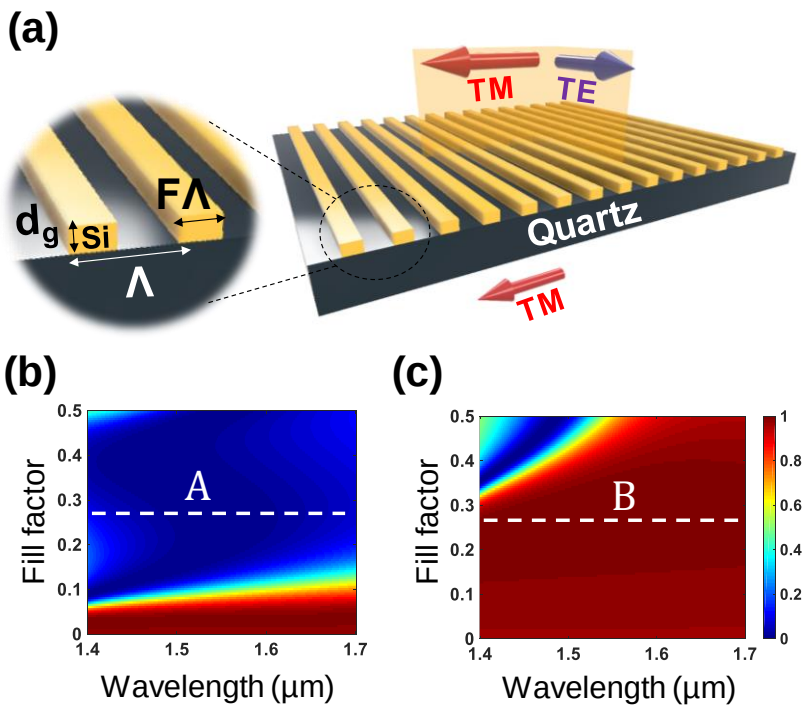

Figure 3-1 Elemental metasurface polarizer. (a) Schematic of the individual metasurface polarizer, made with a Si grating on a quartz substrate, indicating high transmission for TM polarization while suppressing the transmission of the TE polarization state. The physical parameters of the subwavelength grating model are period (Λ), grating depth (d_g), and fill factor (F). Transmission map of a subwavelength Si grating as a function of fill factor F for (b) TE and (c) TM polarization states where Λ=0.95 μm and d_g=0.22 μm and where F=0.28 is marked with dashed lines.

Figures 3-1(b) and **3-1(c)** display zero-order transmission (T_0) maps of the individual polarizer as a function of fill factor (F) pertinent to the TE and TM polarizations, respectively. The TM polarization state has an electric field perpendicular to the grating grooves as noted in **Figure 3-1**. Based on the color scale bar, dark red areas show high transmission whereas dark blue regions

represent low transmission. The white dashed line shows the fill factor at which a wideband polarizer can be achieved based on the highest transmission difference for TE and TM polarization states. Moreover, it is shown that physical dimensions of period Λ=0.95 μm, grating depth d_g=0.22 μm, and grating fill factor F=0.28 result in high and low transmission responses under TM and TE polarization, respectively, in the 1450-1650 nm wavelength range.

3.2 Multilayer polarizer design

To improve the extinction ratio (ER= T_{TM}/T_{TE}) of the polarizer while maintaining low loss and high transmittance, cascading two or multiple individual polarizers is proposed. The lossless nature of the materials in use in each individual polarizer allows us to stack them to improve the polarizer performance. The inset in **Figure 3-2(a)** shows the cascaded device architecture composed of two individual polarizers with F=0.28 separated by an air gap with thickness d_{gap}. Transmission maps of the dual-metasurface structure while changing the air gap thickness are shown in **Figures 3-2(a)** and **3-2(b)** for TE and TM polarization states, respectively. Transmission spectra corresponding to white dashed lines (A', B') for air gap thickness of d_{gap}=1.5 μm are shown in **Figure 3-2(c)**. Moreover, **Figure 3-2(e)** depicts the higher extinction ratio and wider bandwidth for the dual-metasurface polarizer compared to the elemental metasurface design. These individual metasurfaces are not coupled in the cascaded design as the separation

distance exceeds a micrometer. Therefore, there is a negligible effect in device performance associated with any lateral displacement of the top and bottom gratings. Note that the top and bottom polarizers have identical physical parameters.

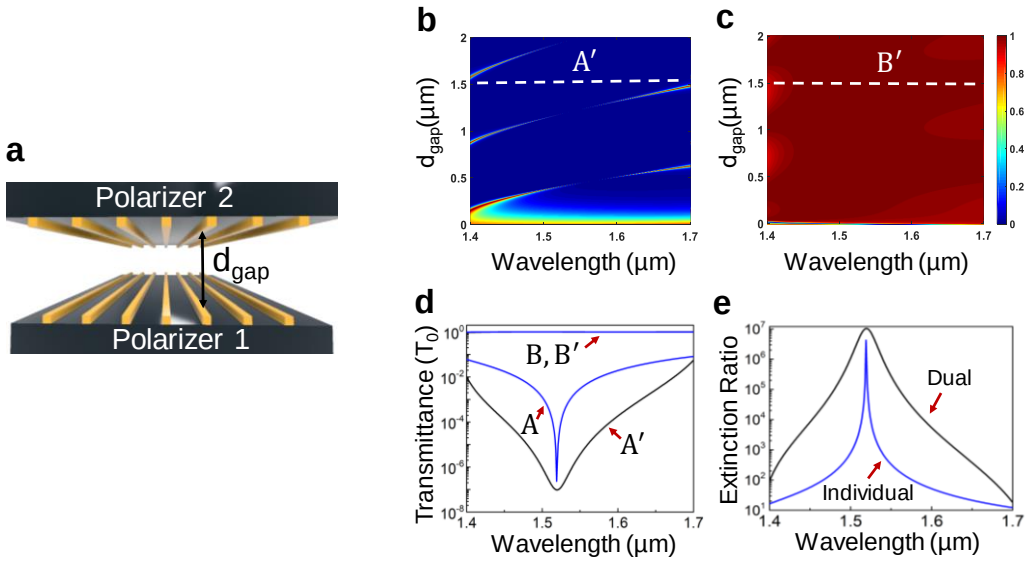

Figure 3-2 Dual cascaded metasurface polarizer module. (a) Schematic of a double-cascaded polarizer module separated by an air gap with thickness of d_{gap}. The calculated transmission spectra for (b) TE and (c) TM polarization states. (d) Transmission spectra pertinent to white dashed lines illustrated in the transmission map of the individual device (A, B) and stacked device (A', B'). (e) Calculated extinction ratio of the elemental and the dual-cascaded module.

In addition, because our polarizers are nanopatterned and periodic, they work perfectly at normal incidence—an extremely common and important case for optical systems. In comparison, multilayer thin-film stacks, which constitute perhaps the most important current commercial polarizer type, do not work at

normal incidence on account of the fundamental physics of homogeneous thin films. The stacked nanograting polarizers provide a good angular tolerance with sustained extinction ratios under angular deviation of incident plane waves and for non-collimated illumination.

3.3 Experimental results

To fabricate the polarizers, the SOQ substrates measuring 25x25 mm^2 are coated with SEPR-701 positive photoresist, followed by a one-minute soft bake process at 110°C. Applying laser interference lithography (LIL), we expose a 3x3 array of 5x5 mm^2 devices and develop the photoresist film to create a 1D resist mask on the c-Si film. The mask patterns transfer to the c-Si film via a reactive-ion-etch (RIE) process. Etching time is optimized based on the etch rate of c-Si. Subsequently, residual photoresist is removed by O_2 ashing. Scanning electron microscopy (SEM) and atomic force microscopy (AFM) measurements are used to verify the final device dimensions. The SEM images shown in **Figure 3-3(a)** confirm that uniform high-quality Si gratings are fabricated via LIL which translates to low scattering loss due to the fabrication process.

To measure the transmission spectra of the fabricated devices and investigate their actual performance, we employ a supercontinuum light source to produce an incident beam and near-IR optical spectrum analyzer (OSA) to detect the transmitted light. The polarized transmission measurements of the fabricated

samples (signal power) are made by inserting a Glan-Thompson polarizer (Thorlabs) with extinction ratio of 100,000:1 in the beam pathway. The reference transmission power is measured by removing the samples from the beam pathway and collecting the output power from the Glan-Thompson polarizer for each polarization state. Finally, the normalized transmission spectra for fabricated samples pertinent to both TE and TM incident waves are calculated by dividing the signal power by the reference power measured via the detector. An excellent quantitative agreement is illustrated in **Figure 3-3(b)** between the simulated and experimental results for the fabricated polarizers. **Figure 3-3(c)** shows the extinction ratio of the fabricated individual polarizer.

To prepare the proposed dual-metasurface polarizer module, the separation distance of the gratings, d_{gap}, must be controlled. This control is achieved by spin coating a layer of photoresist (s-1813) on the patterned SOQ wafer and exposing the device area through a mask. This process results in a 1.5 μm thick PR frame surrounding the 3x3 device array. The side-view SEM image in **Figure 3-3(d)** confirms that the elemental polarizing films are separated by d_{gap}~1.5 μm in the module. Zero-order spectra for TE and TM polarized transmission for the cascaded device are shown in **Figure 3-3(e)** whereas **Figure 3-3(f)** shows the measured extinction ratio of the module. It is clearly observable that the extinction ratio of the dual-cascaded module is an order of magnitude larger than that of the elemental polarizer. A key practical advantage of the face-to-face arrangement in the dual-

grating module is that the grating layers are completely isolated from the surrounded environment. This situation ameliorates cleaning and handling concerns pertinent to many types of conventional polarizers when exposed to different environments.

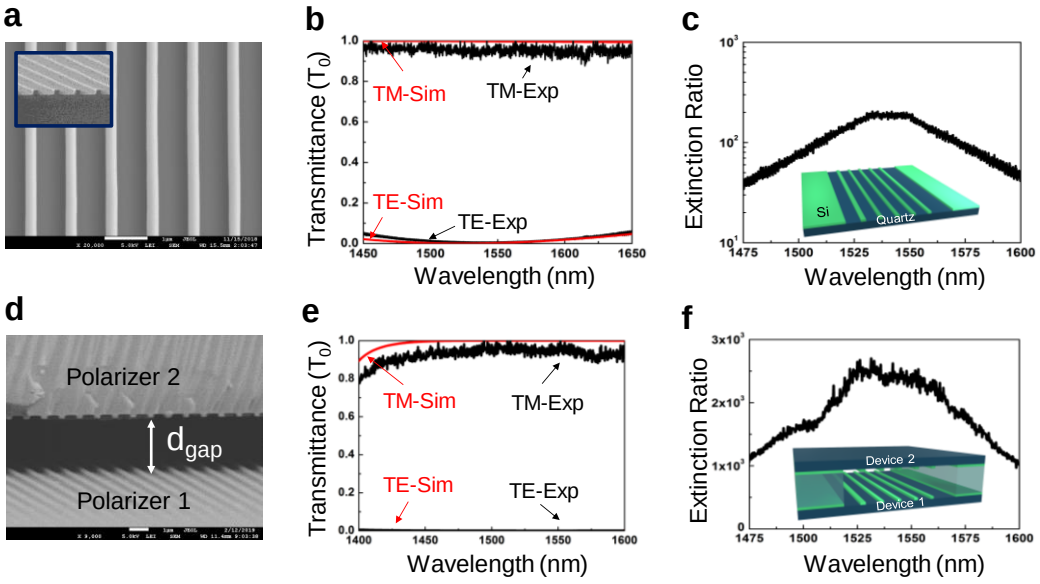

Figure 3-3 Fabricated elemental and dual-cascaded polarizers. (a) SEM image of the fabricated elemental polarizer. (b) The simulated and experimental transmission spectra for TE and TM polarization states of the single device. (c) Measured extinction ratio of the elemental polarizer. (d) Side view SEM image of the fabricated polarizer module with controlled separation distance. (e) TE and TM polarized transmittance of the cascaded polarizer. (f) Measured extinction ratio of the dual-grating module.

To further improve polarizing efficiency, we stack two identical dual-grating modules and measure the resulting transmission spectra. A schematic of this design appears in **Figure 3-4(a)**. **Figure 3-4(b)** shows attendant simulated

extinction ratio. We achieve an extremely high extinction ratio ER> 10^8 in the ~1.45 to 1.6 μm spectral domain across a ~150-nm-wide band. An image of the fabricated polarizer is provided in the inset of **Figure 3-4(b)**; total device thickness is only 2 mm. The zero-order measured transmission spectra of the dual-module under TE and TM polarized incident light are shown in **Figure 3-4(c)**. We see that the normalized transmission of the TE polarization state is suppressed to values less than 10^{-5} while the TM transmission is high due to the lossless nature of our polarizer. The extinction ratio of this device reaches ~100,000 which is the highest experimental value for metasurface polarizers reported to date. It is worth noting that Glan-Thompson polarizers are made of calcite which is sensitive to temperature and prone to thermal shock; in contrast, our devices can tolerate high temperatures and thermal variations. Measured data in **Figure 3-4(d)** shows very high value of ER for the dual module polarizer device.

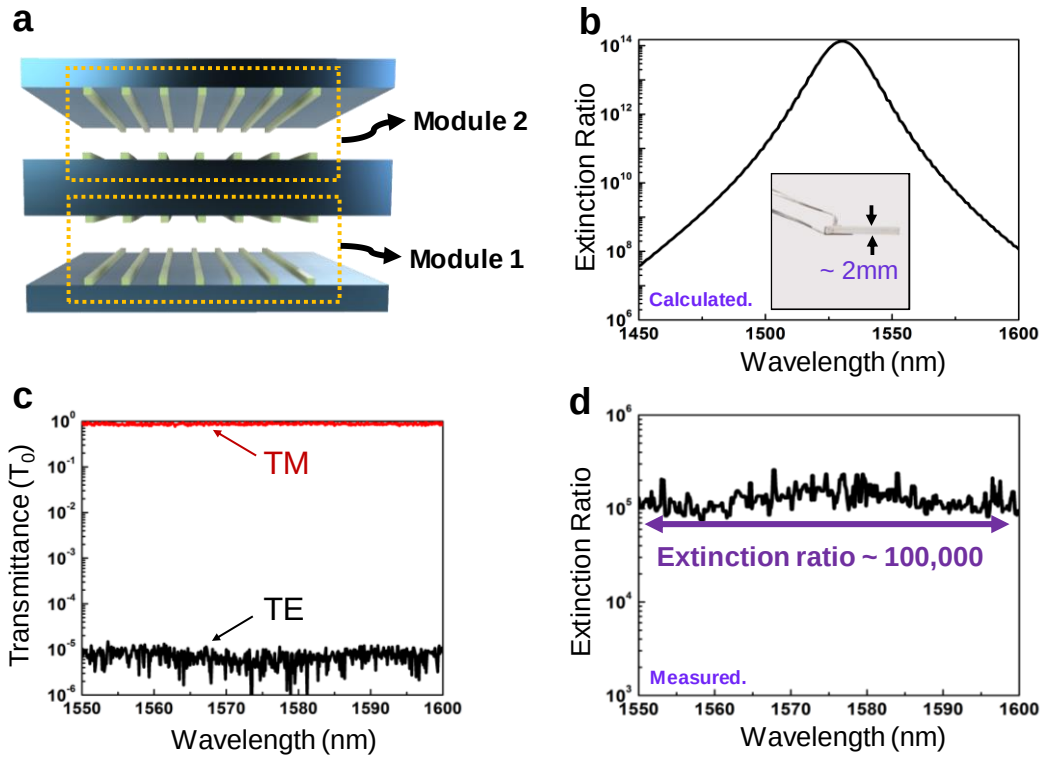

Figure 3-4 Dual-module polarizer. (a) Schematic layout. (b) Calculated extinction ratio. The inset shows a photograph of our polarizer. (c) Logarithmic scale zero-order transmission spectra for TE and TM polarization states. (d) Extinction ratio of the fabricated polarizer.

Measuring very low and very high transmittance accurately is a challenge. Thus, we verify the results by a Muller matrix formulation developed to determine high unknown extinction ratios using a known polarizer with a verified extinction ratio. The extinction ratio of our device can be calculated by [63]

$$ER_2 = \frac{r_{12} ER_1 - 1}{ER_1 - r_{12}} \tag{3.1}$$

where ER_1 and ER_2 are the known and unknown extinction ratio values in a system containing a pair of polarizers while unpolarized light is incident on the system. The pair contrast ratio (r_{12}) is the transmission intensity ratio between parallel and crossed alignment of the polarizers obtained with a power meter. **Figure 3-5(a)** shows a schematic of our measurement setup containing the Glan-Thompson polarizer with a known extinction ratio (ER_1~100,000) as specified by the manufacturer and the dual-module polarizer with an unknown extinction ratio (ER_2). According to the setup, un-polarized light is incident on both polarizers and the unknown extinction ratio ER_2 can be determined using Eq. (3.1). **Figure 3-5(b)** confirms a good agreement between the ER found by Eq. (3.1) and the ER in **Figure 3-4(d)**.

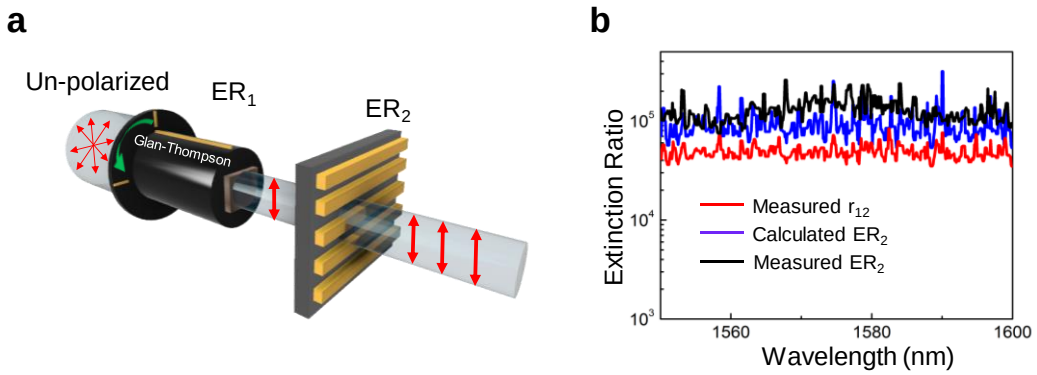

Figure 3-5 High extinction ratio measurement setup. (a) Schematic of the setup containing a pair of polarizers with extinction ratios of ER_1 and ER_2. The parallel and crossed alignment of these polarizers is realized by rotating the Glan-Thompson polarizer. (b) Measured pair contrast ratio as in Fig. 4(d) (black line) and calculated pair contrast ratio based on Eq. (3.1) (blue line).

3.4 Conclusion

We provide cascaded multi-metasurface architectures to linearly polarize an incoming electromagnetic wave to achieve an ultra-high extinction ratio not seen in individual metasurfaces. The backbone of the multi-module polarizer is an individual polarizer made of a 220-nm-thick subwavelength periodic Si grating on a quartz substrate. The numerical and experimental results show that our device is invisible to the TM polarization state while reflecting the TE polarized light efficiently. Moreover, we show experimentally that cascading four metasurfaces in a dual-module structure results in a record extinction ratio of ~100,000 in a sparse 2-mm-thick device. Extinction ratios at this level are obtainable in bulky, expensive, and sensitive commercially available polarizers. On account of the lossless nature of the materials used to fashion each elemental polarizer, we achieve a compact, robust module with a comparable extinction ratio. Further development of the basic concepts explored may lead to a new class of practical polarizers with performance exceeding that shown here.

Chapter 4

Optical devices based on nanoimprinted nanocomposites

Organic-inorganic nanocomposites exhibit new properties not available in their separate constituents. Novel and useful properties of nanocomposites originate from the combination of the advantages of their constituent organic and inorganic materials [64]. There are two main types of nanocomposite preparation techniques: The in-situ method which contains synthesis and growth of nanoparticles inside an organic material and the ex-situ method that involves uniform dispersion of the premade nanoparticles in the polymer matrix [65,66]. Numerous studies have been conducted to tune the refractive index of organic materials by incorporating high refractive index inorganic materials such as ZnS [67,68], ZrO_2 [69], TiO_2 [70,71], and PbS [72,73]. Critical issues associated with nanoparticles are particle size and dispersion quality in the host polymer. Rayleigh scattering and attendant intensity loss of transmitted light from the nanocomposite is managed by choosing the size of the embedded particles to be, for example, below one-tenth of the incident wavelength. Moreover, scattering associated with agglomeration of the nanoparticles takes place especially when the refractive index of nanoparticles is high compared with the host polymer. In addition, as the particle size decreases, the specific surface area, the surface energy, and the mobility of the nanoparticles due to Brownian diffusion increases, which translates to incessant collisions between the particles with proclivity to agglomeration [74, 75]. By using an appropriate

dispersion process in the ex-situ method, the agglomeration can be minimized by reducing attractive forces between the nanoparticles. The more reliable method to enhance dispersibility and reduce agglomeration is to keep the nanoparticles separated from each other by attaching organic chains to the surface of the nanoparticles which act as spacers [76]. Through the nanocomposite process, mechanical and optical properties of organic materials can be improved and manipulated.

Whereas the emphasis here is on fabrication methodology, we provide examples of prototype guided-mode resonance filters. The guided-mode resonance effect occurs in thin-film structures containing 1D or 2D periodic layers enabling applications for instance in lasers [77], biosensors [78,79], and spectral filters [6,80]. In general, attendant modal resonances stimulate rapid changes in the distribution and localization of electromagnetic nearfields as well as in reflected or transmitted light beams. To obtain leaky mode resonances, an appropriate refractive index contrast modulation is required. Therefore, it is necessary to tune the refractive index of polymer. The geometric characteristics of resonance devices such as refractive index (n), grating thickness (d_g), homogenous layer thickness (d_h), grating period (Λ), and fill factor (F) affect the final spectral response. Resonance conditions prevail as an incident light wave couples to leaky, or quasi-guided, lateral Bloch modes supported by the periodic device.

In NIL, patterns on PDMS stamp can be transferred to imprint materials [81]. The resulting structure, which has dimensions defined by the original master, acts as the final device [82-84]. Among critical issues in the NIL process is simultaneous control of the uniformity and thickness of the imprint material which in some applications including resonant optical devices play a vital role [85,86]. A common solution involves applying pressure on the stamp which may not be sufficiently precise for demanding applications. In addition, applying a uniform pressure to all parts of the soft and flexible stamp and imprint material needs accurate control of the applied pressure and special nanoimprint equipment [87-89]. Another solution is placing the imprint stamp in contact with a spin coated layer of a low viscosity polymer follow with the curing process [90]. Here, we use a convenient method to control the uniformity and thickness of imprint material without applying pressure by fabricating a channel. In this work, as an example application, we present simulated and fabricated optical devices made of UV curable NOA73 blended with Si nanoparticles based on the NIL method.

4.1 Experimental methods

Commercially available polycrystalline laser-synthesized Si nanoparticles with diameter < 80 nm and an optical adhesive NOA73 are the nanocomposite constituents applied here. The host polymer with refractive index of 1.56 with low viscosity (130 cps) acts as a matrix for the nanocomposite. The ex-situ method is

used to produce the nanocomposite as a resist or imprint material. For ex-situ preparation of the nanocomposite, the Si nanoparticles were homogeneously dispersed in NOA73 at room temperature via a sonication probe for 30 seconds at 40 watts. The dynamic light scattering (DLS) technique was used to measure the particle size distribution of the nanoparticles existing in the polymer matrix. The refractive index of the nanocomposite corresponds to the volume percentage of the incorporated particles in the matrix material. To predict the refractive index (n) of final the nanocomposites the rule of mixture is used as:

$$n_{nanocomposite} = n_{filler}V_{filler} + n_{matrix}V_{matrix} \tag{4.1}$$

which is proportional to the volume fractions V_i and refractive indices n_i of the filler (Si) and matrix material (NOA73). Here we select Si as a filler because it has high refractive index with n~3.45 in the spectral band of interest and low density (ρ = 2.33 g/cm^3) comparable with other high refractive index materials. Polyvinylpyrolidone (PVP; molecular weight ~55000) is used to functionalize the surface of the Si nanoparticles. To obtain functionalized surfaces, the PVP was attached to the particle surface by addition of 150 mg of Si nanoparticles and 150 mg of PVP to 15 mL of deionized water and then sonicated in a water bath. The mixture was centrifuged to remove the unbound excess of PVP followed by washing and redispersion. Then, unadsorbed PVP was removed by repeated centrifugation/wash/redispersion cycles [91]. Attenuated total reflectance FTIR

(ATR-FTIR) spectroscopy enables confirmation of the attachment of the PVP to the surface of the nanoparticles.

In our study, PDMS was used to make the stamp that contains a negative pattern of the patterned silicon wafer (master template). The NIL process used to fabricate the guided-mode resonance (GMR) device structures is summarized in **Figure 4-1**.

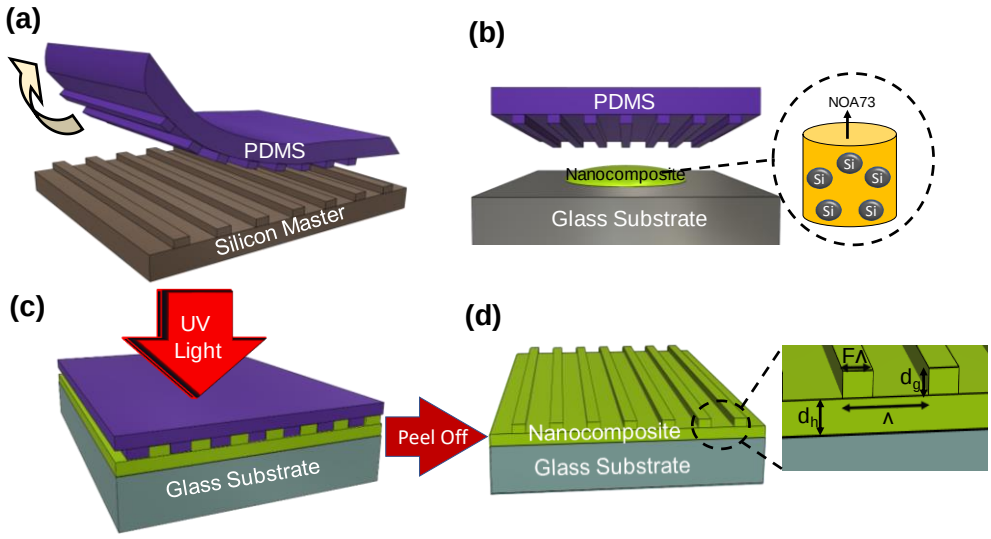

Figure 4-1 Nanoimprint device fabrication method. (a) PDMS stamp peeled off from the silicon master. (b) Nanocomposite poured on a glass substrate. (c) UV curing of the nanocomposite through the PDMS stamp. (d) A final nanoimprinted device with specific physical parameters.

To implement rapid curing of the nanocomposite, we used a high-power UV-cure system with lamp power of 600 watts and irradiance of 175 mW/cm^2. Different concentrations of Si nanoparticles were incorporated into the NOA73 matrix with n=1.56 to tune the refractive index of NOA73 to 1.9, 2, and 2.1 with

filler volume percentage of 18%, 23%, and 28%, respectively. These nanocomposites were employed to fabricate nanoimprinted GMR devices with similar geometric characteristics but different refractive indices. Spectral measurements were carried out with a super continuum light source and a near-IR optical spectrum analyzer (OSA).

4.2 Results and discussion

After mixing the nanoparticles via the sonication probe, dynamic light scattering (DLS) measurements for low filler concentration nanocomposites were carried out to determine the particle size distribution. The DLS results in **Figure 4-2** show an appropriate dispersion quality immediately after the sonication process and verify the particles size is in the range of the specified nanoparticles. This confirms proper dispersion conditions and uniform distribution. Another measurement after 15 minutes demonstrates formation of agglomeration during this interval of time such that now ~95% of mixture particles have diameters up to 800 nm. On the other hand, the DLS curve for the PVP-coated silicon nanoparticles shows a low level of agglomeration after 15 minutes demonstrating the effectiveness of the surface treatment to reduce agglomeration.

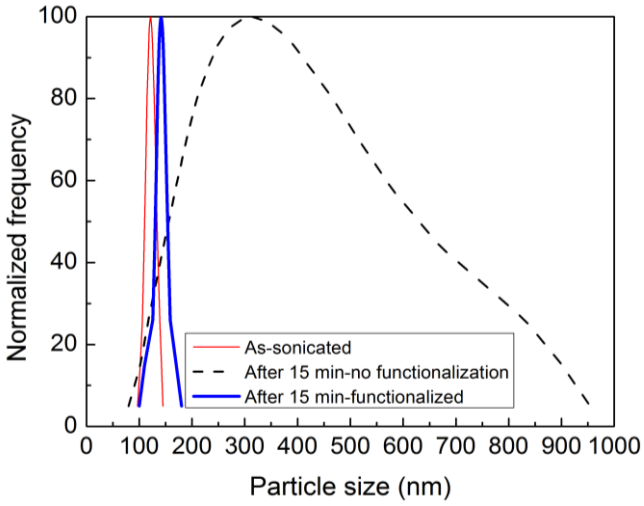

Figure 4-2 DLS measurements of as-sonicated, non-treated, and PVP-treated silicon nanoparticles after 15 minutes.

Moreover, ATR-FTIR measurements were done to confirm the attachment of the PVP polymer to the surface of the silicon nanoparticles. **Figure 4-3** depicts the ATR-FTIR spectra related to the pure PVP, the as-received silicon nanoparticles and the PVP-coated silicon nanoparticles. The absorbance peaks at 1660 cm^{-1}, 1425 cm^{-1}, and 1290 cm^{-1} are related to the characteristic peaks of C=O groups, scissoring bending of CH_2 groups, and C-N stretching vibrations of PVP, respectively [92]. These characteristic PVP dips are clearly shown in the transmitted spectrum of the functionalized nanoparticles which indicates existence and formation of the PVP-coated silicon nanoparticles. In contrast, none of these characteristic peaks were detected in as-received nanoparticle spectra.

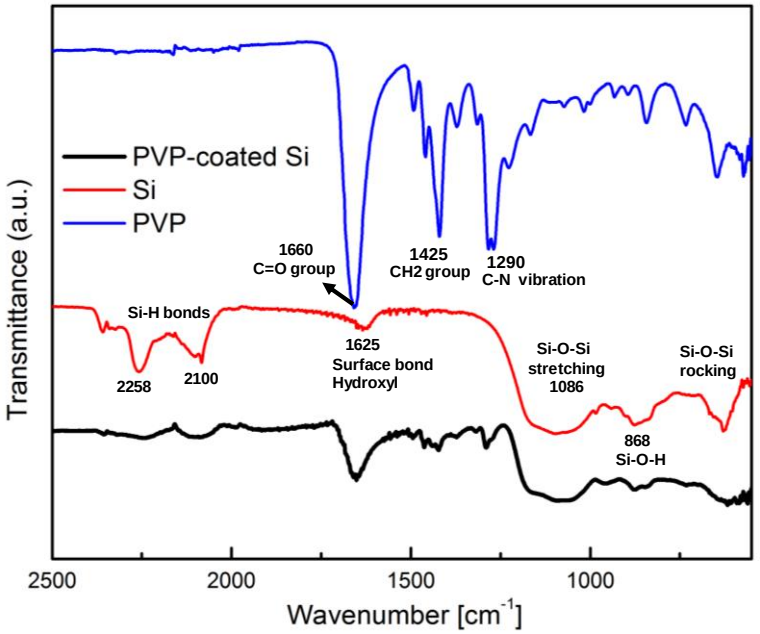

Figure 4-3 ATR-FTIR measurements for pure-PVP, as-received silicon, and PVP-coated silicon nanoparticles.

The SEM images in **Figures 4-4(a)-(c)** demonstrate the importance of the surface modification of the nanoparticles to minimize the formation of agglomeration. Although the surface treatment of the nanoparticles can prevent agglomeration, for highly loaded nanocomposites in which the particles are densely packed, there is a tendency for them to agglomerate during extended curing times. Therefore, in addition to the surface treatment of the silicon nanoparticles to enhance dispersion quality, rapid curing of the nanocomposite will have a beneficial influence to minimize agglomeration. The SEM images illustrate that for the silicon concentration of ~23 vol% combination of rapid curing and surface treatment will give an appropriate particle distribution inside the NOA73 matrix which leads to lower agglomeration and scattering centers.

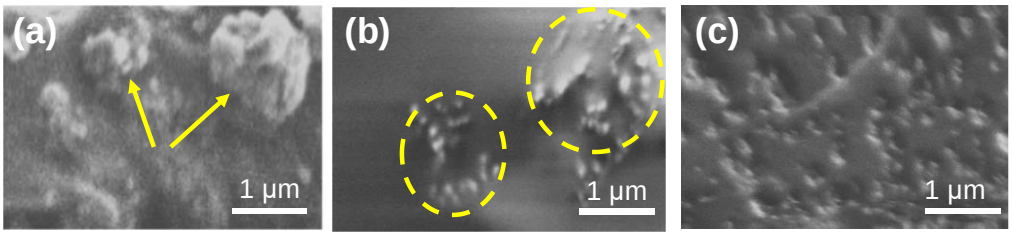

Figure 4-4 SEM images of nanocomposites with different Si concentrations. Distribution of nanoparticles in a nanocomposite containing ~23 vol% Si. (a) Non-treated nanoparticles under slow curing. (b) Non-treated nanoparticles under rapid curing. (c) Surface treated nanoparticles under rapid curing.

An AFM image of the silicon master after deposition of ~20 nm aluminum is show in **Figure 4-5(a)**. Moreover, the fabricated nanoimprinted device is shown in the AFM in **Figure 4-5(b)**. It is shown that the profile of the silicon master transfers well to the nanocomposite by means of the PDMS stamp. The quality of the grating lines shown in **Figure 4-5(b)** demonstrates that the peel-off process of PDMS from the cured nanocomposite is done with minimal imperfection.

Tang et al. mentioned applying an anti-stick monolayer coating to the PDMS before the stamping process to improve the quality of the peel-off process [93]. However, in this study we eliminate all such surface treatment processes. NOA73 is thiolene based and exhibits very poor adhesion to the PDMS [94]. Therefore, employing the thiloene based NOA73 will allow us to accomplish the peel-off process without using any anti-stick chemicals. The AFM images also show that there is no specific shrinkage of the fabricated nanoimprinted devices; thus, the dimensions of the silicon master can be reliably transferred to the final device. This is attributed to the low shrinkage (~1.5%) of NOA73 after curing as

compared to high shrinkage at ~20% associated with methods such as organic-inorganic hybrid sol-gel processing. Moreover, in this work we apply UV-curing which is fast and, unlike the sol-gel process, does not need high temperatures and long time to reach the high refractive index desired in some applications.

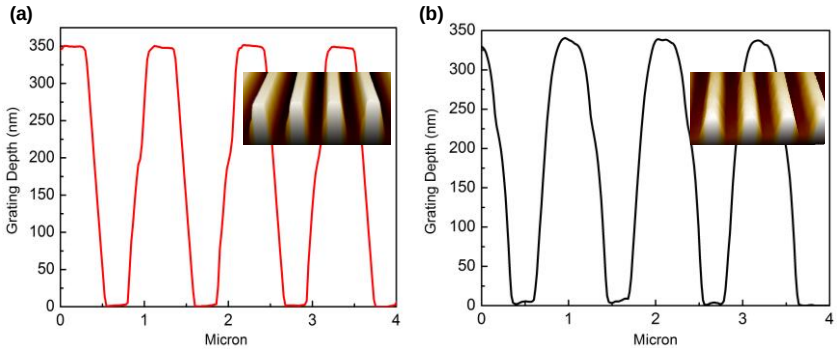

Figure 4-5 AFM images of the nanopatterned structures. (a) Silicon master after aluminum deposition. (b) Fabricated nanoimprinted optical filter device. Insets show 3D views of the grating lines.

Figure 4-6 shows SEM images of the grating ridges and a side view of a device containing 14 vol% Si. The SEM images of the grating lines match well with the AFM images and high-quality grating lines are seen. **Figure 4-6(b)** indicates the cross section of the imprinted device. We can see that the obtained homogeneous layer is thick and non-uniform, which is not acceptable for most resonance devices of current interest. One of the challenges of the nanoimprinting technique applied here is controlling the thickness of the homogeneous layer. Previous reports cite applying pressure to the stamp by simple weights [86] or by using complex imprinting equipment [87,88]. In either case, it is not easy to

accurately control the uniformity of the applied pressure to the whole flexible PDMS stamp.

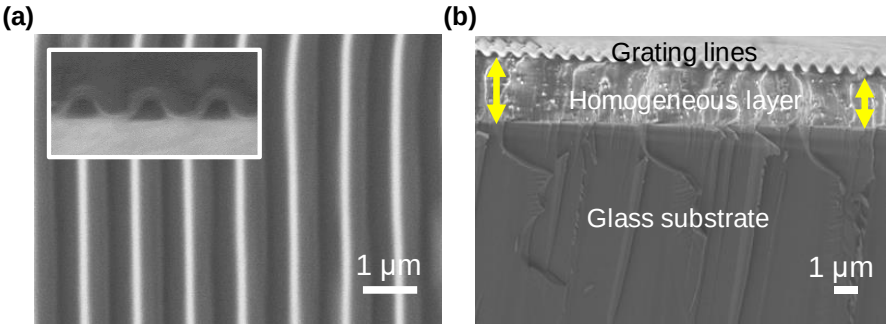

Figure 4-6 SEM images of nanoimprinted devices. (a) top-view of a nanoimprinted resonance device and (b) cross section of a resonance element with a thick and non-uniform homogeneous layer. The inset in (a) shows a cross-sectional view of the grating.

Good control of thickness and uniformity of the homogeneous layer in our example devices is essential for efficiency and functionality. To bring both parameters under simultaneous control, a convenient channel fabrication method is used. To implement this method, we first spin coated a layer of photoresist (Ultra-i 123) on a glass substrate. Then, by shining UV light through a rectangular mask and developing the photoresist, we realized a narrow channel (~5 mm wide). After that, the PDMS master was placed on the channel in a way that its grating lines were parallel to the long edges of the channel. The nanocomposite was poured at the edge of the PDMS which then diffused and filled the channel. The more nanoparticles concentration in the polymer host, the longer time to fill out the channel (1-3 min). Therefore, according to the spin speed, we can control the

photoresist thickness and consequently, the thickness of the homogeneous layer. The schematic steps of the channel fabrication are shown in **Figure 4-7(a)-(c)**. The cross section of the device with controlled homogeneous layer thickness is shown in **Figure 4-7(d)** which is evidence of successful implementation of the channel method.

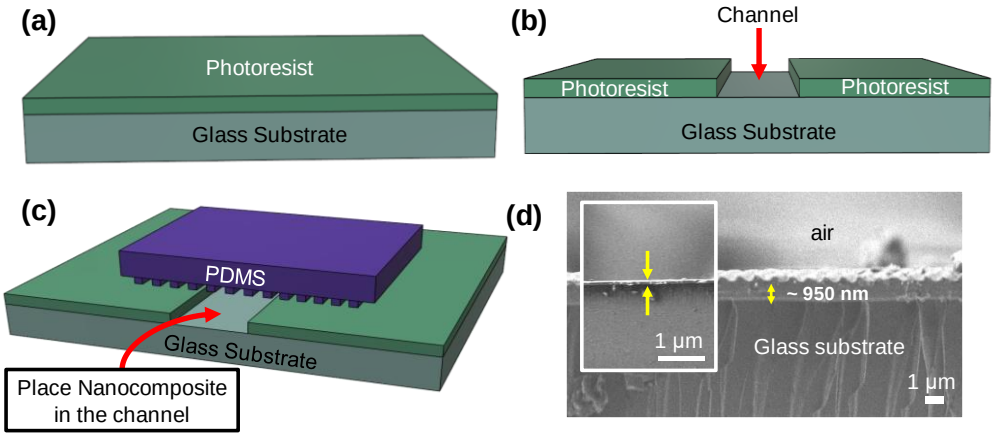

Figure 4-7 Method to control the thickness of the homogeneous layer. (a)-(c) Schematics of the channel fabrication. (d) Cross section of the device fabricated with the channel method to control the thickness of the homogeneous layer.

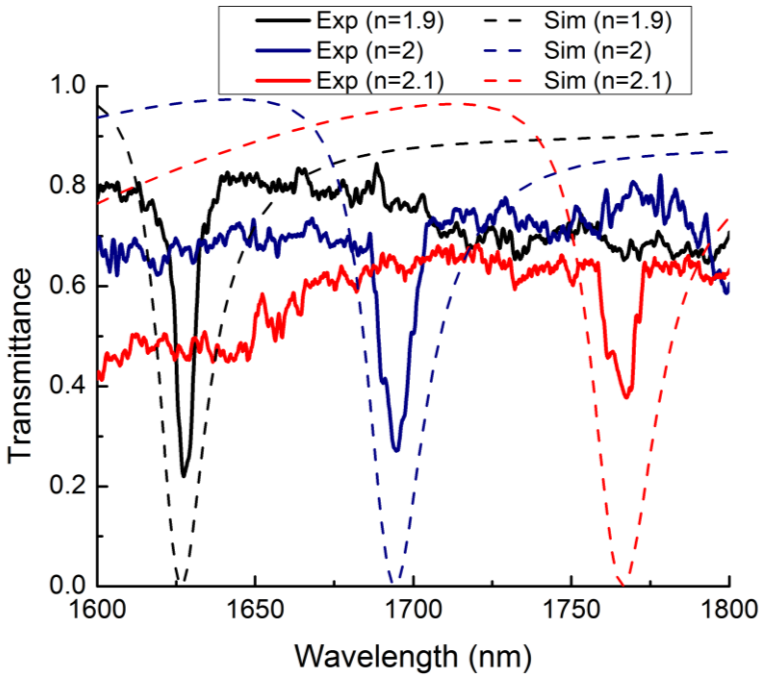

Figure 4-8 Experimental and calculated transmission spectra at normal incidence with TE-polarized light (electric vector of input light lies along the grating grooves). The fabricated devices have different refractive indices but the same physical parameters of Λ = 1.05 μm, d_g = 0.34 μm, d_h = 0.95 μm, and F = 0.45.

Spectral transmission measurements of devices with specific constant dimensions but different refractive indices, obtained by different filler concentrations, are shown in **Figure 4-8**. The input light from a super continuum light source is collimated and polarized with spot size of ~1mm. After the light hits the sample, the transmitted light will be collected by the optical fiber and will be sent to the OSA. The rigorous coupled-wave analysis (RCWA) is used to simulate the transmission spectrum of optical devices [95]. Good agreement is found between simulated and experimental results. However, the transmitted efficiencies of the experimental results are lower than the simulated efficiencies. It is seen that

the lowest nanoparticle concentration inside the polymer corresponds to the highest transmission efficiency. The reason is that the formation of agglomerations which act as scattering centers is more probable in higher concentrations. It is worth mentioning that without surface functionalization, even at low filler concentrations, the efficiency was less than 10% which confirms the importance of surface treatment to avoid agglomeration. Moreover, no transmission dip is observed for devices with n=2.0 and n=2.1 for non-coated nanoparticles even when using the fast curing process. Therefore, to ensure adequate efficiency, the nanoparticle surface treatment is essential.

It is clear that rapid curing of nanocomposite under high power UV lamp helps to prevent agglomeration at low filler concentrations. Through the rapid curing process, we can freeze and hold nanoparticles in the polymer matrix, so they will not have time to stick to each other and consequently settle down. However, for high concentrations of incorporated nanoparticles, the curing time will increase so it is more likely that the particles agglomerate. In summary, taking advantages of both rapid curing and optimal surface treatments enables tuning of the refractive index of the final device-quality polymer.

4.3 Conclusion

In this work, tunable refractive index was implemented by nanocomposites containing mixtures of a host polymer with refractive index of ~1.56 and Si nanoparticles with refractive index of ~3.45. With a ~28% Si fraction, an imprintable material with refractive index of ~2.1 was made. In principle, by controlling the filling fraction, the tunable range could be from ~1.6 to 2.1. Thereafter, we employed nanoimprint lithography using silicon masters and silicone (PDMS) molds to expeditiously fabricate example resonant optical filters. As the thickness of the homogeneous sublayer underneath the periodic layer is critical in this device class, we showed that we could control its thickness without pressure by employing a channel with precisely managed depth. Thus, by taking advantages of NIL and by controlling the refractive index and homogeneous layer thickness of the imprint material, we demonstrated resonant filters possessing the design parameters in composites with refractive indices of 1.9, 2.0 and 2.1. Here, we avoided use of anti-stick media on the PDMS surface by choosing an appropriate organic material (NOA73) which does not stick to the PDMS stamp. We found negligible shrinkage of the nanocomposite imprint material deriving from low shrinkage (1.5%) of the host medium. This enables fabrication of precise resonance devices which maintain the master's dimensions. Additionally, by combining the advantages of surface treatment of the nanoparticles and rapid curing

we minimized particle agglomeration and consequently fabricated useable resonant filters with acceptable response as measured in the 1600-1800 nm spectral band.

Chapter 5

Rapid large-scale fabrication of multipart unit cell metasurfaces

Diffractive elements, recently referenced as metasurfaces, metafilms, or metastructures, composed of periodic wavelength-scale features can be made with favorable effective properties, enabling the manipulation of electromagnetic waves for a wide variety of photonics applications [22,24,58,96-99]. These compact structures serve as alternatives to conventional bulk optical devices while enabling a host of new design options. Varying the periodicity of these features accompanied by appropriate lossless dielectric materials, one can tune the operating wavelength ranging from ultraviolet (UV) to radio frequency (RF). Among the significant characteristic properties of metasurfaces is the coupling of incident light to laterally propagating leaky Bloch modes in the subwavelength regime when the periodicity of the unit cell is moderately smaller than the free-space wavelength [11]. This property, which manifests itself as a resonance at certain wavelengths, has been shown to be foundational for the wide variety of exotic behaviors found in metastructures [100-102]. Working in the subwavelength regime guarantees that only zero-order diffraction prevails. As the period increases relative to the wavelength, higher diffraction orders begin to propagate and manifest themselves in the optical spectra of the metastructures which is well known from classical diffractive optics theory and experiments.

Most of the literature on periodic metasurfaces has focused on conventional one-dimensional (1D) or two-dimensional (2D) periodic grating lines or posts composed of only one protrusion and one associated groove (i.e. two-part fill factor) within one period. However, in the present context, some past studies on periodic metasurfaces containing multiple ridges or multiple filling factors in a one unit cell are relevant. For instance, in 2004, Ding and Magnusson used an asymmetric four-part fill factor (period contains two ridges and two grooves) subwavelength periodic structures to design numerous types of advanced devices based on the guided-mode resonance (GMR) effect [7]. More recently, planar lenses based on metasurfaces with four-part fill factors have been reported to suppress chromatic aberration for imaging applications [103]. Lin et al. made use of four-part fill factor design to steer visible wavelengths to a large deflection angle [104]. In 2018, 1D and 2D four-part fill factor metasurfaces were used to achieve wideband antireflection devices [105]. Moreover, in 2019, Ilic and Atwater reported the levitation and propulsion of a macroscopic object based on an asymmetric unit cell having four-part fill factor design [106]. These examples highlight the importance of developing novel advanced technologies based on multipart unit cell metasurfaces as well as exploring the new design spaces revealed by this added capability.

Figure 5-1 displays some concrete examples supporting this viewpoint. Elaborated in **Figure 5-1(a)** are representative symmetric and asymmetric

metasurfaces so classified by the value of their fill factors as shown there. Useful applications of four-part grating devices are exemplified in **Figure 5-1(b)-(e)** using silicon-on-glass as material platform. For instance, **Figure 5-1(b)** shows the tunability of the resonance wavelength by introducing asymmetry to the symmetric two part grating design via changing the gap (F_2) between two ridges with fixed widths (i.e. F_1, F_3=constant). Comparing TE-polarized reflection spectra of two symmetric wideband designs, **Figure 5-1(c)** represents a significant bandwidth improvement (~475 nm wider) for the design with four-part period [7,40]. Finally, we show in **Figure 5-1(d)**, e that transferring from symmetric to asymmetric four-part period device results in a narrow band transmission filter showing very low sidebands across a ~400-nm wavelength range.

Until now, most fabricated four-part fill factor devices have employed electron-beam lithography methods. This method of fabrication is time consuming, expensive, and impractical when applying patterning on large areas because of stitching issues and a restricted area of exposure. Among nanofabrication methods, laser interference lithography (LIL) enables rapid realization of high- quality periodic structures on a large surface area. This method offers versatility for fabricating diffractive elements and metastructures because the periodicity and fill factor can be altered without the use of traditional masks [107,108]. One advantage of LIL is that in comparison with electron-beam lithography, it does not require high vacuum chamber for patterning. LIL is based on the interference pattern

generated by at least two coherent laser beams ($N \geq 2$). Three-dimensional (3D) structures with sub-micrometer periodicity were fabricated in 30-μm-thick photoresist (PR) film via interference of four non-coplanar laser beam (N=4) [109]. Moreover, interference of three laser beams in pattern-integrated interference lithography (PIIL) was used to fashion photonic crystal lattices with integrated functional elements via a single-exposure process [110]. Interference of multiple non-coplanar laser beams is unlike two-beam interference in that the polarization of the multiple beams will not be in the same direction. Therefore, we use the simple two-beam interference configuration with sequential exposures to achieve precise control over the interference-fringe contrast in each exposure that translate to the resultant pattern features.

Employing two-beam interference lithography, 2D periodic structures can be realized by applying two sequential exposures and by rotating the substrate in its plane to $\varphi=90^{o}$ after the first exposure. There are also studies on fabrication methods of nanostructures based on multiple exposures with different sample rotation angles (φ) in between. For example, fabrication of n-fold 2D photonic quasi-crystals has been reported based on repeated exposures and rotation of the sample n/2 times [111]. Simulation of more complicated patterns via the multiple exposure method has been reported based on a single repeated exposure at a specific angle of sample rotation [112]. Interference of multiple beams based on the

diffraction orders originating from appropriately-designed phase masks leads to fabrication of nanomotifs with different shapes [113].

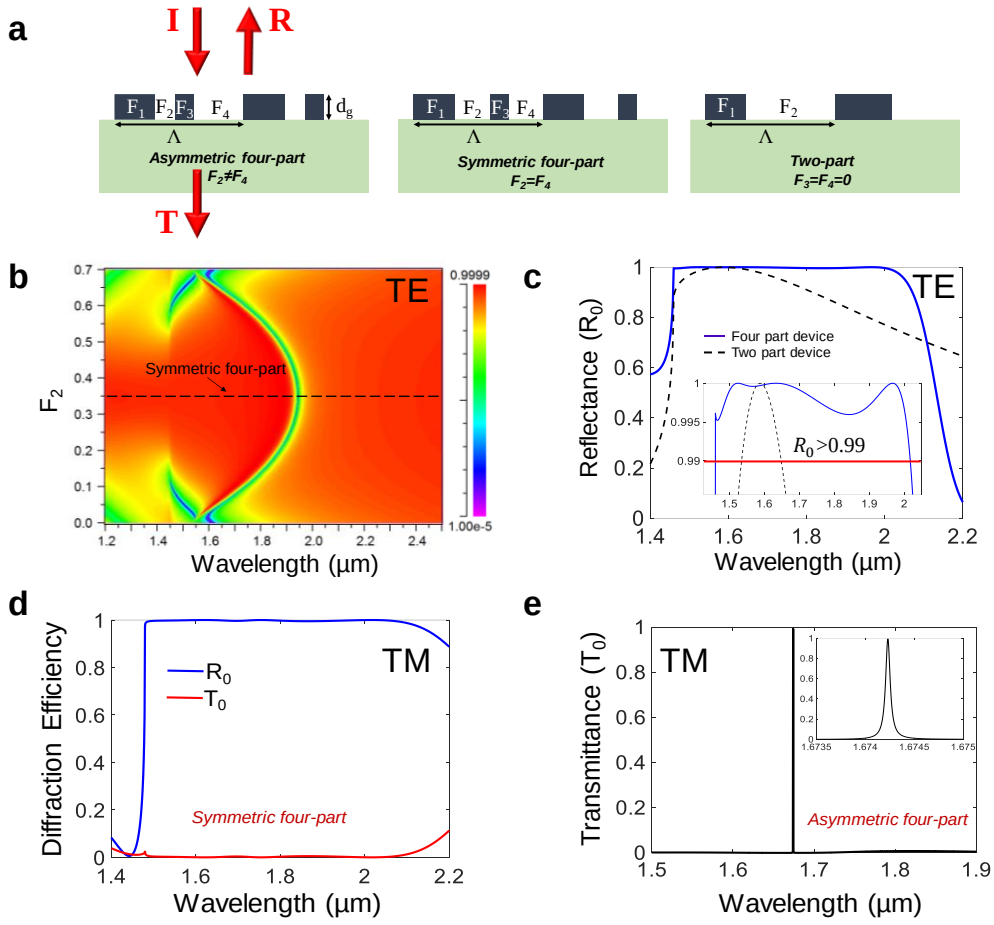

Figure 5-1 Applications of four-part grating devices. (a) Symmetric and asymmetric guided-mode resonance device designs based on filling factor values in 1D grating structures with grating thickness of d_g. (b) Logarithmic scale transmission map with TE-polarized incident light while changing F_2 of a device with Λ=1 μm, F_1=0.2, F_3=0.1, and d_g=0.22 μm. (c) Zero-order TE-polarized reflection spectrum possessing R_0>0.99 with bandwidth of $\Delta\lambda$~600 nm for four-part design [7] (Λ=1 μm, F_1=0.075, F_2=0.275, and d_g=0.228 μm) and $\Delta\lambda$~125 nm of two-part design [40] (Λ=0.986 μm, F_1=0.329, F_2=0.671, and d_g=0.49 μm). (d) TM-polarized R_0 and T_0 spectra for symmetric four-part fill factor wideband reflector [7] F_2=F_4=0.125. (e) Asymmetric design with F_2=0.127 and F_4=0.123. All other parameters are fixed for parts (d) and (e) as Λ=1 μm, F_1=0.25, F_3=0.5, and

d_g=0.8 μm. Transverse-electric (TE) polarization refers to incident light electric field vector being orthogonal to the plane of incidence or along the grating grooves in this example whereas transverse-magnetic (TM) polarization refers to the magnetic vector being thus oriented.

Here, we report a new, expeditious fabrication method to fashion periodic devices with multi-fill factor unit cells based on LIL. This method of fabrication yields non-conventional periodic patterns on large substrates enabling realization of new emerging devices and technologies based on complex multipart fill factor metasurfaces. In summary, first, we apply two carefully controlled exposures with altered periodicities between the exposures without rotating the substrate with respect to its plane (φ=0) to make 1D four-part fill factor gratings. Repeating the same procedure while changing the rotation angle to φ=90 degrees, we obtain a 2D four-part unit cell metasurface. We also show that multipart (i.e. greater than four) fill-factor metasurfaces are achievable via our fabrication method. We demonstrate the optical characteristics of a fabricated proof-of-concept device for both transverse electric (TE) and transverse magnetic (TM) polarization of the incident light.

5.1 Fabrication method

First, we develop an example 1D four-part period grating with a periodicity of 1000 nm on silicon-on-quartz (SOQ) wafers (Shin-Etsu Chemical Co., Ltd.). This wafer contains 220 nm crystalline silicon on a quartz substrate, both of which are lossless in the near infrared wavelength range. In a representative process to

fabricate the device, the SOQ substrates measuring 2.5x2.5 cm^2 are spin-coated at 3000 rpm with SEPR 701-2.9, a positive photoresist (PR), for 1 minute after the primer is applied. The spin-coated substrates are then soft baked for 90 seconds at 110°C followed by patterning using laser interference lithography (LIL). We employ a Lloyd's mirror interference lithography configuration which consists of a high-quality mirror mounted orthogonally to the sample holder stage. A schematic of this system is depicted in **Figure 1-4**. In our setup, the intensity of the laser light is measured as I ~96 $\mu W/cm^2$ at the sample surface. Each exposure has a periodicity that is determined by $\Lambda=\lambda/2\sin\theta$ in which λ is the laser wavelength (266 nm in our case) and θ is the bisector of the angle between the two interfering beams. This angle can be precisely controlled by rotating the stage [114]. Therefore, changing θ allows one to change the periodicity of the grating.

In order to realize four-part fill factor periodic gratings, the PR-coated substrates are double exposed with two different periods (Λ_1 and Λ_2) and exposure times (t_1 and t_2) to create a 1D photoresist mask as shown schematically in Fig. 3. It is necessary that the periodicity of the second exposure be half of the first exposure period ($\Lambda_2=1/2\ \Lambda_1$) to achieve a uniform four- part fill factor grating as shown in **Figures 5-2(a)** and **5-2(b)**. Most importantly, the exposure time for the first and second exposure should be optimized in such a way that the first exposure be underexposed. If this optimization is correctly implemented, the second exposure dose will add to the first one, resulting in two different grating ridge

widths. Therefore, precise control over these parameters is required to achieve high-quality results. In practice, finding the optimal exposures requires experimentation and tuning which once established can be successfully applied in subsequent fabrication.

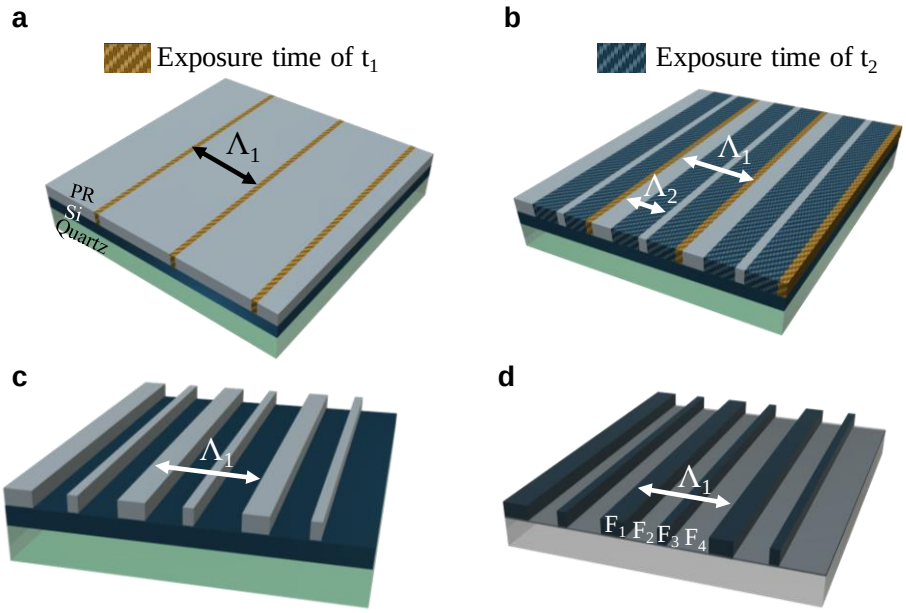

Figure 5-2 Schematics of the fabrication process of four-part period metasurfaces via the LIL method. (a) First exposure with periodicity of Λ_1 and exposure time of t_1 on a PR-coated SOQ wafer. (b) Second exposure with periodicity of Λ_2=1/2 Λ_1 and exposure time of t_2. (c) Developed PR after two exposures. (d) Transferred four-part periodic pattern from PR to Si via the RIE process.

In this work, to achieve four-part fill factor gratings with periodicity of 1000 nm, the longer period Λ_1 = 1000 nm is exposed first for 10 seconds followed by the smaller period Λ_2 = 500 nm exposed for 34 seconds. For this four-part metagrating, the longer periodicity defines the periodicity of the final device. Post-exposure, the substrates are baked at 110º C for 90 seconds and then developed in AZ 917 MIF

developer for 45 seconds, as shown in **Figure 5-2(c)**. The asymmetric pattern on the PR is transferred to c-Si by dry etching, as illustrated in **Figure 5-2(d)**, in an Oxford PlasmaLab 80plus etcher using SF_6 and CHF_3 for 7 minutes with RIE power of 100 W which gives an etch rate of about 30 nm/min. Etching time defines the thickness of the final metagrating (d_g). The remaining PR is removed using an O_2 ashing process. The final device dimensions are measured by using scanning electron microscopy (SEM) and atomic force microscopy (AFM).

Similar to fabrication of 1D structure, 2D structures can be fabricated via two identical exposures at φ=0 degrees following two exposures at φ=90 degrees. However, at each φ, approximately half of the exposure doses used in the 1D metagrating are applied to create the 2D structure. In other words, two exposures are carried out at φ=0 degrees with Λ_1 = 1000 nm and t_1=5 seconds followed by Λ_2 = 500 nm for t_2 = 17 seconds. The same exposure periods and times are applied to the PR after sample rotation of 90 degrees. This results in 2D spatially-modulated metasurfaces with a host of possible unit-cell architectures realizable.

5.2 Results and discussion

5.2.1 Devices with four-part unit cells

Figure 5-3 illustrates AFM images of a PR-patterned four-part fill factor metagrating at different second-exposure times while the first exposure is fixed at 10 seconds. It is clearly shown that the fill factors can be controlled by exposure energy. As the second exposure time increases, the fill factors of the final pattern decrease. This result is expected as we are using positive PR in these experiments.

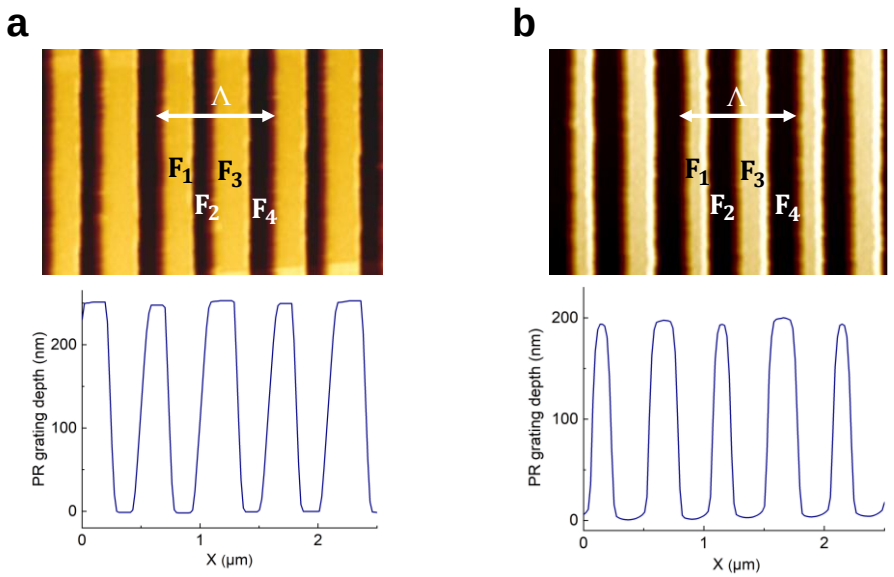

Figure 5-3 AFM images of four-part PR grating metasurfaces. Fixed first-exposure time t_1=10 seconds and varying the second-exposure time for (a) t_2=34 seconds and (b) t_2=45 seconds.

The schematic of the fabricated 1D and 2D multipart metasurfaces are shown in **Figures. 5-4(a)** and **5-4(b)**. **Figures 5-4(c)** and **5-4(d)** reveal SEM and AFM images of an etched asymmetric four-part periodic grating device fabricated

on the SOQ wafer based on our proposed method of fabrication. Within one period, the device shows two different widths of grating ridges and two different widths of grooves (i.e. four-part fill factors). A double exposure of Λ_1 = 1000 nm and Λ_2 = 500 nm on PR followed by the RIE process gives the final device a set of fill factors (F_1 = 0.2, F_2 = 0.34, F_3 = 0.1, and F_4 = 0.36). **Figure 5-4(e)** demonstrates SEM images of a 2D etched asymmetric unit cell fabricated by the four-time-exposure approach explained earlier. **Figure 5-4(f)** shows an AFM of this device.

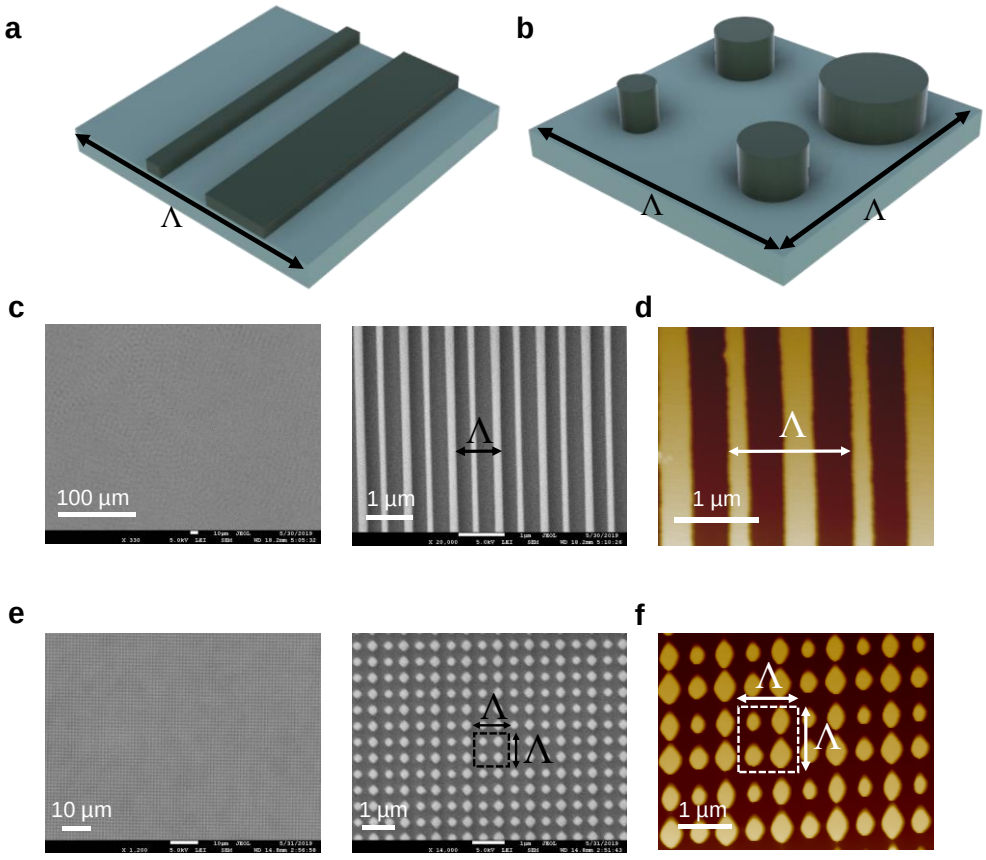

Figure 5-4 1D and 2D multipart metasurfaces. Schematic of device for (a) 1D and (b) 2D structures. Metrology of representative SOQ fabricated devices. (c) SEM

images of a 1D four-part grating at two different magnifications. (d) AFM image pertinent to the 1D four-part grating device. (e) SEM images of a 2D four-part unit cell metasurface at two different magnifications. (f) AFM image of the 2D four-part unit-cell metasurface.

5.2.2 Devices with multipart unit cells

The method of two exposures can be used to fabricate not only four-part periodicity, but also multipart unit cell diffractive elements and metasurfaces that are realized if the second exposure periodicity is not equal to half of the first exposure period ($\Lambda_2 \neq 1/2\ \Lambda_1$). Under this condition, the final device period is not defined by the longer period. The final period is set by the least common multiple of two the periods at work. Here, as an example, we use the double exposure method for exposures with periods of Λ_1=1000 nm and Λ_2=600 nm to obtain long periods containing multipart fill factors. We show in **Figures 5-5(a)** and **5-5(b)** that the period of the final device is Λ_f=3000 nm, which translates to the point where the two periodicities match each other (least common multiple) and repeat periodically. 1D and 2D meta-structures with changing fill factor avlues are shown in **Figures. 5-5(c)** and **5-5(d)** obtained by two exposures with periods of Λ_1=1000 nm and Λ_2=660 nm. It is obvious that in 2D device, fill factor varies in different directions.

In addition, and importantly, our method can be implemented to design and pattern nonperiodic metasurfaces and gratings. This happens when the least common multiple of the two periodicities at work becomes a large number. For instance, as shown in **Figure 5-5(e)**, choosing two periods of Λ_1=1233 nm and

Λ_2=835 nm results in the large global period of Λ_f=1,029,555 nm (~1 mm). Therefore, we can realize ~1 mm^2 areas containing aperiodic metastructures.

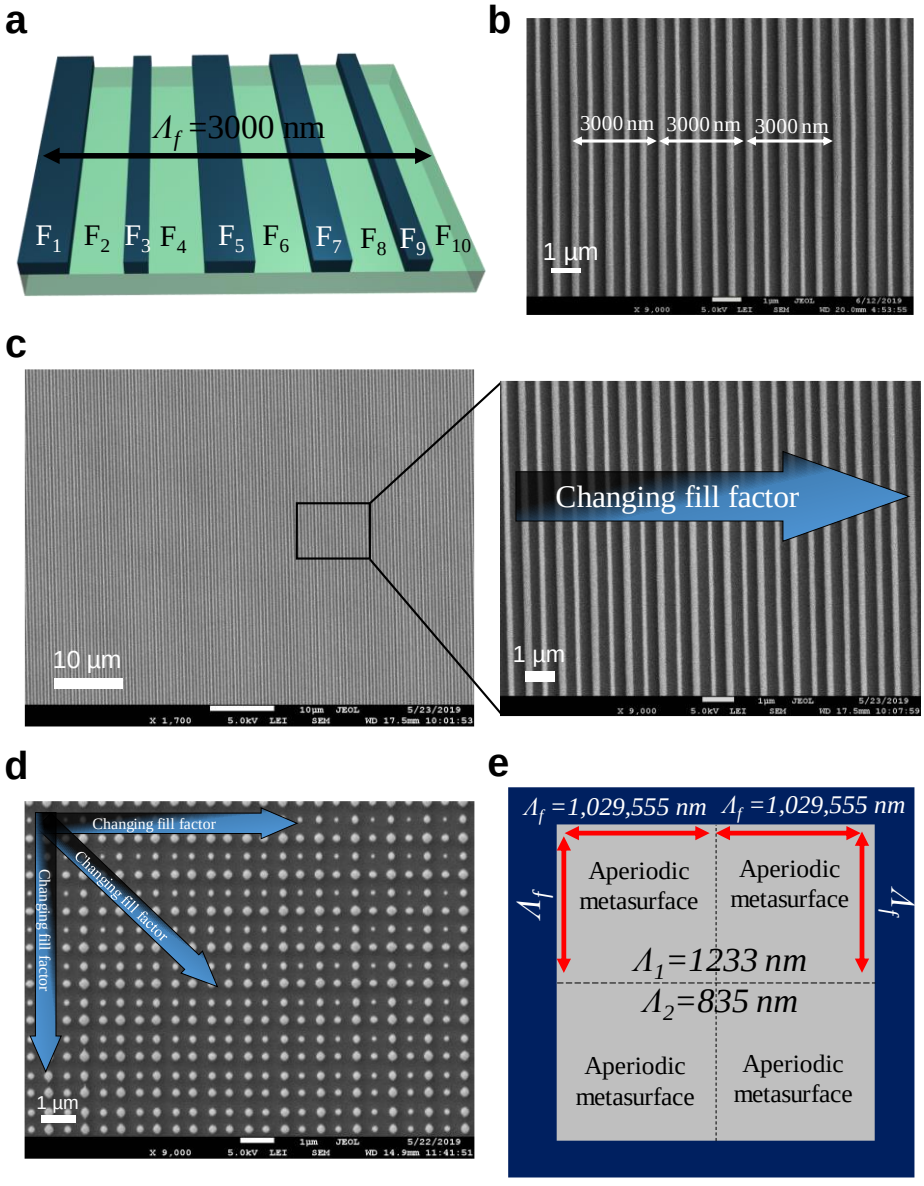

Figure 5-5 Multipart fill factor grating metastructures. (a) A schematic of a 10-part fill factor device with periodicity of Λ_f=3000 nm by choosing two periods of Λ_1=1000 nm and Λ_2=600 nm. (b) SEM image of a fabricated 10-part fill factor

device pertinent to 1D metasurface. SEM images of patterned structures choosing two periods of Λ_1=1000 nm and Λ_2=660 nm for (c) 1D and (d) 2D metasurfaces. (e) Schematic of a proposed ~1 mm^2 aperiodic metasurface obtained by two exposures with base periods Λ_1=1233 nm and Λ_2=835 nm.

The corresponding optical spectrum pertinent to the 1D multipart metasurface developed on SOQ is now investigated both theoretically and experimentally. The rigorous coupled-wave analysis (RCWA) method is employed for simulation of the device spectrum based on the dimensions of the fabricated proof-of-concept device. The low-loss, nondispersive nature of Si and quartz in the near-IR band allows use of constant real-valued refractive indices set to n_{Si}=3.45 and n_{quartz}=1.45 while performing simulations. **Figure 5-6** shows computed and experimental spectra. **Figures 5-6(a)** and **5-6(b)** show RCWA simulated transmission maps that represent variation of the grating thickness (d_g) for TM and TE polarization states, respectively. A wideband antireflection spectrum is observed for the TM case while the TE case shows a guided-mode resonance dip in the transmission simulations. We measure the spectra of the fabricated device and confirm wideband antireflection for TM and resonance characteristic for the TE case in **Figure 5-6(c)**. The zero-order transmission (T_0) measurement is carried out by collecting the transmitted output light using a detector and transferring it to an optical spectrum analyzer by means of an optical fiber. The simulated spectra of the fabricated SOQ device shown in **Figure 5-6(c)** correspond to a grating thickness of d_g=220 nm which is noted by dotted lines in **Figures 5-6(a)** and **5-6(b)** for the

case of TE and TM incident polarized light. The discrepancy between the measurement and simulation is related to the collimation issues and interference of two reflected beams, from two interfaces of the SOQ wafer, with the incident light. These points are ignored in the simulation.

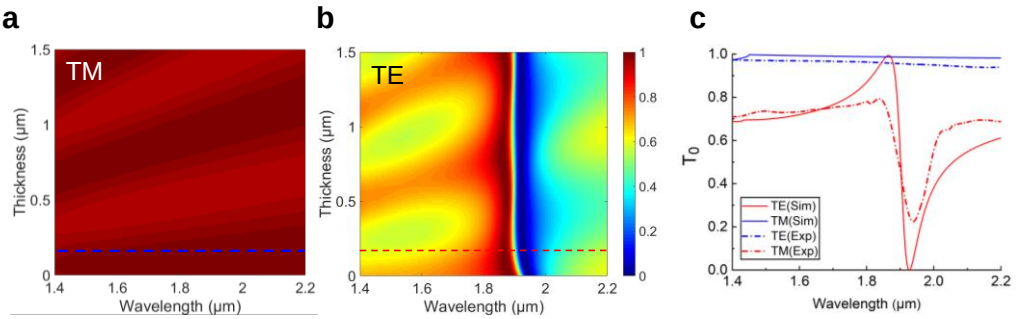

Figure 5-6 Computed and experimental spectra. Simulated zero-order transmission (T_0) optical spectral map as a function of grating thickness d_g for (a) TM, and (b) TE polarization of incident light. (c) Simulated and measured transmission spectra of a device with d_g=220 nm for both TE and TM cases. Parameters of the four-part period grating device are Λ=1 μm, F_1=0.2, F_2=0.34, F_3=0.1, F_4=0.36 which remain constant for (a)-(c).

5.3 Conclusion

In this work, we present a method applying two-time exposures generated by a LIL system to realize multipart periodic-unit-cell metastructures. The proposed method, which exploits the nature of the interaction between two different periodic UV-light patterns with precisely controlled exposure parameters, can be used to create new and emerging classes of metasurfaces recently found in applications for imaging, object levitating, and light propelled spacecraft, especially when patterning on large areas (~1 m) is required. The novel fabrication methods described here are tested to realize four-part and multipart unit-cell 1D and

2D periodic patterns in photoresist followed by etch steps to transfer the patterns to the SOQ platform for near-IR band device applications. Moreover, by appropriate selection of the two base periods, one can achieve millimeter-size final unit cells possessing aperiodic metastructures with one superperiod. AFM and SEM images of the fabricated devices in different magnifications reveal no signs of nonuniformity as demonstrated by imaging at multiple locations across these large surfaces. Finally, optical spectral measurements and simulations of one of the fabricated proof-of-concept devices indicates wideband antireflection and guided-mode resonance response for TM- and TE-polarized input light, respectively. This test device measures 100 mm^2, has 500 nm minimum feature size, and was fabricated in less than one hour including etching.

Chapter 6

Dual-grating metamembranes supporting bound states in the continuum

Bound states in the continuum (BICs), which were first proposed in quantum mechanics by von Neumann and Winger in 1929, have been extended into the realm of nanophotonics [115]. Although the term BIC appeared in photonics in 2008 [116], the concept behind this phenomenon was first reported by Kazarinov et al. in 1976 [117]. These researchers derived a formula for the quality factor of a corrugated waveguide and reported suppressed radiation loss at the upper band edge when the second-order Bragg condition was satisfied. Later, in 1979, Vincent and Neviere numerically demonstrated the existence of a non-leaky edge pertinent to symmetric grating designs while introducing asymmetry to the grating profile resulted in leaky radiating modes at both band edges [3]. Ding and Magnusson manipulated the separation of the non-degenerate leaky resonances associated with asymmetric profiles to engineer the resonant spectral response of periodic films [118]. Experimentally, the non-leaky edge, and thus BIC, was revealed in 1998 by imposing asymmetry on an otherwise symmetric periodic structure by variation in the angle of incidence [119].

Thus, optical BICs are grounded in confined (non-leaky) modes with an infinite lifetime above the light line in the dispersion diagram of periodic structures. Well established symmetry-protected BICs with exact zero resonance bandwidth (true BIC) reside at the Γ point of the band diagram based on the symmetry

incompatibility between the asymmetric standing waves inside the structure and symmetric outgoing waves [120-122]. In addition, it has been shown both theoretically and experimentally that off-Γ BIC, with near-zero resonance linewidth (quasi-BIC or asymptotic BIC) can be obtained at specific incident angles in periodic structures [123,124]. Moreover, quasi-BICs at the Γ point were reported for specific physical parameters of nanostructures [125]. These nearly-zero resonance linewidths possess quasi-embedded eigenvalues which cause coupling to the radiated waves.

Whereas there have been extensive studies conducted on metamaterial devices with a single spatial periodicity, there is less research on resonance elements containing multiple spatial periodic layers. Unquestionably, there are additional design dimensions to be exploited with such architectures as any multi-periodic construct will operate on available bound modes differently than a single periodicity. Thus, there are scientific and practical reasons to explore attendant device designs and corresponding spectral response. Past related work includes demonstration that properly designed dually-corrugated waveguides support unidirectional output radiation [5]. Similar elements were advanced as solutions to improve the efficiency and stability of second-order surface emitting laser diodes via substrate radiation suppression [5,126]. In 2014, a unidirectional coupler for surface plasmon polaritons was proposed and realized with a dislocated double-layer metal grating structure [127]. Bulgakov et al. employed the Fourier modal

approach to study BICs above the light line in double-sided grating designs based on symmetric and asymmetric structures [128]. In traditional metasurfaces, thin-film deposition of different materials is applicable to obtain desired thicknesses and refractive indices of device layers. The periodicity is subsequently inscribed by traditional means including holographic interference lithography and electron-beam patterning. In this work, we model and make grating-enclosed single-film membranes. Thus, nanoimprint lithography (NIL) with curable materials becomes the appropriate choice to demonstrate example resonant devices.

Thin photonic membranes can be made with various materials such as semiconductors or flexible polymers for various applications such as photonic crystals, pressure sensors, biosensors, and lasers [129-132]. For semiconductor photonic membrane metamaterials, traditional photolithography methods with wet etching and sacrificial layers support the fabrication process. Such membranes can attach to other substrates like flexible substrates via a transfer process [133,134]. Comparatively, employing NIL, which can be flexible and fast, abates some of the complexity associated with thin membrane fabrication.

In this study, we explore the spectral response and attendant novel features obtained by introducing a dual periodic scattering region in membrane designs. We find that the calculated transmission spectrum of a grating-enclosed homogeneous film shows quasi-BICs with high Q ($Q=\lambda/\Delta\lambda$ where $\Delta\lambda$ is the linewidth and λ is the resonance wavelength) as the thickness of the homogeneous layer varies. We

experimentally confirm spectral narrowing and broadening trends for fabricated double-grating metamaterials. We demonstrate by numerical simulation as well as experimentally that specific restrictions on the physical parameters need to be satisfied to obtain an ultra-narrow resonance linewidth as otherwise the linewidth of the resonance broadens with reduced resonant Q. The formulation defining these restrictions is applied here to establish a quasi-BIC at the Γ point.

6.1 Fabrication technique

The dual-grating membrane metamaterials presented here are fabricated through a peel-off process involving a cured polymer sandwiched between two patterned stamps. Usually, in NIL, patterns on a single stamp imprint resist on rigid or flexible substrates with the stamp then peeled off the cured resist [135,136]. Thick (~100 μm) double-sided structures made by NIL were fabricated through replicating two patterned surface treated molds [137]. In the present work, we deposit a UV curable polymer between two flexible patterned stamps to realize much thinner (~1 μm) free-standing dual-patterned membrane metamaterials. Choosing an appropriate polymer with minimal adhesion to the stamps enables fast single-step fabrication process which eliminates typical anti-stick surface treatment steps.

The fabrication process of double-sided grating membranes is schematically shown in **Figure 6-1.** The optical adhesive NOA73 with refractive index of 1.56

acts as the resist material which will turn into the polymer membrane. As NOA73 is thiolene based, there is relatively weak adhesion to the PDMS resulting in a clean separation of both top and bottom PDMS stamps. Our final device is a free-standing flexible membrane metamaterial containing patterns on both sides replicating each stamp. Typically, for high performance, guided-mode resonance devices are thin so as to support only a single, or few, leaky modes. The total thickness, including homogeneous layer thickness, can be controlled either by applying measured pressure or by using spacers between the master stamps. A PDMS spacer can be realized by UV light illumination of spin-coated positive photoresist through a rectangular mask followed by a development process similar to the method reported in Ref. [136].

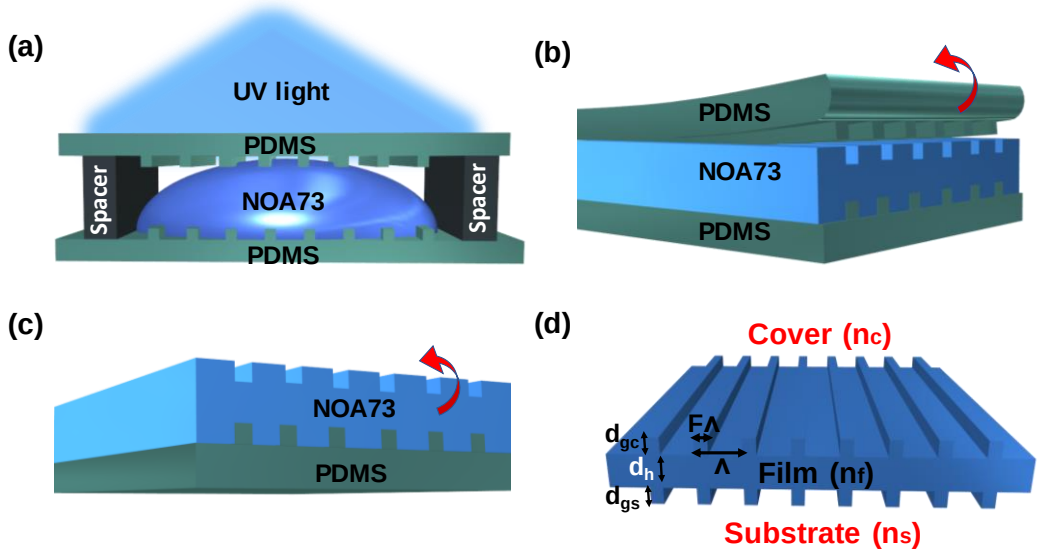

Figure 6-1 Schematics explaining fabrication of double-grating membrane metamaterials. (a) UV curing of the sandwiched polymer between patterned PDMS stamps with spacer-controlled thickness. (b) Top PDMS stamp peel off from the

cured polymer. (c) Cured patterned polymer release from the bottom PDMS stamp. (d) Final membrane metamaterial with specific physical parameters. The grating depths on the cover side and substrate side are denoted by d_{gc} and d_{gs}, respectively, while the homogeneous film thickness is labeled by d_h. Fill factor (F) is defined as the fraction of the grating period (Λ) filled with the high index material.

Figure 6-2 shows an AFM of the grating quantifying its depth and providing a 3D view along with SEM images related to the silicon master and the final fabricated membrane. In particular, **Figure 6-2(a)** shows the silicon master template after peel-off confirming an excellent process as there is no residual PDMS observed. Due to negligible shrinkage (~ 1.5%) of the NOA73, after the curing process, there is minimal difference between the dimensions of master template compared to the final device displayed in **Figure 6-2(b)**.

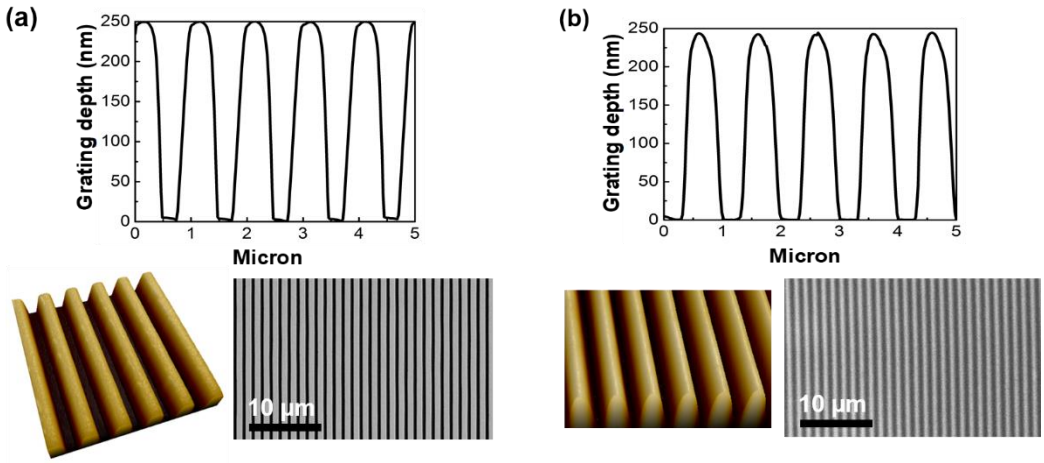

Figure 6-2 AFM and top view SEM images of the subwavelength grating lines. (a) Silicon master template after PDMS release. (b) Fabricated membrane device.

6.2 Metamembrane design and spectral characterization

Simulated zero-order transmittance (T_0) maps for single and dual-grating designs are displayed in **Figure 6-3**. The simulated spectra for TE polarization (incident electric-field vector lies along the grating lines) are obtained using the rigorous coupled-wave analysis (RCWA) method. It is clear that along the resonance loci in dual-grating designs, presented in **Figure 6-3(b)** and **6-3(c)**, there exist regions with vanishing resonant linewidths as well as regions with significantly large linewidths. Therefore, in double-grating designs as the thickness of the homogeneous layer reaches specific values, BICs emerge as the resonance linewidth asymptotically approaches zero. This behavior is absent in the map for the single-grating design as shown in **Figure 6-3(a)**.

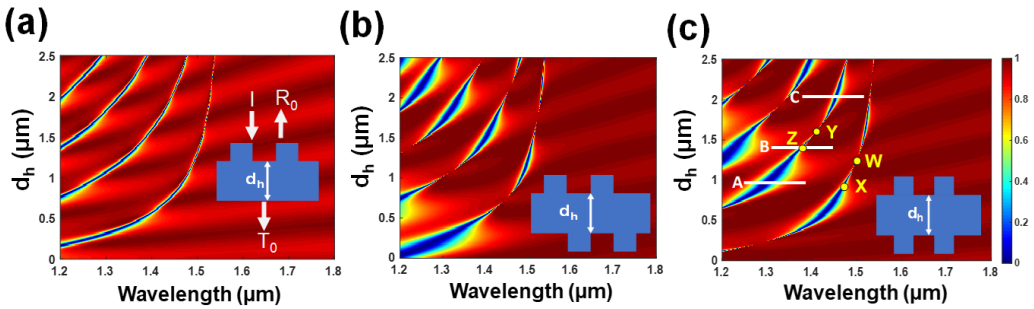

Figure 6-3 Simulated zero-order transmittance (T_0) spectral map as a function of homogeneous layer thickness (d_h) for TE-polarized incident light at normal incidence. (a) Single grating metamaterial design. (b) and (c) Dual-grating metamaterial designs. Insets show the schematic of each design. Physical parameters of Λ=1 μm, d_{gc}= d_{gs} = 0.25 μm, and F=0.45 are the same in all designs. The resonance loci show characteristics of classic slab waveguide mode plots with the TE_0 mode belonging to the trace at the longest wavelengths.

Figures 6-4(a)-4(c) demonstrate the experimental results and SEM images of three freestanding dual-grating metamembranes in air. The zero-order transmission spectra are measured using a spectrum analyzer with a matched supercontinuum light source covering the spectral region shown. These devices correspond to the selected homogeneous layer thicknesses of regions A, B, and C shown in Figure 3(c), respectively, where the resonance is associated with a ~TE_1 leaky Bloch mode. A good agreement between the measured transmission results and the predictions from the simulations is obtained. As shown, the full width at half maximum (FWHM) of the experimental spectra decreases from 50 nm to 5 nm and then increases again to 15 nm. We note that region B is near but not at the spectrally narrow Y point with high Q. Since our data acquisition system has a resolution of ~1 nm, we take the measurement at the wider location linewidth. These results confirm the resonance narrowing and broadening trends observed in dual-grating design simulations shown in **Figure 6-3(c)**. To align the top and bottom gratings, consistent with the inset schematic of **Figure 6-3(c)**, we fold the PDMS stamp as illustrated in **Figure 6-4(d)**. This is one of the advantages of using flexible and foldable stamps. To make sure the alignment is perfect between the top and bottom parts of the PDMS stamp, we illuminate the stamp in **Figure 6-4(d)** with a green laser pointer and observe the diffraction orders from both gratings. Perfect alignment occurs when the two sets of diffraction orders line up. **Figure 6-4(e)** is a photograph of the fabricated device on a sample holder with a hole in the

center of the holder to highlight the fact that the fabricated device is surrounded only by air.

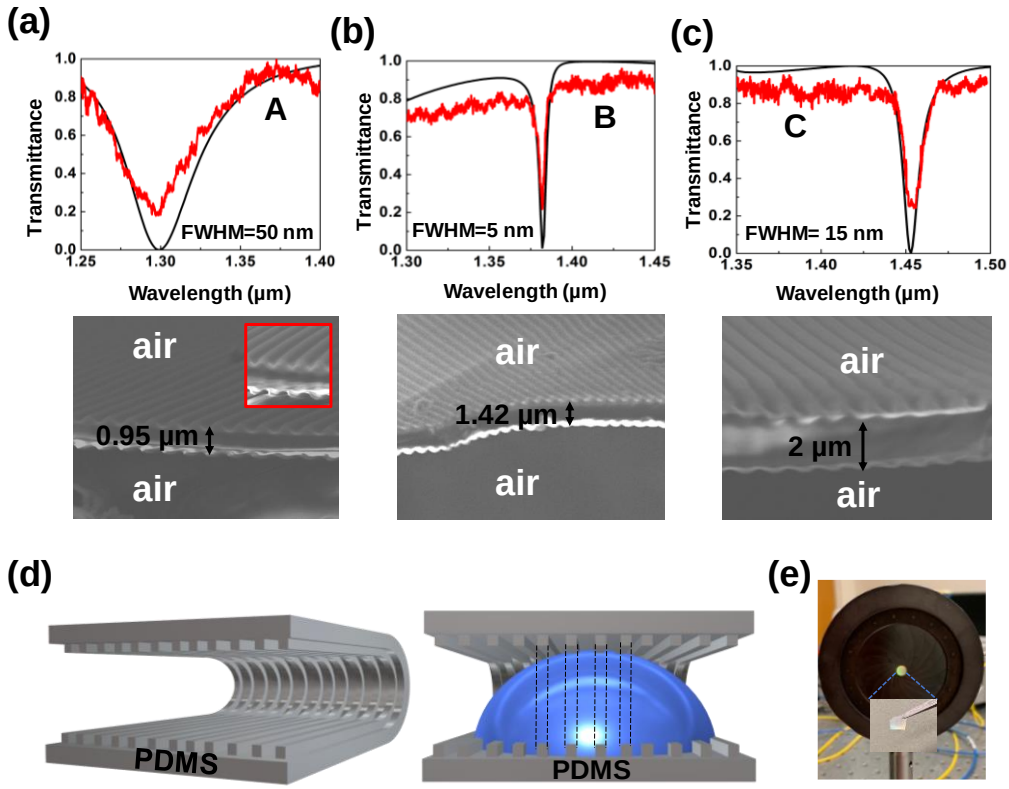

Figure 6-4 Experimental results of freestanding dual-grating metambrane. Simulated and measured transmission spectra under normal incidence of TE-polarized light and corresponding SEM cross-sectional images of each free-standing membrane with different homogeneous layer thicknesses of (a) 0.95 μm, (b) 1.42 μm, and (c) 2 μm. Physical parameters of Λ=1 μm, d_{gc}= d_{gs} = 0.25 μm, and F=0.45 are the same in all designs and devices. (d) Fabrication schematics illustrating the folded-PDMS technique to align the gratings. (e) Photograph of the fabricated device on a sample holder.

6.3 Discussion and explanation

In 1989, Avrutsky et al. performed analysis based on the electromagnetic boundary conditions of a waveguide surrounded by two shallow sinusoidally corrugated boundaries to derive formulas for radiation losses into the cover medium and to the substrate [5]. They found that properly designed dual-grating waveguides can lead to a unidirectional output radiation towards the cover or the substrate. This result is important as the total number of photons in play can, in principle, be sent to a single receiver. Device schematics, with the sinusoidal gratings assumed in Avrutsky's work and with rectangular gratings used here, are shown in **Figure 6-5(a)**.

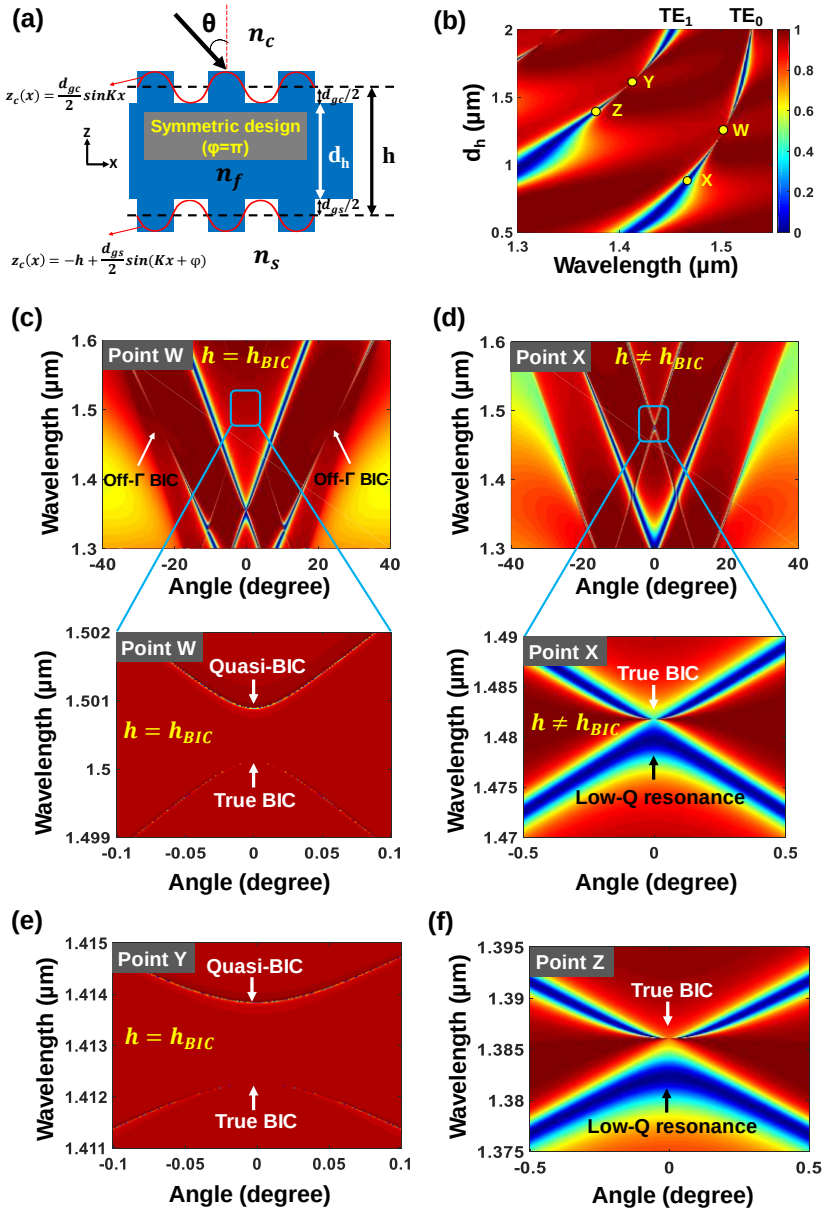

Figure 6-5 BIC properties of a symmetric dual-grating metamembrane with lateral grating phase shift of φ=π. (a) schematic design, (b) Simulated transmission map as a function of homogeneous layer thickness. Angle-resolved transmission spectra for TE_0 mode at (c) $h=h_{BIC}$, (d) $h\neq h_{BIC}$ and TE_1 mode at (e) $h=h_{BIC}$, (f) $h\neq h_{BIC}$. At $h=h_{BIC}$, the TE_0 mode is resonant near λ~1500 nm whereas the TE_1 mode resonates near λ~1413 nm.

For designs of φ=π and φ=0, radiation suppression towards the cover is possible if [5]

$$\frac{d_{gs}}{d_{gc}} = \frac{E_c(\mathrm{n}_f^2 - \mathrm{n}_c^2)}{E_s(\mathrm{n}_f^2 - \mathrm{n}_s^2)} \tag{6.1}$$

$$kn_f h = m\pi \tag{6.2}$$

where m is an integer, k is the wave number in free space, E_c and E_s represent the mode field amplitudes on the boundaries, and n_c, n_f, and n_s are the refractive indices of the cover, membrane, and substrate, respectively. One can further derive a formula for the electric field amplitudes on the cover-film (E_c) and substrate-film (E_s) interfaces [138] as

$$\frac{E_c}{E_s} = \sqrt{\frac{\mathrm{n}_f^2 - \mathrm{n}_s^2}{\mathrm{n}_f^2 - \mathrm{n}_c^2}} \tag{6.3}$$

Substituting Eq. (6.3) into Eq. (6.1), and $\mathrm{k} = 2\pi/\lambda$ in Eq. (6.2), results in

$$\frac{d_{gs}}{d_{gc}} = \sqrt{\frac{\mathrm{n}_f^2 - \mathrm{n}_c^2}{\mathrm{n}_f^2 - \mathrm{n}_s^2}} \tag{6.4}$$

$$h_{BIC} = m\frac{\lambda_{res}}{2} \times \frac{1}{n_f} \tag{6.5}$$

These simple expressions are then the conditions for maximum transmission towards the substrate and radiation suppression towards the cover region. In a reflective resonant structure, radiation suppression towards the cover

compel the bandwidth of the reflection resonance vanishes. Equation (6.4) shows the grating depths ratio should be selected such that destructive interference comes into play in accordance with the conditions of equal contributions of each grating towards radiation into the cover. Based on this equation, having two identical grating depths results in high Q resonances only if n_c=n_s. Equation (6.5) gives the thickness value at which the highest Q occurs in dual-grating designs (h_{BIC}). This separation distance introduces destructive interference based on the π phase shift of the two resonances that arise from identical gratings at the top and bottom sides of the metamembrane. This thickness satisfies the condition for maximum transmission of the Fabry-Perot cavity. The transmittance of two identical parallel mirrors separated by a distance h in a Fabry-Perot cavity model is [139]:

$$T_{FP} = \frac{t^4}{1 + r^4 - 2r^2 \cos\delta} \tag{6.6}$$

where t and r are the transmission and reflection coefficients of the mirror, respectively, and $\delta = 2kh$ is the round-trip phase shift. The maximum transmission in the Fabry-Perot cavity occurs when $\delta = 2kh = 2m\pi$. This is equivalent to Eq. (6.5) defining the half-wavelength thickness condition. A half-wave thick film with $n_f > n_c, n_s$ is anti-reflecting thus promoting transmission whereas leaky-mode resonance is inherently reflective. These counteracting effects create the narrow BIC line. In addition, the highest Q factors (narrowest reflection resonance linewidths) in dual-grating designs are obtainable for $\varphi = m\pi$, ($m = 0, 1, 2, ...$)

when Eq. (6.4) and Eq. (6.5) are satisfied. Therefore, lateral grating displacement, film thickness, and grating-depth ratio substantially influence the resonant reflectance Q-factor in dual-grating designs. Note that $d_h = h - \frac{d_{gc}}{2} - \frac{d_{gs}}{2}$ as depicted in **Figure 6-5(a)**.

Figure 6-5(a) shows a schematic of a symmetric dual-grating structure with grating lateral displacement of φ=π. Designs with lateral phase shifts of φ=π and φ=0 are symmetric possessing mirror symmetry with respect to the z-axis. **Figure 6-5(b)** shows a simulated zero-order transmission map of the dual-grating metamaterial. This figure is a magnified version of **Figure 6-3(c)**; we repeat it here for easy reference. **Figure 6-5(c)** and **6-5(d)** demonstrate angularly-resolved transmission spectra supporting resonant TE_0 modes for homogeneous layer thicknesses of $h=h_{BIC}$ and $h\neq h_{BIC}$, respectively. Bottom panels in **Figure 6-5(c)** and **6-5(d)** show an expanded view of the blue-box enclosed section of the wide angular map. Similar transmission maps are shown in **Figure 6-5(e)** and **6-5(f)** for the TE_1 resonant mode for thicknesses of $h=h_{BIC}$ and $h\neq h_{BIC}$, respectively. These figures confirm that as long as the symmetry of the design is preserved, at normal incidence (θ=0), a true (symmetry protected) BIC ensues at one band edge while the other band edge generates a guided-mode resonance. The resonance Q is tuned by changing the thickness of the structure such that at thicknesses h_{BIC}, pertinent to points W and Y shown in **Figure 6-5(b)**, BICs arise at each band edge, one being a true BIC via symmetry protection and the other a quasi-BIC according to the

simple model in Eq. (6.4) and Eq. (6.5). At these points the resonance linewidth vanishes with $Q \rightarrow \infty$. We see that deviation from these thicknesses in symmetric structures results in transitions from quasi-BIC to low-Q resonances at selected points such as X and Z in **Figure 6-5(b)**. In addition, on moving from point W to point X, the true BIC transitions from the upper band edge (short wavelength) to the lower edge as shown in bottom panels of Figures **6-5(c)** and **6-5(d)**. This band flip phenomenon arises in each mode by varying the homogeneous layer thickness as seen in **Figures 6-5(c)-5(f)** [140]. Furthermore, angular transmission spectra show that at off-normal incidence, true BICs couple to the radiation continuum which results in resonant leaky modes appearing at both the upper and lower band edges. At the lower band edges, as the incidence angle approaches zero ($\theta \rightarrow 0$), the resonance linewidth falls until it completely disappears at $\theta=0$ the Γ point. It is also shown in the upper panel of **Figure 6-5(c)**, that the metamembrane supports off-Γ BICs at specific angles of incidence. Therefore, at a specific thickness of the homogeneous layer ($h=h_{BIC}$) a true BIC, a quasi-BIC at Γ, and a quasi-BIC off Γ exist in the device.

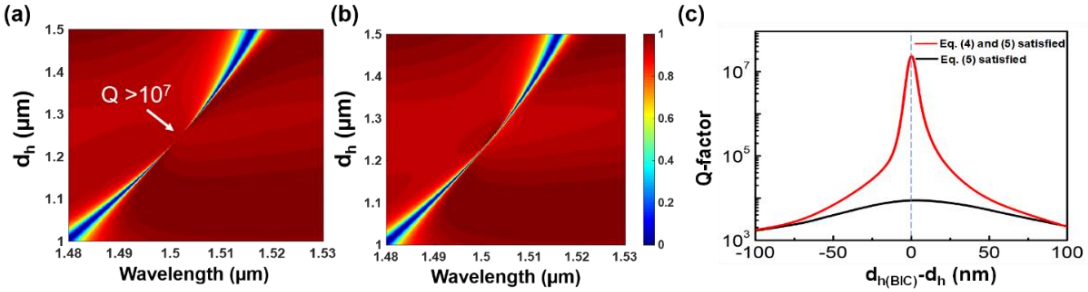

Figure 6-6 Transmission map as a function of d_h for a double-grating membrane metamaterial in air. (a) d_{gs} = d_{gc} = 0.25, and (b) d_{gs} = 0.2, d_{gc} = 0.3. Design parameters are Λ=1 μm, F=0.45, $\varphi = \pi$. (c) Calculated quality factor versus deviation from half-wavelength thickness related to designs (a) and (b).

Computed TE transmission maps of metamembranes in air are plotted in **Figures 6-6(a)** and **6-6(b)**. These figures confirm that the narrowest linewidth with Q~ 4×10^7 occurs when both values of the grating-depth ratio and the film thickness follow Eq. (6.4) and Eq. (6.5). According to **Figure 6-6(c)**, for an arbitrary ratio of grating depths (d_{gs}/d_{gc}), the Q is relatively low even when the half-wavelength thickness condition holds. Therefore, the half-wavelength thickness condition is necessary but not sufficient for vanishing resonant linewidth. Indeed, **Figure 6-6(c)** quantifies the gain in Q when both conditions represented by Eq. (6.4) and Eq. (6.5) hold.

6.4 Conclusions

In this work, the resonance properties of dual-grating metamaterial architectures are explored experimentally and theoretically. The distinction between the ordinary single-grating resonance device and a dual- or multi-grating

device is of primary interest. It is clear that there are new mechanisms and additional design dimensions to be exploited with such architectures as the multi-grating device will operate on available Bloch modes differently than a device containing a single-grating. These membrane-type metamaterials are realized by nanoimprint lithography using silicone master stamps to mold a well-suited optical polymer. Indeed, we find that introducing the second subwavelength periodic region to the membrane design enables novel properties differing significantly from those of single-grating metamaterials. For instance, the simulated transmission map of the dual-grating devices illustrates highly-variable resonance linewidth regions as the thickness of the homogeneous layer changes. At grating-depth and thickness values satisfying the analytical scattering model dicussed here, a high Q results implying a quasi-BIC on one band edge and a true BIC on the other. Our experimental spectral data obtained with the fabricated grating-enclosed homogeneous layer metamaterials confirm the predicted narrowing and broadening trends of the resonance linewidth. Moreover, it is shown that specific conditions on the relative lateral displacement of the gratings, thickness of the homogeneous layer, and grating-depth ratio defined by refractive-index values need to be satisfied to obtain the highest Q, while deviation from these conditions will reduce the resonance quality factor. Since quasi-off-Γ BICs arise also, three types of BICs can be found at specific physical parameters of the dual-grating structure. In this study, we use the simplest 1D canonical model possible to uncover the main properties

expeditiously. Nevertheless, we believe that the observed properties will apply to generalized photonic lattices containing multi-periodic regions in ordinary 2D metamaterials that are of high current interest.

Chapter 7

Fiber-facet integrated guided-mode resonance filters and sensors

Resonant gratings with clear prospects for applications have been studied since the early 1990's [11]. Prior to that, seminal contributions elucidating the nature of the fundamental effects, often termed "diffraction anomalies," appeared [3, 4]. The structural simplicity of this device class offers unique opportunities for integration and compact layout. Therefore, many concrete applications have been proposed. Efficient resonance devices possess subwavelength one-dimensional (1D) or two-dimensional (2D) periodicity. They are expeditiously fabricated with optical interference lithography or nanoimprint methods often taking a final form as a single, partially etched layer on a substrate. These devices operate on the basis of guided-mode, or leaky-mode, resonance. The resonance mechanism is grounded in leaky Bloch modes that are driven laterally by evanescent diffracted waves. There result useful variations in the intensities of the reflected and transmitted waves as the wavelength, angle of incidence, or any one of the physical characteristics of the device is varied around the resonance values. Recently, nanostructured resonance elements of this kind are sometimes called metasurfaces or metamaterials.

Whereas there is substantial literature in existence on resonance elements placed on bulk substrates, there are very few contributions treating fiber-mounted devices. The first fiber-tip-integrated guided-mode resonance filters were provided

by Tibuleac et al. [141] and Wawro et al. [78]. In this early work, guided-mode resonance (GMR) devices were fabricated by first depositing thin films of silicon nitride on clean, uncoated optical fiber facets by sputtering. Then a photoresist film was deposited on the silicon nitride and a grating recorded in it by UV-laser interferometry. Experimental GMR transmittance notches of ~18% were observed. Biomedical sensors and spectral filters were proposed as applications of fiber-endface GMR elements [141,142].

Optical fiber technology has advanced dramatically over time since its humble beginnings. Optical fibers enable modern telecommunications networks including the internet. The ubiquity and utility of the basic fiber motivates pursuit of methods and technology to integrate photonic devices directly on them. With fiber cores ranging in size from a few micrometers to hundreds of micrometers and total diameter including the cladding being approximately a millimeter, there are inherent difficulties in handling a device platform in the form of a cut fiber. Historically, the first fiber tip devices were microlenses made with photoresist fabricated directly on fiber facets by UV-illumination through the fiber itself [143]. Following this pioneering work, many research groups developed and proposed a broad range of applications and fabrication methods for fiber tip devices as comprehensively reviewed by Kostovski et al. [144].

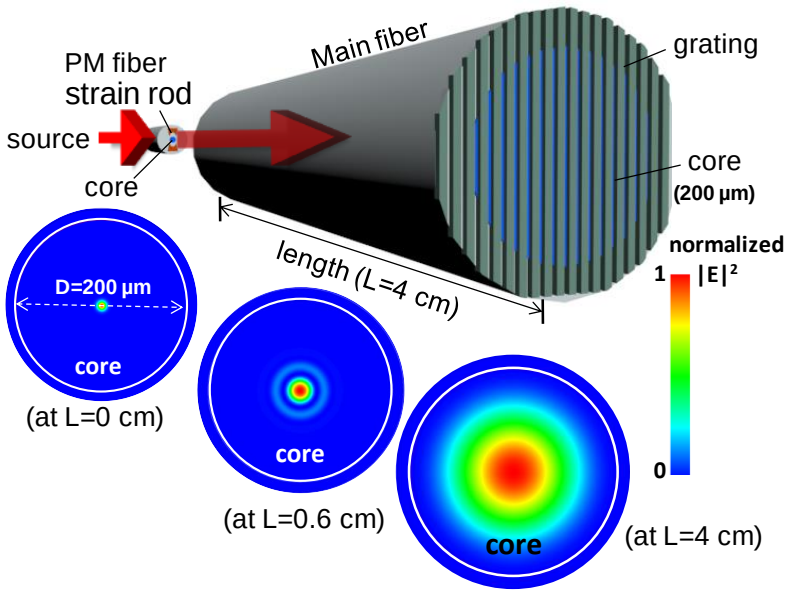

Figure 7-1 Simulation of beam propagation in a multimode fiber to establish the light distribution incident on the fiber-tip GMR device. Shown is a schematic of the integrated GMR filter with the beam source being coupled to the main fiber by a polarization maintaining (PM) fiber. The intensity distribution ($|\mathbf{E}|^2$) of the guided beam is numerically characterized using the beam propagation method with samples of the beam distribution along the fiber illustrated in the figure. Here, **E** denotes the optical electric-field vector.

Here we remark only on work most closely connected to the current topic of periodic structures on fiber facets. As precursors to the fiber-tip resonant sensors, Wawro reported fabrication of gratings where the ±1 diffraction orders contained ~50% of the total output power at the HeNe laser wavelength. The fiber coupled grating showed clear color spectra under white light illumination. Surface-relief gratings with period of 2 μm were fabricated on an optical fiber tip coated with azo polymer via interferometry to obtain diffraction pattern containing the zeroth and first orders under illumination with a 635 nm laser source [145]. Subsequently, Lin

et al. used e-beam lithography to create gold nanodot arrays on a fiber tip for surface-plasmon resonance sensors and gold nano-grid to fabricate ultra-wideband fiber inline polarizer on the fiber tip [146]. Dhawan et al. used focused-ion beam milling for direct writing and patterning on a facet of a gold deposited optical fiber [147]. Other notable works applied nanoimprint lithography to fashion ordered nanostructures on fibers [148-150]. In contrast to these cited works, here we report advances in fiber-tip guided-mode resonance filters and sensors with both theoretical modeling and experimental verification presented.

A waveguide mode propagating in the fiber is taken as an input wave to find the spectral response of the resonant filter. **Figure 7-1** illustrates the assumed geometry that is consistent with the experimental setup. To operate the GMR filters in TE (electric field parallel to groove) polarization, we use a polarization maintaining (PM) fiber that provides a linearly polarized Gaussian output beam (width, W=9.5 μm). This beam is coupled into the main multimode fiber and guided towards a fiber-facet integrated 1D GMR grating as noted in the figure. Here, we use a large diameter (D=200 μm) main fiber to support the resonant grating on the core. The field distribution of the waveguide mode along the main fiber (length, L=4 cm) is numerically characterized by the beam propagation method (BPM) using an iterative function [151]. At L=0 cm, as shown in **Figure 7-1**, the beam profile indicates the intensity distribution of the Gaussian output beam from the PM

fiber. As it propagates along the main fiber, the beam gradually spreads and forms a broadened Gaussian at the end of fiber.

To investigate the spectral response of facet-mounted GMR filters with the characterized beam profile as input, we perform a 3D finite-difference time-domain (FDTD) simulation using a high-performance computer. As illustrated in **Figure 7-2(a)**, the Si_3N_4 grating is on the tip of the fiber and its structure is defined by a corresponding grating parameter set {period Λ=1.03 μm, fill factor F=0.77, grating depth d_g=0.2 μm and sublayer thickness d_h=0.15 μm}. The refractive indices of Si_3N_4 and core are 1.9 and 1.45, respectively. The input beam is that found by the BPM illustrated in **Figure 7-1**.

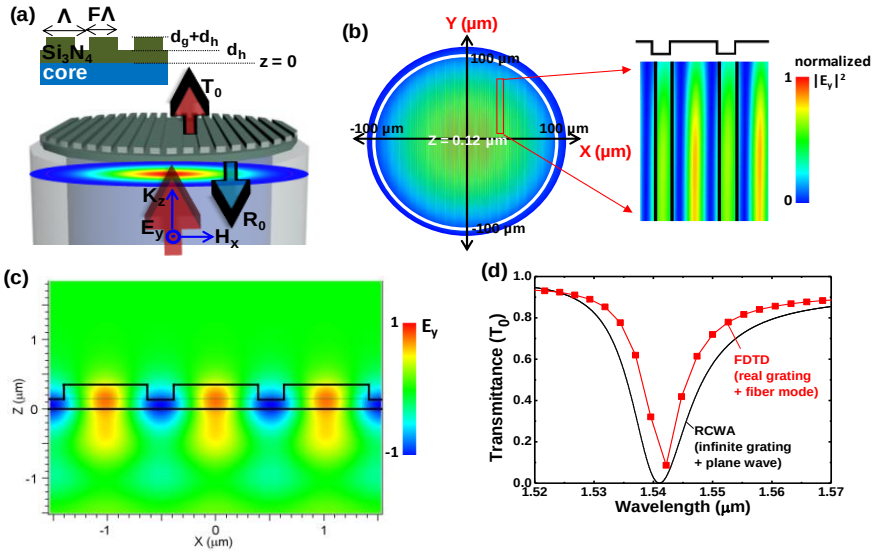

Figure 7-2 Spectral response based on characterized beam profile as input. (a) An integrated GMR filter fashioned with a Si_3N_4 grating on the tip of a fiber where the grating parameters are Λ (period), F (fill factor), d_g (grating depth), and d_h (sub layer thickness) are shown. (b) Calculated steady-state intensity distribution $|E_y|^2$ in

an integrated GMR at λ=1.543 μm by FDTD. (c) Calculated field distribution (E_y) in a periodic Si_3N_4 grating using RCWA at λ=1.541 μm (d) Comparison of transmittance T_0 spectra for the integrated GMR filter using FDTD with an infinite grating filter on substrate using RCWA.

The calculated field distribution in the grating at the resonance wavelength (λ=1.543 μm) is shown in **Figure 7-2(b)**. With a large diameter (D=200 μm) of the main fiber, numerous Si_3N_4 grating periods (N=193) fit onto the core. The figure shows how the resonant mode localizes on the fiber facet; the finite lateral extent of the input wave affects the distribution. The local mode-field distribution is similar to that in an infinite grating with plane-wave input as shown in **Figure 7-2(c)** which is calculated by rigorous coupled-wave analysis (RCWA). In **Figure 7-2(d)**, we compare the simulated zero-order transmittance spectra (T_0) for the real grating on fiber computed by FDTD and an infinite grating simulated by the RCWA method. These spectra are similar as the fiber is quite large and the input Gaussian mode has a relatively flat phase front.

After stripping the multi-mode fiber (MMF), it is cleaved to create a flat end-face which acts as a substrate for the fiber-mounted GMR device. To deposit Si_3N_4 on the fiber tip, the cleaved fiber is held in a mounting chuck which is placed inside a sputter chamber. A test substrate is also used to determine the deposition rate and refractive index of the sputtered Si_3N_4 thin film. According to ellipsometry measurements, the refractive index and the deposition rate of the sputtered Si_3N_4 film are n = 1.9 and 6 nm/min, respectively.

To fabricate reliable devices, we coat a uniform, thin layer of negative photoresist (PR) on the cleaved fiber tip to make the desired pattern. To do this, the fiber tip is dipped in PR and then the fiber is held straight for the spin coating process by a simple 3D-printed fiber holder. The spin coating process is accomplished successfully to reach a desired and relatively uniform thickness of PR. Then, the fiber is patterned with a laser interference lithography (LIL) system. In order to pattern the device, a spin coated fiber is mounted in a holder on an xyz controlled stage and fixed near the aperture of the interferometric exposure system. The exposure time is optimized according to the characteristics of the device. Two types of devices with different materials and physical characteristics are fabricated. One device consists of a homogeneous layer of Si_3N_4 topped by a patterned Si_3N_4 grating which is shown in **Figure 7-3(a)**. The Si_3N_4 grating is created by using a reactive-ion etching (RIE) process with a patterned photoresist mask. **Figure 7-3(b)** illustrates the second device consisting simply of a photoresist grating on top of a Si_3N_4 homogeneous layer without any etching process. The measurement setup is illustrated in **Figure 7-3(c)**. To measure the transmission spectrum of the fabricated devices, the laser light from the PM fiber is coupled into the cleaved multimode fibers supporting these GMR devices on their facets.

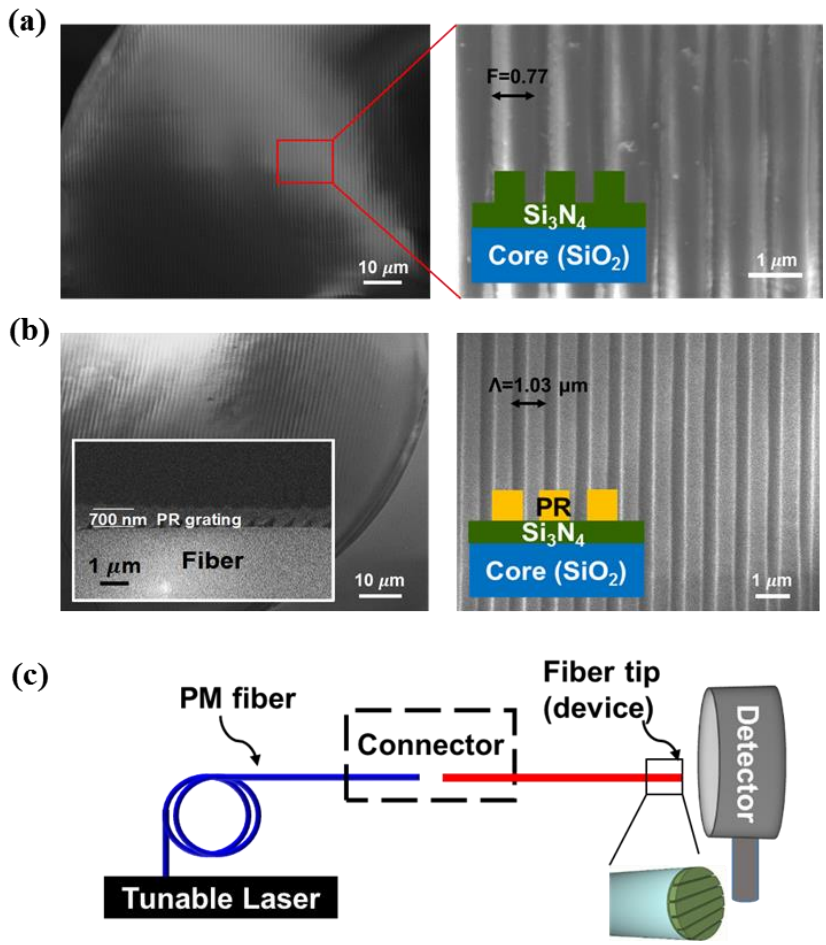

Figure 7-3 Experimental results. (a) SEM images of a fabricated GMR device which is an etched Si_3N_4 grating on a fiber tip with physical parameters of $\Lambda = 1.03$ μm, $d_g = 0.2$ μm, $d_h = 0.15$ μm, and $F = 0.77$. (b) SEM images of a fabricated PR-based GMR device on a fiber tip with physical parameters of $\Lambda = 1.03$ μm, $d_g = 0.7$ μm, $d_h = 0.19$ μm, and $F = 0.65$. (c) Measurement setup with connector to couple the laser light to the fiber for propagation to the resonance device.

Figure 7-4(a) shows the transmitted spectra for both etched and PR-based fiber-integrated resonance devices. The input light from a tunable InGaAsP laser couples to, and propagates in, the core region of the multimode fiber. The interaction of light with the fabricated fiber-mounted GMR devices with particular

physical parameters results in a dip at a specific wavelength in the transmission spectrum. Thus, spectral measurements verify the existence of GMR for these devices and, consequently, confirm that they can be used in spectral filtering applications. As we can see, the efficiency for the etched device is ~77% whereas that for the PR-based device it is ~62%. We can explain the reason for this efficiency difference by comparing the angular tolerance of the transmission spectra for both devices. According to **Figure 7-4 (b)**, we see that the angular aperture of the etched device is wider than that for the PR-based device. Therefore, the etched device accomodates the fiber mode more completely resulting in higher efficiency. There is good agreement between the experimental results in **Figure 7-4(a)** in resonance location and filter bandwidth as shown in **Figure 7-2(d)** for the silicon nitride device.

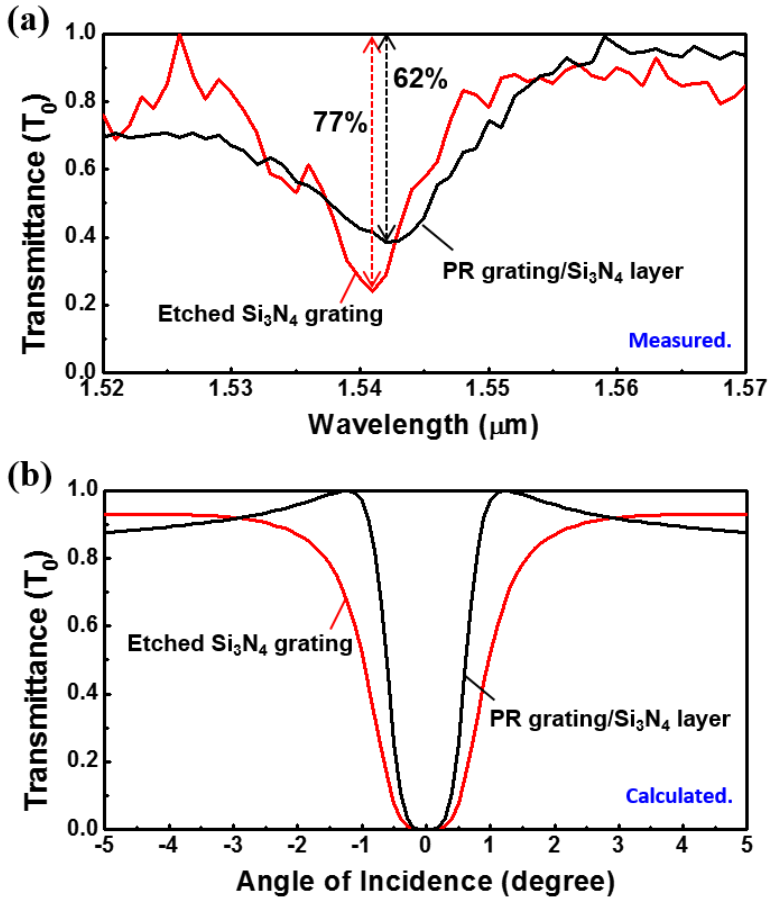

Figure 7-4 Measured and calculated spectra. (a) Experimental transmission spectra at normal incidence with TE polarized light measured with the fabricated devices. (b) Calculated angular tolerance of the transmission spectra for the experimental devices using plane-wave input.

Contemplating now the application of fiber-integrated GMR elements as sensors, we conduct a simple sensitivity test on the current prototypes. The sensitivity to a refractive-index change is typically reported in nm per refractive index unit (RIU), which indicates the resonance wavelength shift for a unit change of the refractive index. **Figure 7-5** demonstrates sensing by an etched fiber

integrated GMR device. Here, three different solutions, water (n=1.33), 50%-50% water-IPA (n=1.35), and IPA (n=1.37), are used. Based on simulated and experimental results it can be observed that this fiber integrated GMR device operates as a sensor exhibiting resonance wavelength shifts with respect to the change of the refractive index of its environment. For these solutions, a linear shift with respect to the increase in refractive index exist and the slope of this line shows the sensitivity of the sensor as ~200 nm/RIU.

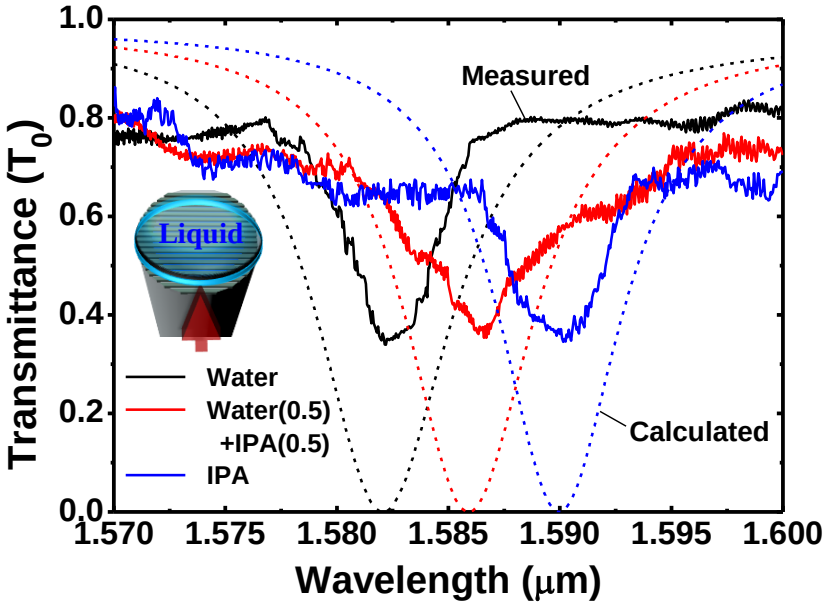

Figure 7-5 Calculated and measured transmission spectra for the etched silicon-nitride fiber device operating as a sensor in three different surrounding environments.

To summarize, we address both theory and experiment of fiber-mounted guided-mode resonance filters and sensors. We account for mode propagation along the multimode fiber using the beam propagation method. This establishes the

correct amplitude and phase distribution of the beam incident of the tip-mounted GMR element thus yielding an improved prediction of the resonance response relative to assuming a plane-wave incidence. In addition, two different fiber-integrated GMR devices are fabricated with and without an etching process for optical filtering applications. Spin coating and RIE-etch processes are employed to fabricate efficient devices while controlling the physical parameters. Transmission spectra found by simulations and experimental data for these devices are presented with good agreement found between theory and experiment. At last, sensor application of the etched device is investigated and an approximate sensitivity of 200 nm/RIU is measured.

References

1. R. W. Wood, “On a remarkable case of uneven distribution of light in a diffraction grating spectrum,” Philos. Mag. 4, 396–402 (1902).
2. Lord Rayleigh, “Note on the remarkable case of diffraction spectra described by Prof. Wood,” Philos. Mag. 14, 60–65 (1907).
3. P. Vincent and M. Neviere, “Corrugated dielectric waveguides: A numerical study of the second-order stop bands” Appl. Phys. 20, 345-351(1979).
4. E. Popov, L. Mashev, and D. Maystre, “Theoretical study of the anomalies of coated dielectric gratings,” Optica Acta, 33 607 –619 (1986).
5. I. A. Avrutsky, A. S. Svakhin, and V. A. Sychugov “Interference phenomena in waveguides with two corrugated boundaries” J. Mod. Opt. 36, 1303–1320 (1989).
6. S. S. Wang and R. Magnusson, “Theory and applications of guided-mode resonance filters,” Appl. Opt. 32, 2606-2613 (1993).
7. Y. Ding and R. Magnusson, "Resonant leaky-mode spectral-band engineering and device applications," Optics Express, vol. 12, no. 23, pp. 5661-5674, 2004.
8. D. Rosenblatt, A. Sharon and A. A. Friesem, "Resonant Grating Waveguide Structures," IEEE Journal of Quantum Electronics, vol. 33, no. 11, p. 2038, 1997.
9. C Y. Ding and R. Magnusson, “Band gaps and leaky-wave effects in resonant photonic-crystal waveguides,” Opt. Express, vol. 15, no. 2, pp. 680- 694, 2007.
10. R. Magnusson and S. S. Wang, “New principle for optical filters,” Appl. Phys. Lett. 61, 1022 (1992).
11. S. S. Wang, R. Magnusson, J. S. Bagby, and M. G. Moharam, “Guided-mode resonances in planar dielectric-layer diffraction gratings,” J. Opt. Soc. Am. A 7, 1470–1474 (1990).
12. R. Petit, ed., Electromagnetic Theory of Gratings (Springer-Verlag, Berlin, 1980).
13. S. T. Peng, H. L. Bertoni, and T. Tamir, “Analysis of periodic thin-film structures with rectangular profiles,” Opt. Commun. 10, 91–94 (1974).
14. M. G. Moharam and T. K. Gaylord, “Diffraction analysis of dielectric surface-relief gratings,” J. Opt. Soc. Am. 72, 1385–1392 (1982).
15. P. Lalanne, J. P. Hugonin, and P. Chavel, “Optical properties of deep lamellar gratings: a coupled Bloch-mode insight,” J. Lightwave Technol. 24, 2442–2449 (2006).
16. C. J. Chang-Hasnain and W. Yang, “High-contrast gratings for integrated optoelectronics,” Adv. Opt. Photon. 4, 379–440 (2012).
17. D. Fattal, J. Li, Z. Peng, M. Fiorentino, and R. G. Beausoleil, “Flat dielectric grating reflectors with focusing abilities,” Nat. Photonics 4, 466–470 (2010).
18. B. Zhang, Z. Wang, S. Brodbeck, C. Schneider, M. Kamp, S. Hofling, and H. Deng, “Zero-dimensional polariton laser in a subwavelength grating-based vertical microcavity,” Light Sci. Appl. 3, e135 (2014).
19. G. Quaranta, G. Basset, O. J. F. Martin, and B. Gallinet, “Recent advances in resonant waveguide gratings,” Laser Photonics Rev. 12, 1800017 (2018).
20. A. V. Kildishev, A. Boltasseva, and V. M. Shalaev, “Planar photonics with metasurfaces,” Science 339(6125), 1232009 (2013).

21. B. Desiatov, N. Mazurski, Y. Fainman, and U. Levy, “Polarization selective beam shaping using nanoscale dielectric metasurfaces,” Opt. Express 23(17), 22611–22618 (2015).
22. A. Arbabi, Y. Horie, M. Bagheri, and A. Faraon, “Dielectric metasurfaces for complete control of phase and polarization with subwavelength spatial resolution and high transmission,” Nat. Nanotechnol. 10, 937–943 (2015).
23. A. L. Holsteen, A. F. Cihan, and M. L. Brongersma, “Temporal color mixing and dynamic beam shaping with silicon metasurfaces,” Science 365(6450), 257–260 (2019).
24. S. Jahani and Z. Jacob, “All-dielectric metamaterials,” Nat. Nanotechnol. 11, 23–36 (2016).
25. S. M. Rytov, “Electromagnetic properties of a finely stratified medium,” Sov. Phys. JETP 2(3) 466-475 (1956).
26. T. K. Gaylord, W. E. Baird, and M. G. Moharam, ‘‘Zero reflectivity high spatial-frequency rectangular-groove dielectric surface-relief gratings,’’ Appl. Opt. 25, 4562–4567 (1986).
27. Y. Ono, Y. Kimura, Y. Ohta, N. Nishada, “Antireflection effect in ultrahigh spatial-frequency holographic relief gratings,” Appl. Opt. 26, 1142–1146 (1987).
28. I. Ricther, P. C. Sun, F. Xu, and Y. Fainman, ‘‘Design considerations of form birefringent microstructures,’’ Appl. Opt. 34, 2421–2429 (1995).
29. D. Raguin and G. M. Morris, “Antireflection structured surfaces for the infrared spectral region,” Appl. Opt. 32, 1154–1167 (1993).
30. S. W. Tang, B. C. Zhu, M. Jia, Q. He, S. L. Sun, Y. F. Mei, and L. Zhou, “Effective-medium theory for one-dimensional gratings,” Phys. Rev. B 91, 174201 (2015).
31. Ph. Lalanne and D. Lemercier-Lalanne, ‘‘On the effective medium theory of subwavelength periodic structures,’’ J. Mod. Opt. 43, 2063–2085 (1996).
32. P. Lalanne and J. P. Hugonin, “High-order effective-medium theory of subwavelength gratings in classical mounting: application to volume holograms,” J. Opt. Soc. Am. A 15(7), 1843–1851 (1998).
33. S. Isaacs, A. Hajoj, M. Abutoama, A. Kozlovsky, E. Golan, and I. Abdulhalim, “Resonant Grating without a Planar Waveguide Layer as a Refractive Index Sensor,” Sensors 19, 3003 (2019).
34. H. Kikuta, H. Yoshida, and K. Iwata, ‘‘Ability and limitation of effective medium theory for subwavelength gratings,’’ Opt. Rev. 2, 92–99 (1995).
35. Y. H. Ko and R. Magnusson, “Wideband dielectric metamaterial reflectors: Mie scattering or leaky Bloch mode resonance?” Optica 5, 289-294 (2018).
36. T. K. Gaylord and M. G. Moharam, “Analysis and Applications of Optical Diffraction by Gratings,” Proc. IEEE 73(5), 894–937 (1985).
37. P. Moritra, B. A. Slovick, Z. G. Yu, S. Krishnamurthy, and J. Valentine, “Experimental demonstration of a broadband all-dielectric metamaterial perfect reflector,” Appl. Phys. Lett. 104, 171102 (2014).
38. V. Karagodsky, F. G. Sedgwick, and C. J. Chang-Hasnain, “Theoretical analysis of subwavelength high contrast grating reflectors,” Opt. Express 18(16), 16973–16988 (2010).

39. C. F. R. Mateus, M. C. Y. Huang, L. Chen, C. J. Chang-Hasnain, and Y. Suzuki, “Broad-band mirror (1.12–1.62 μm) using a subwavelength grating,” IEEE Photon. Technol. Lett. 16(7), 1676–1678 (2004).
40. R. Magnusson and M. Shokooh-Saremi, “Physical basis for wideband resonant reflectors,” Opt. Express 16(5), 3456–3462 (2008).
41. H. Heo, S. Lee and S. Kim, "Tailoring Fano Resonance for Flat-Top Broadband Reflectors Based on Single Guided-Mode Resonance," J. Lightwave Technol. 37, 4244-4250 (2019).
42. S. Tibuleac and R. Magnusson, “Narrow-linewidth bandpass filters with diffractive thin-film layers,” Opt. Lett. 26, 584-586 (2001).
43. Y. Ding and R. Magnusson, “Doubly-resonant single-layer bandpass optical filters,” Opt. Lett. 29, 1135- 1137 (2004).
44. J. M. Foley, S. M. Young, J. D. Phillips, “Narrowband mid-infrared transmission filtering of a single layer dielectric grating,” Appl. Phys. Lett. 103, 071107 (2013).
45. M. Niraula, J. W. Yoon, and R. Magnusson, “Mode-coupling mechanisms of resonant transmission filters,” Opt. Express 22(21), 25817–25829 (2014).
46. D. Delbeke, R. Baets, and P. Muys, “Polarization-selective beam splitter based on a highly efficient simple binary diffraction grating,” Appl. Opt. 43, 6157-6165 (2004).
47. J. W. Yoon, K. J. Lee, and R. Magnusson, “Ultra-sparse dielectric nanowire grids as wideband reflectors and polarizers,” Opt. Express 23, 28849-28856 (2015).
48. E. H. Land, “Some aspects of the development of sheet polarizers,” J. Opt. Soc. Am. 41, 957–962 (1951).
49. J. A. Reyes-Esqueda, C. Torres-Torres, J. C. Cheang-Wong, A. Crespo-Sosa, L. Rodríguez-Fernández, C. Noguez, and A. Oliver, “Large optical birefringence by anisotropic silver nanocomposites,” Opt. Express 16, 710–717 (2008).
50. P. B. Clapham, M. J. Downs, and R. J. King, "Some Applications of Thin Films to Polarization Devices," Appl. Opt. 8, 1965-1974 (1969).
51. M. Xu , H. P. Urbach , D. K. G deBoer , and H. J. Cornelissen , “Wire-grid diffraction gratings used a polarizing beam splitter for visible light and applied in liquid crystal on silicon ,” Opt. Express 13 , 2303 – 2320 (2005).
52. J. Kang, H-S. Yun, H-I. Jang, J. Kim, J. H. Park, J-Y. Lee, “Solution-processed aluminium nanogratings for wire grid polarizers,” Adv. Opt. Mater. 6, 1800205 (2018).
53. R. C. Tyan, A. A. Salvekar, H. P. Chou, C. C. Cheng, A. Scherer, Y. Fainman, “Design, fabrication, and characterization of form-birefringent multilayer polarization beam splitter,” J. Opt. Soc. Am. 14, 1627–1636 (1997).
54. D. Delbeke, R. Baets, and P. Muys, “Polarization-selective beam splitter based on a highly efficient simple binary diffraction grating,” Appl. Opt. 43, 6157-6165 (2004).
55. K. J. Lee, R. LaComb, B. Britton, M. Shokooh-Saremi, H. Silva, E. Donkor, Y. Ding, and R. Magnusson, “Silicon-layer guided-mode resonance polarizer with 40-nm bandwidth,” IEEE Photon. Technol. Lett. 20, 1857–1859 (2008).

56. K. J. Lee, J. Giese, L. Ajayi, R. Magnusson, and E. Johnson, "Resonant grating polarizers made with silicon nitride, titanium dioxide, and silicon: Design, fabrication, and characterization," Opt. Express 22, 9271-9281 (2014).
57. A D. Lin, P. Fan, E. Hasman, and M. Brongersma, "Dielectric gradient metasurface optical elements," Science 345, 298–302 (2014).
58. P. Genevet, F. Capasso, F. Aieta, M. Khorasaninejad, and R. Devlin, "Recent advances in planar optics: from plasmonic to dielectric metasurfaces," Optica 4, 139-152 (2017).
59. M. Kamali Seyedeh, E. Arbabi, A. Arbabi, and A. Faraon, "A review of dielectric optical metasurfaces for wavefront control," Nanophotonics 7, 1041–1068 (2018).
60. A. Arbabi, Y. Horie, M. Bagheri, and A. Faraon, "Dielectric metasurfaces for complete control of phase and polarization with subwavelength spatial resolution and high transmission," Nat. Nanotechnol. 10, 937– 943 (2015).
61. E. Arbabi, S. M. Kamali, A. Arbabi, and A. Faraon, "Full-stokes imaging polarimetry using dielectric metasurfaces," ACS Photon. 5, 3132–3140 (2018).
62. Y. Yang, W. Wang, P. Moitra, I. I. Kravchenko, D. P. Briggs, and J. Valentine, "Dielectric meta-reflectarray for broadband linear polarization conversion and optical vortex generation," Nano Lett. 14, 1394–1399 (2014).
63. M. Kraemer, and T. Baur, "Extinction ratio measurements on high purity linear polarizers," Proc. SPIE 10655, 1065505 (2018).
64. C. Sanchez, B. Julian, P. Belleville, and M. Popall, "Applications of hybrid organic-inorganic nanocomposites," J. Mater. Chem. 15(35), 3559-3592 (2005).
65. C. Lü and B. Yang, "High refractive index organic–inorganic nanocomposites: design, synthesis and application, "J. Mater. Chem. 19(19), 2884-2901 (2009).
66. K. Segala, R. L. Dutra, C. V. Franco, A. S. Pereira, and T. Trindade, "In situ and ex situ preparation of ZnO/Poly-{trans-[RuCl2(vpy)4]/styrene} nanocomposites," J. Braz. Chem. Soc. 21(10), 1986-1991(2010).
67. I. Denisyuk, and M. Fokina, "A review of high nanoparticles concentration composites: semiconductor and high refractive index materials," in nanocrystals, Y. Masuda, ed. (Sciyo, 2010) Chap. 5.
68. C. Lu, Z. Cui, Y. Wang, Z. Li, C. Guan, B. Yang, and J. Shen "Preparation and characterization of ZnS-polymer nanocomposite films with high refractive index," J. Mater. Chem. 13(9), 2189-2195 (2003).
69. K. Xu, and Y. Q. Hu "Fabrication of transparent PU/ZrO2 nanocomposite coating with high refractive index," Chin. J. Polym. Sci. 28(1), 13-20 (2010).
70. A. Pradana, C. Kluge, and M. Gerken, "Tailoring the refractive index of nanoimprint resist by blending with TiO2 nanoparticles," Opt. Mater. Express 4(2), 329-337 (2014).
71. B. Cai, O. Sugihara, H. I. Elim, T. Adschiri, and T. Kaino, "A novel preparation of high-refractive-index and highly transparent polymer nanohybrid composites," Appl. Phys. Express 4(9), 092601 (2011).
72. L. Zimmermann, M. Weibel, W. Caseri, and U. W. Suter, "High refractive index films of polymer nanocomposites," J. Mater. Res. 8(7), 1742-1748 (1993).

73. C. Lü, C. Guan, Y. Liu, Y. Cheng, and B. Yang, “PbS/polymer nanocomposite optical materials with high refractive index,” Chem. Mater. 17(9), 2448-2454 (2005).
74. W. Caseri “Nanocomposites of polymers and metals or semiconductors: Historical background and optical properties,” Macromol. Rapid. Commun. 21(11), 705-722 (2000).
75. C. Ingrosso, A. Panniello, R. Comparelli, M. L.Curri, “Colloidal inorganic nanocrystal based nanocomposites: functional materials for micro and nanofabrication,” Materials 3(2), 1316-1352 (2010).
76. R. A. Sperling, and W. J. Parak, “Surface modification, functionalization and bioconjugation of colloidal inorganic nanoparticles,” Phil. Trans. R. Soc. A 368(1915), 1333-1383 (2010).
77. T. Kondo, S. Ura, and R. Magnusson, “Design of guided-mode resonance mirrors for short laser cavities,” J. Opt. Soc. Am. A 32(8), 1454-1458 (2015).
78. D. Wawro, S. Tibuleac, R. Magnusson, and H. Liu, “Optical fiber endface biosensor based on resonances in dielectric waveguide gratings,” Proc. SPIE 3911, 86–94 (2000).
79. K. Jia, D. Zhang, J. Ma, “Sensitivity of guided mode resonance filter-based biosensor in visible and near infrared ranges,” Sensors and Actuators B 156(1), 194-197 (2011).
80. M. Niraula, J. W. Yoon, and R. Magnusson, “Single-layer optical bandpass filter technology,” Optics Letters 40(21), 5062-5065 (2015).
81. Y. Xia, J. A. Rogers, K. E. Paul, and G. M. Whitesides, “Unconventional methods for fabricating and patterning nanostructures,” Chem. Rev. 99(7) 1823-1848 (1999).
82. S. Y. Chou, P. R. Krauss, and P. J. Renstrom, “Nanoimprint lithography,” J. Vac. Sci. Technol. B 14(6), 4129-4133 (1996).
83. H. Schift, “Nanoimprint lithography: an old story in modern times? A review,” J. Vac. Sci. Technol. B 26(2), 458-480 (2008).
84. L. J. Guo, “Nanoimprint lithography: methods and material requirements,” Adv. Mater. 19(4), 495–513 (2007).
85. K. J. Lee, J. Jin, B. - S. Bae, and R. Magnusson, “Guided-mode resonance filters fabricated with soft lithography,” in Recent Advances in Nanofabrication Techniques and Applications, B. Cui, ed. (InTech, 2011) Chap. 12.
86. Y. Huang, L. Liu, M. Johnson, A. C. Hillier, and M. Lu, “One-step sol-gel imprint lithography for guided-mode resonance structures,” Nanotechnology 27(9), 095302 (2016).
87. J. S. Lin, C. L. Lai, Y. C. Tu, C. H. Wu, and Y. Takeuchi, “A uniform pressure apparatus for micro/nanoimprint lithography equipment,” Int. J. of Automation Technology 3(1), 84-88 (2009).
88. H. Lee, “Effect of imprinting pressure on residual layer thickness in ultraviolet nanoimprint lithography,” J. Vac. Sci. Tech. B 23(3), 1102-1106 (2005).
89. H. J. Lee, H. W. Ro, C. L. Soles, R. L. Jones, E. K. Lin, and W. I. Wu, “Effect of initial resist thickness on residual layer thickness of nanoimprinted structures,” J. Vac. Sci. Tech. B 23(6), 3023-3027 (2005).

90. V. Malyarchuk, F. Hua, N. H. Mack, V. T. Velasquez, J. O. White, R. G. Nuzzo, and J. A. Rogers, "High performance plasmonic crystal sensor formed by soft nanoimprint lithography," Opt. Express 13(15), 5669-5675 (2005).
91. X. Liu, Y. Du, L. Hu, X. Zhou, Y. Li, Z. Dai, and J. Bao, "Understanding the effect of different polymeric surfactants on enhancing the silicon/reduced graphene oxide anode performance," J. Phys. Chem. C 119(11), 5848-5854 (2015).
92. K. M. Koczkur, S. Mourdikoudis, L. Polavarapu, and S. E. Skrabalak, "Polyvinylpyrrolidone (PVP) in nanoparticle synthesis," Dalton Trans. 44(41), 17883-17905 (2015).
93. M. D. Tang, A. P. Golden, and J. Tien, "Molding of three-dimensional microstructures of gels," J. Am. Chem. Soc. 125(43), 12988-12989 (2003).
94. G. Sheppard, T. Oseki, A. Baba, D. Patton, F. Kaneko, L. Mao, and J. Locklin, "Thiolene-based microfluidic flow cells for surface plasmon resonance imaging," Biomicrofluidics 5(2), 026501 (2011).
95. M. G. Moharam, D. A. Pommet, E. B. Grann, and T. K. Gaylord "Stable implementation of the rigorous coupled-wave analysis for surface-relief gratings: Enhanced transmittance matrix approach," J. Opt. Soc. Am. A 12, 1077-1086 (1995).
96. P. Moritra, B. A. Slovick, W. Li, I. Kravchencko, D. P. Briggs, S. Krishnamurthy, and J. Valentine, "Large-scale all-dielectric metamaterial perfect reflectors," ACS Photon. 2, 692–698 (2015).
97. H. Hemmati and R. Magnusson, "Resonant dual-grating metamembranes supporting spectrally narrow bound states in the continuum," Adv. Optical Mater. 7, 1900754 (2019).
98. Y. Zhao and A. Alu, "Manipulating light polarization with ultrathin plasmonic metasurfaces," Phys. Rev. B 84, 205428 (2011).
99. S. Lan, X. Zhang, M. Taghinejad, S. Rodrigues, K.-T. Lee, Z. Liu, and W. Cai, "Metasurfaces for near-eye augmented reality," ACS Photon. 6, 864–870 (2019).
100. S. J. Kim and M. L. Brongersma, "Active flat optics using a guided mode resonance," Opt. Lett. 42, 5–8 (2017).
101. M. Grande, M. A. Vincenti, T. Stomeo, G. V. Bianco, D. de Ceglia, N. Aközbek, V. Petruzzelli, G. Bruno, M. De Vittorio, M. Scalora, and A. D'Orazio, "Graphene-based perfect optical absorbers harnessing guided mode resonances," Opt. Express 23, 21032–21042 (2015).
102. S. Sarkar, V. Gupta, M. Kumar, J. Schubert, P. T. Probst, J. Joseph, T.A. F. König, "Hybridized guided-mode resonances via colloidal plasmonic self-assembled grating," ACS Appl. Mater. Interfaces 11, 13752−13760 (2019).
103. F. Aieta, M. A. Kats, P. Genevet, and F. Capasso, "Multiwavelength achromatic metasurfaces by dispersive phase compensation," Science 347, 1342–1345 (2015).
104. D. Lin, M. Melli, E. Poliakov, P. S. Hilaire, S. Dhuey, C. Peroz, S. Cabrini, M. Brongersma, and M. Klug, "Optical metasurfaces for high angle steering at visible wavelengths," Sci. Rep. 7, 2286 (2017).
105. E. F. Pecora, A. Cordaro, P. G. Kik, and M. L. Brongersma, "Antirefection coatings employing multiresonant dielectric metasurfaces," ACS Photonics 5, 4456–4462 (2018).

106. O. Ilic and H. A. Atwater, “Self-stabilizing photonic levitation and propulsion of nanostructured macroscopic objects,” Nat. Photonics 13, 289–295 (2019).
107. D. Xia, Z. Ku, S. C. Lee, and S. R. J. Brueck, “Nanostructures and functional materials fabricated by interferometric lithography,” Adv. Mater. 23, 147–179 (2011).
108. J. H. Seo, J. H. Park, S. I. Kim, B. J. Park, Z. Q. Ma, J. Choi, and B. K. Ju, “Nanopatterning by Laser Interference Lithography: Applications to Optical Devices,” J. Nanosci. Nanotechnol. 14(2), 1521–1532 (2014).
109. M. Campbell, D. N. Sharp, M. T. Harrison, R. G. Denning, and A. J. Tuberfield, “Fabrication of photonic crystals for the visible spectrum by holographic lithography,” Nature 404, 53–56 (2000).
110. Guy M. Burrow, Matthieu C. R. Leibovici, and Thomas K. Gaylord, "Pattern-integrated interference lithography: single-exposure fabrication of photonic-crystal structures," Appl. Opt. 51, 4028-4041 (2012).
111. J. B. Yeo, S. D. Yun, N. H. Kim, and H. Y. Lee, “Fabrication of Si-based two-dimensional photonic quasicrystals by using multiple-exposure holographic lithography,” J. Vac. Sci. Technol. 27, 1886 (2009).
112. A. Hassanzadeh, M. Mohammadnezhad, and S. Mittler, “Multiexposure laser interference lithography,” J. Nanophotonics 9(1), 093067 (2015).
113. M. Vala and J. Homola, “Multiple beam interference lithography: A tool for rapid fabrication of plasmonic arrays of arbitrary shaped nanomotifs,” Opt. Express 24(14), 15656–15665 (2016).
114. H. Lloyd, “On a new case of interference of the rays of light,” Trans. Roy. Irish Acad. 17, pp. 171–177 (1834).
115. J. von Neumann and E. Wigner, “Uber merkwürdige diskrete Eigenwerte” Phys. Z. 30, 467-470 (1929).
116. D. C. Marinica, A. G. Borisov, and S. V. Shabanov, “Bound States in the Continuum in Photonics” Phys. Rev. Lett. 100, 183902 (2008).
117. R. F. Kazarinov, Z. N. Sokolova, and R. A. Suris, “Planar distributed-feedback optical resonators” Sov. Phys. Tech. Phys. 21, 131-136 (1976).
118. Y. Ding and R. Magnusson, “Use of nondegenerate resonance leaky modes to fashion diverse optical spectra” Opt. Express 12, 1885-1891 (2004).
119. Z. S. Liu, S. Tibuleac, D. Shin, P. P. Young, and R. Magnusson, "High-efficiency guided-mode resonance filter," Opt. Lett. 23, 1556-1558 (1998).
120. J. Lee, B. Zhen, S. L. Chua, W. Qiu, J. D. Joannopoulos, M. Soljačić, and O. Shapira, “Observation and differentiation of unique high-Q optical resonances near zero wave vector in macroscopic photonic crystal slabs” Phys. Rev. Lett. 109, 067401 (2012).
121. K. Fan, I. V. Shadrivov, and W. J. Padilla, "Dynamic bound states in the continuum," Optica 6, 169-173 (2019).
122. L. Cong and R. Singh, “Symmetry-protected dual bound states in the continuum in metamaterials,” Adv. Opt. Mater. 7, 1900383 (2019).
123. J. W. Yoon, S. H. Song, and R. Magnusson, “Critical field enhancement of asymptotic optical bound states in the continuum,” Scientific Reports 5, 18301 (2015).

124. S. I. Azzam, V. M. Shalaev, A. Boltasseva, and A. V. Kildishev, “Formation of bound states in the continuum in hybrid plasmonic-photonic systems,” Phys. Rev. Lett. 121, 253901 (2018).
125. A. Kodigala, T. Lepetit, Q. Gu, B. Bahari, Y. Fainman, and B. Kanté, “Lasing action from photonic bound states in continuum” Nature 541, 196-199 (2017).
126. M. Kasraian, “Double-grating thin-film devices based on second-order Bragg interaction” J. of Appl. Phys.75, 7639-7652 (1994).
127. T. Liu, Y. Shen, W. Shin, Q. Zhu, S. Fan, and C. Jin, “Dislocated double-layer metal gratings: an efficient unidirectional coupler,” Nano Lett. 14(7), 3848–3854 (2014).
128. E. N. Bulgakov, D. N. Maksimov, P. N. Semina, and S. A. Skorobogatov, "Propagating bound states in the continuum in dielectric gratings" J. Opt. Soc. Am. B 35, 1218-1222 (2018).
129. T. Karrock and M. Gerken, "Pressure sensor based on flexible photonic crystal membrane" Biomed. Opt. Express 6, 4901-4911 (2015).
130. Jon Olav Grepstad, Peter Kaspar, Olav Solgaard, Ib-Rune Johansen, and Aasmund S. Sudbø, "Photonic-crystal membranes for optical detection of single nano-particles, designed for biosensor application" Opt. Express 20, 7954-7965 (2012).
131. C. Lin, J. Wang, C. Chen, K. Shen, D. Yeh, Y. Kiang, and C. Yang, “A GaN photonic crystal membrane laser” Nanotechnology 22, 025201 (2011).
132. K. Srinivasan, P. E. Barclay, O. Painter, J. Chen, and A. Y. Cho, “Fabrication of high-quality-factor photonic crystal microcavities in InAsP/InGaAsP membranes” J. Vac. Sci. Technol. B 22, 875-879 (2004).
133. W. Zhou, Z. Ma, H. Yang, Z. Qiang, G. Qin, H. Pang, L. Chen, W. Yang, S. Chuwongin, and D. Zhao, “Flexible photonic-crystal Fano filters based on transferred semiconductor nanomembranes,” J. Phys. D 42, 234007 (2009).
134. M. Karl, J. M. E. Glackin, M. Schubert, N. M. Kronenberg, G. A. Turnbull, I. D. W. Samuel, and M. C. Gather, “Flexible and ultra-lightweight polymer membrane lasers,” Nat. Commun. 9, 1525 (2018).
135. H. Hemmati and R. Magnusson, "Development of tuned refractive-index nanocomposites to fabricate nanoimprinted optical devices," Opt. Mater. Express 8, 175-183 (2018).
136. H. Lee, S.H. Hong, K.Y. Yang, K.W. Choi, “Fabrication of 100 nm metal lines on flexible plastic substrate using ultraviolet curing nanoimprint lithography” Appl. Phys. Lett. 88 pp. 143112-1-143112 (2006).
137. N. B. A. Talip, and J. Taniguchi. "Fabrication of double-sided self-supporting antireflection-structured film by ultraviolet nanoimprint lithography." *Japanese Journal of Applied Physics* 53, no. 6S (2014): 06JK03.
138. H. Kogelnik, in Integrated Optics, Vol. 7 of Topics in Applied Physics, T.Tamir, ed. (Springer-Verlag, 1979), pp. 13-81.
139. F. L. Pedrotti, L. M. Pedrotti, and L. S. Pedrotti, in Introduction to Optics, 3th ed. (Pearson, 2006), pp. 200-204.
140. S. G. Lee and R. Magnusson, “Band flips and bound-state transitions in leaky-mode photonic lattices” Phys. Rev. B 99, 045304 (2019).

141. S. Tibuleac, D. Wawro, and R. Magnusson, “Resonant diffractive structures integrating waveguide-gratings on optical fiber endfaces,” LEOS’99, IEEE Lasers and Electro-Optics Society 1999 Annual Meeting, Conference Proceedings, 2, 874–875, San Francisco, California, (1999).
142. D. Wawro, S. Tibuleac, and R. Magnusson, “Resonant waveguide-grating filters and sensors and methods for making and using same,” U.S. patent No. 7,167,615.
143. L. G. Cohen and M. V. Schneider, “Microlenses for coupling junction lasers to optical fibers” Appl. Opt. 13, 89-94 (1974).
144. G. Kostovski, P. R. Stoddart, and A. Mitchell, “The optical fiber tip: an inherently light-coupled microscopic platform for micro-and nanotechnologies” Adv. Mater. 26, 3798-3820 (2014).
145. S. Choi, K. R. Kim, K. Oh, C. M. Chun, M. J. Kim, S. J. Yoo, and D. Y. Kim, “Interferometric inscription of surface relief gratings on optical fiber using azo polymer film” Appl. Phys. Lett. 83, 1080-1082 (2003).
146. Y. Lin, Y. Zou, Y. Mo, J. Guo, and R. G. Lindquist, “E-beam patterned gold nanodot arrays on optical fiber tips for localized surface plasmon resonance biochemical sensing” Sensors (Basel, Switzerland). 10, 9397-9406 (2010).
147. A. Dhawan, J. F. Muth, D.N. Leonard, M. D. Gerhold, J. Gleeson, T. Vo-Dinh, and P. E. Russell, “FIB fabrication of metallic nanostructures on end-faces of optical fibers for chemical sensing applications” J. Vac. Sci. Technol B Microelectron Nanometer Struct Process Meas Phenom. 26, 2168-2173 (2008).
148. S. Scheerlinck, P. Bienstman, E. Schact, and D.V. Thourhout, “Metal grating patterning on fiber facets by UV-based nano imprint and transfer lithography using optical alignment” IEEE Journal of Lightwave Technology, 27, 1415-1420 (2009).
149. G. Kostovski, U. Chinnasamy, S. Jayawardhana, P. R. Stoddart, and A. Mitchell, “Sub-15nm optical fiber nano imprint lithography: a parallel, self-aligned and portable approach” Adv. Mater. 23, 531-535 (2011).
150. G. Calafiore, A. Koshelev, F. I. Allen, S. Dhuey, S. Sassolini, E. Wong, P. Lum, K. Munechika and S. Cabrini, “Nanoimprint of a 3D structure on an optical fiber for light wavefront manipulation” Nanotechnology, 27, 1-6 (2016).
151. M. D. Feit and J. A. Fleck, “Light propagation in graded-index optical fibers”, Appl. Opt. 17, 3990 (1978).

Appendix A

List of Publications

Journal Publications

1. **H. Hemmati** and R. Magnusson, “Applicability of the Rytov full effective-medium formalism to the physical description and design of resonant metasurfaces,” *ACS Photonics* **(2020).**
2. **H. Hemmati**, P. Bootpakdeetam, K. J. Lee, and R. Magnusson, "Rapid large-scale fabrication of multipart unit cell metasurfaces," *Opt. Express* 28, 19304-19314 (**2020**).
3. **H. Hemmati**, P. Bootpakdeetam, and R. Magnusson, "Metamaterial polarizer providing principally unlimited extinction," *Opt. Lett.* 44, 5630-5633 (**2019**).
4. **H. Hemmati** and R. Magnusson, “Resonant dual-grating metamembranes supporting spectrally narrow bound states in the continuum,” *Adv. Opt. Mater*. 7(20), 1900754 (**2019**).
5. D. J. Carney, H. G. Svavarsson, **H. Hemmati**, A. Fannin, J. W. Yoon, and R. Magnusson, “Refractometric Sensing with Periodic Nano-Indented Arrays: Effect of Structural Dimensions,” *Sensors* 19, 897, (**2019**).
6. **H. Hemmati** and R. Magnusson, "Development of tuned refractive-index nanocomposites to fabricate nanoimprinted optical devices," *Opt. Mater. Express* 8, 175-183 (**2018**).
7. **H. Hemmati**, Y. H. Ko, and R. Magnusson, "Fiber-facet-integrated guided-mode resonance filters and sensors: experimental realization," *Opt. Lett.* 43, 358-361 (**2018**).

Conference Proceedings

1. R. Magnusson, K. J. Lee, **H. Hemmati**, P. Bootpakdeetam, J. Vasilyev, F. A. Simlan, N. Razmjooei, Y. H. Ko, S. Zhang, S. G. Lee, H. G. Svavarsson, *Proc. SPIE,* 11290-5 (**2020**).
2. **H. Hemmati** and R. Magnusson, *IEEE Research and Applications of Photonics in Defense (RAPID)*, 1-2 (**2019**).
3. **H. Hemmati**, and R. Magnusson, *Proc. SPIE 10914, Optical Components and Materials XVI,* 1091409 (**2019**).
4. R. Magnusson, S. G. Lee, K. J. Lee, **H. Hemmati**, D. J. Carney, P. Bootpakdeetam, and Y. H. Ko, *Proc. SPIE 10921, Integrated Optics: Devices, Materials, and Technologies XXIII*, 109211E (**2019**).
5. R. Magnusson, K. J. Lee, **H. Hemmati**, D. Carney, and S. G. Lee, *IEEE Aerospace Conference*, 1-8 (**2019**).
6. **H. Hemmati** and R. Magnusson, *Frontiers in Optics / Laser Science, OSA Technical Digest (JTu3A.85),* 1-2 (**2018**).
7. R. Magnusson, K. J. Lee, **H. Hemmati**, Y. H. Ko, B. R. Wenner, J. W. Allen, M. S. Gimlin, D. W. Weidanz, *Frontiers in Biological Detection: From Nanosensors to Systems X 10510*, 105100G (**2018**).
8. **H. Hemmati** and R. Magnusson, Frontiers in Optics, OSA Technical Digest (Optical Society of America, paper JW3A.104), 1-2 (**2017**).

Biographical Information

Hafez Hemmati completed his B.Sc. and M.Sc. in Materials Science and Engineering at Sharif University of Technology (SUT) and Iran University of Science and Technology (IUST), Tehran, Iran in 2010 and 2013, respectively. In 2016, he moved to the USA and began his Ph.D. work at the University of Texas at Arlington (UTA) at the Nanophotonics Device Group, led by Prof. Robert Magnusson. Through his Ph.D., he worked on several NSF projects, some in collaboration with optical companies, to design, develop, and characterize various resonant-nanostructure-based optical elements such as filters, sensors, reflectors, and polarizers. His research interests include theory and experiment of periodic nanostructures, nanoelectronics, optical materials, diffractive optics, micro/nano fabrication, and semiconductor-patterning technology.